NASA/TM-2017-219473

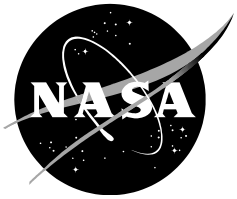

Design Guide for Aerodynamics Testing of Earth and Planetary Entry Vehicles in a Ballistic Range

David W. Bogdanoff
AMA, Inc., Moffett Field, California
Ames Research Center, Moffett Field, California

January, 2017

NASA STI Program ... in Profile

Since its founding, NASA has been dedicated to the advancement of aeronautics and space science. The NASA scientific and technical information (STI) program plays a key part in helping NASA maintain this important role.

The NASA STI program operates under the auspices of the Agency Chief Information Officer. It collects, organizes, provides for archiving, and disseminates NASA's STI. The NASA STI program provides access to the NTRS Registered and its public interface, the NASA Technical Reports Server, thus providing one of the largest collections of aeronautical and space science STI in the world. Results are published in both non-NASA channels and by NASA in the NASA STI Report Series, which includes the following report types:

- TECHNICAL PUBLICATION. Reports of completed research or a major significant phase of research that present the results of NASA Programs and include extensive data or theoretical analysis. Includes compilations of significant scientific and technical data and information deemed to be of continuing reference value. NASA counterpart of peer-reviewed formal professional papers but has less stringent limitations on manuscript length and extent of graphic presentations.

- TECHNICAL MEMORANDUM. Scientific and technical findings that are preliminary or of specialized interest, e.g., quick release reports, working papers, and bibliographies that contain minimal annotation. Does not contain extensive analysis.

- CONTRACTOR REPORT. Scientific and technical findings by NASA-sponsored contractors and grantees.

- CONFERENCE PUBLICATION. Collected papers from scientific and technical conferences, symposia, seminars, or other meetings sponsored or co-sponsored by NASA.

- SPECIAL PUBLICATION. Scientific, technical, or historical information from NASA programs, projects, and missions, often concerned with subjects having substantial public interest.

- TECHNICAL TRANSLATION. English-language translations of foreign scientific and technical material pertinent to NASA's mission.

Specialized services also include organizing and publishing research results, distributing specialized research announcements and feeds, providing information desk and personal search support, and enabling data exchange services.

For more information about the NASA STI program, see the following:

- Access the NASA STI program home page at http://www.sti.nasa.gov

- E-mail your question to help@sti.nasa.gov

- Phone the NASA STI Information Desk at 757-864-9658

- Write to:
  NASA STI Information Desk
  Mail Stop 148
  NASA Langley Research Center
  Hampton, VA 23681-2199

Table of Contents

1. Summary and Introduction

The purpose of this manual is to aid in the design of an aerodynamics test of an Earth or planetary entry capsule in a ballistic range. In this manual, much use is made of the results and experience gained in 50 years of ballistic range aerodynamics testing at the NASA Ames Research Center, and in particular, that gained in the last 30 years, while the author was working at NASA Ames. The topics treated herein include:

- Data to be obtained; predicted flight data needed to design test
- Reynolds number and dynamic similarity of flight trajectory and ballistic range test; capabilities of various ballistic ranges
- Calculations of swerves due to average and oscillating lift and of drag-induced velocity decreases
- Model and sabot design; materials, weights and stresses
- Sabot separation
- Launches at angle of attack and “slapping” with paper to produce pitch/yaw oscillations

Nomenclature

A	area
a	acceleration
C_D	drag coefficient
C_L	lift coefficient
C_m	pitching moment coefficient
C_{m_q}	pitch damping coefficient
C_{m_α}	derivative of pitching moment coefficient with respect to angle of attack
C_n	yawing moment coefficient
C_{n_r}	yaw damping coefficient
C_Y	side force coefficient
c	speed of sound
D	diameter
$\left.\frac{du}{u}\right\|_\lambda$	fractional velocity drop over distance of one pitch oscillation wavelength
E	Young's modulus of elasticity
E_s	strain energy per unit volume
$\bar{E}_s$	strain energy per unit volume averaged over shell thickness
$\bar{E}_{sm}$	strain energy per unit mass averaged over shell thickness
$\bar{\bar{E}}_{sm}$	strain energy per unit mass averaged over shell thickness and averaged over entire shell
F	force
I	moment of inertia for pitching motion about center of gravity for model or flight vehicle
I_A	angular impulse
I_b	moment of inertia of shell about neutral axis per unit length
I_L	linear impulse
K	constant, see Eq. (4)
K_a	kinetic energy per unit mass
L	lift
L	length of range
M	Mach number
$\bar{M}$	average Mach number
M_b	bending moment
m	mass
m	paper mass loading (mass per unit area)
m_p	paper mass loading (mass per unit area)
P	period of pitch oscillation
P_r	range pressure
R	$= \rho_s/\rho$
Re	Reynolds number
r	radius
r_g	radius of gyration
T	temperature
s	sideways swerve

t time
t_a shell thickness
u velocity
u_a velocity of thin shell or aerobrake with respect remainder of model
V volume
x distance
x_{cg} x location of center of gravity
y swerve to side
y_{max} maximum swerve to side
$\ddot{y}$ acceleration to side
z_{cg} z location of center of gravity

Subscripts:

cg center of gravity
f flight
max maximum
r range
λ for one pitch oscillation wavelength

Greek:

α pitch angle of attack
$\tilde{\alpha}$ rms pitch angle of attack
β yaw angle of attack
$\tilde{\beta}$ rms yaw angle of attack
ε_b strain
θ pitch angle of attack
θ_{max} maximum pitch angle of attack
$\dot{\theta}_{max}$ maximum rate of change of pitch angle of attack
λ wavelength of pitch oscillation
μ viscosity
π 3.14159...
ρ gas density
ρ_a shell density
ρ_s model or vehicle density
ρ_{sr} range model density
σ_b maximum compressive or tensile stress
σ_{yield} material yield stress

2. Description of a ballistic range; types of testing covered in this manual; data to be obtained

Figure 1 shows a sketch of the NASA Ames HFFAF (Hypervelocity Free Flight Aerodynamic Facility) ballistic range, which is representative of enclosed test section ranges. Key elements of the range are the launch gun, dump tank (to contain the muzzle blast), sabot stripper (to prevent the sabot fingers from flying down the range) and test section with spark shadowgraph stations

and cameras. The Ames HFFAF range has 16 orthogonal stations and 32 cameras. In the HFFAF, the shadowgraphs are shuttered by 40 nanosecond Kerr cells. Open air ranges, operating at atmospheric pressure, do not use a dump tank or an enclosed test section. Models are typically launched inside multi-piece carriers, called sabots. Figure 2 shows a model to be launched by a four piece sabot, comprising four sabot "fingers", locked together in the gun barrel by serrations. On exiting the gun muzzle, the sabot fingers are meant to be separated sideways from the model by aerodynamic forces acting on the fronts of the fingers and/or muzzle blast forces acting on the rears of the fingers. With sufficient lateral sabot finger separation, the fingers will impact on the outside of the sabot stripper cone and the model will travel down the range unaccompanied by the fingers.

The launch gun can be a cold gas gun for low velocities (up to ~1.3 km/s) or a powder gun for velocities up to ~2.5 km/s. For higher velocities a two-stage light gas gun using helium or hydrogen (for the highest velocities) is often used. Figure 3 shows a representative two-stage light gas gun. The piston (often plastic) is accelerated by the gunpowder gas to velocities between (typically) 500 to 1000 m/s, and greatly compresses and heats the light working gas. When the light gas pressure reaches a certain value, the diaphragm breaks and the compressed light gas accelerates the launch package (with the model) down the launch tube. Muzzle velocities up to 7 km/s can be obtained fairly routinely (with hydrogen). With special gun designs and operating conditions and light projectiles, launches at velocities up to ~11 km/s have been achieved.

The vehicle models treated herein are Earth and planetary entry capsules, including those with low density aerobrakes (i.e., inflatables, deployables) outside a compact centerbody. In general, the models are axisymmetric or have a plane of symmetry. The models may trim at an angle of attack (and hence, lift) due to an off-axis weight or a trim tab. More complex models, such as airplane shapes or capsule models with an abort rocket tower attached, are not discussed. Also, aerodynamic heating models, which are generally launched with minimal pitch and yaw angles, are not treated. Testing of highly lifting and swerving models, such as those for shuttle tank foam debris, is also not discussed. The exclusion of a number of types of testing keeps the scope of the present paper within manageable bounds, and permits us to examine in some detail testing that does lie within the scope of the paper.

The data sought are generally:

The drag coefficient, C_D, as a function of the pitch angle of attack, α
The lift coefficient, C_L, as a function of the pitch angle of attack, α
The pitching moment coefficient, C_m, as a function of the pitch angle of attack, α
The pitch damping coefficient, C_{m_q}, as a function of the rms amplitude of the pitch oscillations, $\tilde{\alpha}$
The above data are often sought for a number of Mach numbers in a test entry

For non-axisymmetric models with a plane of symmetry, other coefficients, such as the side force coefficient, C_Y, the yawing moment coefficient, C_n, and the yaw damping coefficient, C_{n_r}, can also be obtained and all coefficients are, in principle, functions of the pitch angle of attack, α, and the yaw angle of attack, β. In addition, the damping coefficients are functions of the rms angles of attack, $\tilde{\alpha}$ and $\tilde{\beta}$. However, in general, the model behavior is not very different with respect to pitch or yaw oscillations and designing of a test can be done by referring only to C_D, C_L and C_m as functions of the pitch angle of attack, α, at the Mach numbers of interest.

3. Data needed for test design

In order to design a test that simulates full-scale flght, certain data are required. This includes vehicle physical and aerodynamic data (the latter would be estimates from CFD solutions) and the flight trajectory data. These will be used to calculate the degree to which dynamic similarity and Reynolds number similarity can be achieved between the flight vehicle and the range model and to estimate the model swerves due to oscillating and average lift. Similarity is treated in sections 5 through 7. Swerve due to oscillating lift and the effect of its amplitude on the accuracy of the determination of the lift coefficient as a function of the pitch angle of attack is discussed in section 8. Swerve due to average lift for lifting vehicles can obviously lead to the model flying out of the field of view of the cameras and is discussed in section 9.

To perform the required calculations, considerable data, including predicted flight data, is needed. First, one needs the vehicle physical data, as follows:

- Diameter, D (area, A = $\frac{\pi}{4}D^2$)
- Mass, m
- Moment of inertia for pitch oscillations, I
- Radius of gyration, r_g, defined by r_g^2 = I/m
- Volume, V
- Density of flight vehicle, ρ_s = m/V
- Location of CG, x_{cg}, z_{cg}

- Vehicle shape (drawings)
- Note that subscript f will denote flight vehicle parameters and subscript r will denote range model parameters

Next, one needs vehicle aerodynamic data, usually computational (CFD) values at the flight conditions of interest. For each Mach number of interest, these comprise:

- The drag coefficient, C_D
- The lift coefficient, C_L, as a function of the pitch angle of attack, α
- The pitching moment coefficient, C_m, as a function of the pitch angle of attack, α; from this data, the derivative C_{m_α} can be calculated

Finally, one needs the trajectory data at each point along the trajectory to be tested. These comprise:

- Atmospheric composition
- Velocity, u
- Density, ρ
- Temperature, T
- From the temperature, T, and the atmospheric composition, the speed of sound, c, and the viscosity, μ, can be obtained
- The Mach number, M, follows from M = u/c and the Reynolds number, Re, follows from

$$\mathrm{Re} = \frac{\rho u D}{\mu}$$

4. Calculations which need to be performed

For each point along the flight trajectory to be simulated, one must calculate Re, ρ_s/ρ and λ/D, where:

Re = Reynolds number
ρ_s = flight vehicle mean density
ρ = atmospheric density
λ = wavelength of pitch oscillations
D = flight vehicle diameter

The three aforementioned quantities must be matched, as closely as possible, between the flight conditions and the ballistic range conditions in order the achieve Reynolds number similarity and dynamic similarity. (Further discussion is presented in Sec. 5.) Then, the capabilities of the ranges in question need to be plotted in the Re – ρ_s/ρ plane. These capabilities are determined by various limits discussed at a later point. The flight trajectory must then be plotted on the Re – ρ_s/ρ plane. This will aid one to select the most suitable range in which to perform the desired test campaign. At this point, it may already be necessary to accept some compromises, that is, to accept some mismatches in Re and ρ_s/ρ. For example, it may prove impossible to simulate simultaneously high values of Re and low values of ρ_s/ρ. An option in this case would be to accept the Re mismatch and simulate accurately the flight values of ρ_s/ρ in the range.

From λ/D and the spacing of the camera stations, D needs to be selected to put 6 to 8 camera stations in each pitch oscillation cycle. Then, the gun should be selected to make this D value as close to 80% of the gun bore diameter as possible, without exceeding the 80% figure. Some compromise may be necessary here. The 80% figure is good general rule, but saboted models have been launched that had diameters up to 90% of the gun bore diameter. In such a case, there would be increased concerns about sabot failure due to the launch stresses.

If the range is an enclosed, variable pressure range, the range pressure needs to be selected to match Re, if possible. If the range is an open air range, the range pressure is always atmospheric, which determines what Re values will be obtained. ρ_s should be chosen to match $(\rho_s/\rho)_{flight}$. The model material then needs to be chosen to match ρ_s as close as is possible. Multi-material models or models with internal hollows may be necessary to get a good match of ρ_s.

These calculations may need to be iterated as required. As stated previously, it may be necessary to accept some mismatches in Re and ρ_s/ρ in the final model design and test condition selection. After the main design work outlined above has been done, several checks and additional calculations should be made, as follows.

The normalized drop in velocity per pitch oscillation cycle and for the length of the range should be checked. These are $\left.\frac{du}{u}\right|_{\lambda}$ and $\left.\frac{du}{u}\right|_{range}$, where du is the velocity drop and u is the average velocity. To maintain a “constant” test condition in the range (as much as possible), it would be desirable if $\left.\frac{du}{u}\right|_{range}$ were less than 0.20, but this may be difficult to achieve for a lightweight ballistic range model encountering a relatively high density test gas. There is also a

lower limit to $\left.\frac{du}{u}\right|_{range}$ connected with having acceptable accuracy in determining the drag coefficient. To have reasonable dynamic similarity for drag slow down between the flight vehicle and the model, $\left.\frac{du}{u}\right|_{\lambda}$ should not be too different for the two cases. A difference of up to perhaps 0.06 should be acceptable.

The swerves due to oscillating α should be checked; these must be larger than a certain minimum value if C_{L_α}, the slope of the lift coefficient with varying α, is to be determined accurately.

The swerve due to average lift should be checked (only applies to lifting models). Verify that model will remain in view of the cameras.

Stress calculations for model and sabot need to be performed.

5. Calculating range simulation capabilities – example 1

To achieve similarity between the flight vehicle and the ballistic range model, one must have the same Reynolds number (Re) for both and the model motion must be dynamically similar to that of the flight vehicle. The dynamical similarity comprises dynamical similarity of pitching (and yawing) motion and of the slowing down of the model and vehicle due to drag. The pitching motion will be dynamically similar if λ/D for the model and the flight vehicle are equal, where λ is the wavelength of the pitching oscillation and D is the diameter of the model or flight vehicle. The slowing down due to drag will be dynamically similar if $\left.\frac{du}{u}\right|_{\lambda}$ for the model and the flight vehicle are equal, where u is the flight velocity and du is the change in flight velocity over the wavelength λ. In general, much more importance is given to pitching motion similarity than to drag slow-down similarity. Also, if pitching motion similarity is achieved, drag slow down similarity will not be too far off if r_g/D is not too different between the model and the flight vehicle, where r_g is the radius of gyration. Thus, in general, for ballistic range work, similarity between the model and the flight vehicle consists of matching each of Re and λ/D between the two cases.

The steps to make these calculations are given below. First, calculate λ/D for flight vehicle for each trajectory point to be tested using Eq. (1) below. [Equation (1) was derived from Eq. 7.140 of Ref. 1 by suppressing the minus sign of C_{m_α} and replacing the reference dimension l by the model diameter, D.]

$$\frac{\lambda}{D} = \sqrt{\frac{8\pi^2 I}{\rho A D^3 C_{m_\alpha}}} \qquad (1)$$

Equation (1) gives the normalized pitch oscillation wavelength in terms of the pitching moment of inertia of the vehicle, I, the gas density, ρ, the frontal area of the vehicle, A, the diameter of the vehicle, D, and the derivative of the pitching moment coefficient with respect to angle of attack, C_{m_α}. At this point, a rough, preliminary model design is necessary. This design would have the same shape, as close as is feasible, as the flight vehicle. The diameter could be set to 80% of that of the available gun, as a first cut. A material must be chosen for the majority of the model volume. This could be steel or aluminum or some other material. The model may need to be weighted to have the center of gravity in the location corresponding to that of the flight

vehicle. Note that both the model diameter and the model material may change during the design process. For the preliminary model design, calculate $\left(\frac{r_g^2}{D^2}\right)$. Then, the relation between λ/D and ρ_s/ρ for the model is calculated from

$$\frac{\lambda}{D} = \sqrt{\frac{8\pi^2}{C_{m_\alpha}} \frac{\rho_s}{\rho} \frac{V}{AD} \frac{r_g^2}{D^2}} \tag{2}$$

or

$$\frac{\lambda}{D} = K\sqrt{\frac{\rho_s}{\rho}} \tag{3}$$

where

$$K = \sqrt{\frac{8\pi^2}{C_{m_\alpha}} \frac{V}{AD} \frac{r_g^2}{D^2}} \tag{4}$$

(Note that ρ_s for the model in Eqs. (2) and (3) is not the same as ρ_s for the flight vehicle.) Since the flight vehicle and the model are assumed to be geometrically similar, V/AD is the same for both. Equation (3) is then rearranged as

$$\frac{\rho_s}{\rho} = \frac{1}{K^2} \frac{\lambda^2}{D^2} \tag{5}$$

The Reynolds number, Re, can be written as

$$\mathrm{Re} = \frac{\rho u D}{\mu} = \frac{\rho M c D}{\mu} \tag{6}$$

By manipulating equations (5) and (6), it can be shown that

$$\frac{\rho_s}{\rho} = \frac{1}{K^{2/3}} \left(\frac{\lambda M \rho_s c}{\mathrm{Re}\,\mu}\right)^{2/3} \tag{7}$$

Equation (7) defines two limiting lines for the facility in the ρ_s/ρ – Re plane. One line is for the maximum value of $\lambda\rho_s$ and the other for the minimum value of $\lambda\rho_s$. For the NASA Ames Hypervelocity Free Flight Aerodynamic Facility (HFFAF), 2 to 2.5 cycles in the 75 ft (22.86 m) long range has proven optimal. Two complete cycles are needed so that at least 4 extrema of the pitch and yaw oscillations can be seen at the 16 orthogonal shadowgraph stations. With four extrema, lines can be drawn joining the 2 positive extrema and the 2 negative extrema and the difference between the slopes of these lines allows the damping (or growth) of the oscillations in pitch and yaw to be accurately determined. (An example of a curve of pitch oscillation amplitudes varying down the range and the lines joining the extrema is shown in Fig. 4.) In addition, it is desirable to have at least 6 data points per cycle, which requires a minimum λ of 9.14 m (since the spacing of the shadowgraph stations is 1.524 m). (Six data points per cycle

are the minimum to reasonably accurately define the amplitude and wavelength of the oscillation. Seven or eight points would be better, if possible.) Thus, tests in the HFFAF are designed so that λ ranges between 9.14 and 11.43 meters.

Typical model densities range between 0.94 g/cm^3 (polyethylene) to 13 g/cm^3. The latter figure is based on machinable tungsten alloy (with a density of 17 g/cm^3) with enough margin to locate the CG correctly. An upper limit can be defined using the maximum, reasonable values of λ and ρ_s and, likewise, a lower limit can be defined using the minimum values for these two variables. To exceed the upper limit would require a ρ_s above 13 g/cm^3 (which is very difficult to achieve) or by increasing λ, so that there would be less than 4 extrema of the pitch oscillations during the model's flight within the range test section. To go below the lower limit requires a ρ_s less than 0.94 g/cm^3, or a reduced λ, so that there are fewer than 6 data points per pitch oscillation cycle.

We will use the supersonic flight test of the Low Density Supersonic Decelerator (LDSD)[2] project as an example to illustrate calculating the test simulation capability of a ballistic range. The LDSD flight tests were to demonstrate the feasibility of a Supersonic Inflatable Aerodynamic Decelerator (SIAD) for Mars entry. The SIAD is an inflatable torus attached to the outer rim of a capsule-like atmospheric entry vehicle. Figures 5 and 6 show the vehicle and the ballistic range model, respectively, in the SIAD-deployed configuration. Note that the ballistic range model is solid metal with shape representative of the inflated SIAD. For the flight vehicle at Mach 3.96, the range capability limits are shown in Fig. 7 as the two slanted limit lines with slopes Re α $(\rho_s/\rho)^{-1.5}$. Note that the LDSD is referred to as SIAD and SIAD-R in Ref. 2. However, not all of the area between these two diagonal limit lines is accessible to the facility since there are several other limiting factors. If the smallest acceptable λ is set at 9.14 meters and maximum model diameter is D = 3.56 cm (for models launched from the Ames 44.5 mm gun) and 4.88 cm (for models launched from the Ames 61 mm gun), these define limiting values of λ/D. Using Eq. (5), these translate into limiting values of ρ_s/ρ ~ 20,000 and 10,600, respectively. These limiting values appear as the vertical lines defining the leftmost sides of the facility capability zones in Fig. 7. One could conceivably extend the limit to the left by increasing D. This could put the integrity of the sabot at risk, since there would be very little sabot material left between the model and the gun bore. Likewise one could also extend the limit to the left of this line by decreasing λ. However, this would result in less than 6 data point per pitch oscillation cycle. There is another ρ_s/ρ value limit on the leftmost side of the facility capability zone. Since the maximum allowable test section pressure is 1 atm in air (Tests in other gases are typically done at sub-atmospheric pressure levels.), the maximum gas density is 1.194×10^{-3} g/cm^3. Using a minimum ρ_s of 0.94 g/cm^3 (polyethylene) yields a ρ_s/ρ of ~800. This limit lies well to the left the ρ_s/ρ values obtained previously from the λ/D values and thus, does not limit the facility capability.

Similarly, using the largest acceptable λ value of 11.43 meters and a minimum acceptable model diameter of 1.27 cm (based on acceptable resolution in the shadowgraphs). These define a limiting value of λ/D which translates into a limiting value of ρ_s/ρ of 2.45×10^5. This limiting value of ρ_s/ρ is shown as the vertical line to the right of the facility capability zone in Fig. 7. One could move to the right of this line by reducing D further. However, this could result in decreased accuracy of the data obtained, since the ratio (shadowgraph reading error)/(model diameter) would be reduced. One could also move to the right of this line by increasing λ, which would, however, result in having less than 4 extrema of the pitch oscillations within the range.

Another limit is the maximum possible Reynolds number (for a given Mach number) based on the maximum facility pressure and the maximum model diameter. For the 4.88 and 3.56 cm LDSD models with the inflatable deployed at Mach 3.96, these limits are shown as the horizontal lines near the top of the facility capability zone in Fig. 7. It is seen that the line for the 4.88 cm model truncates slightly the facility capability zone, while the line for the 3.56 cm model does not affect the corresponding facility capability zone. For a one atm maximum pressure

range like the HFFAF, one may move above the maximum Reynolds lines shown in Fig. 7 only by increasing D, which can be done only by 10% or so, and even that at the risk of compromising sabot integrity, as discussed previously.

At the topmost part of the facility capability zone, still another limit is encountered. From the definition of the Reynolds number, we write

$$\mathrm{Re} = \frac{uD}{\mu}\frac{\rho_s}{(\rho_s/\rho)} \tag{8}$$

Rearranging, we get

$$\rho_s = \frac{\rho_s}{\rho}\mathrm{Re}\frac{\mu}{uD} \tag{9}$$

Near the top of the facility capability zone defined by the leftmost vertical line and the topmost slanted line discussed previously, taking $D = D_{max}$, it is easy to show from Eq. (9) that there is a small region where the model density exceeds the maximum allowed density. This region is removed from the facility capability zone by adding the slanted lines with slopes $\mathrm{Re}\ \alpha\ (\rho_s/\rho)^{-1}$.

The various limits which may bound the facility simulation capability zone in the Re – ρ_s/ρ plane are enumerated below. Not all the limits affect the capability since some limits may fall outside other, more restrictive, limits.

(1) Two lines defined by Eq. (7) with slope -1.5 in the Re – ρ_s/ρ plane. One line is for $(\lambda\rho_s)_{max}$ and the other for $(\lambda\rho_s)_{min}$. The facility capability lies between the two lines.

(2) Two vertical lines determined by $(\lambda/D)_{max}$ and $(\lambda/D)_{min}$. The facility capability lies between the two lines.

(3) One vertical line defining the minimum ρ_s/ρ by ρ_{max} and $\rho_{s,min}$. The facility capability lies to the right of the line.

(4) One horizontal line at the maximum Re defined by D_{max} and the maximum facility pressure. The facility capability lies below the line.

(5) One line defined by Eq. (9) with slope -1 in the Re – ρ_s/ρ plane. This limit depends on the maximum value of ρ_s. The facility capability lies below the line.

The solid blue lines in Fig. 7 define the facility capability zone for Mach 3.96 and a maximum model diameter of 3.56 cm. For a maximum model diameter of 4.88 cm, the facility capability zone extends further upwards and to the left, enclosed by dashed blue lines. For the D_{max} = 3.56 cm case, the limits which appear in Fig. 7 are, from the above list, (1) (both lines), (2) (leftmost line) and (5). For the D_{max} = 4.88 cm case, the limit (4) also appears.

We next place the flight trajectory points on the ρ_s/ρ – Re plane of Fig. 7. For each trajectory point λ/D is calculated using Eq. (1). Then, for the preliminary model design, $\frac{r_g^2}{D^2}$ is determined for the model. K is then calculated from Eq. (4), ρ_s/ρ from Eq. (5) and the Reynolds number from Eq. (6). The red data points show the flight trajectory data points for the Mach number range 2.37 – 3.96. It should be pointed out that the ρ_s/ρ values for the trajectory points plotted on the facility capability plot of Fig. 7 are not the same as the actual flight ρ_s/ρ values. This is because

$\frac{r_g^2}{D^2}$ is different for the flight vehicle and the model. (For the flight vehicle, $\frac{r_g^2}{D^2}$ is 0.0421 and for the preliminary model design considered herein, $\frac{r_g^2}{D^2}$ is 0.0599 – the difference being due to the light inflatable surrounding the centerbody of the flight vehicle. This is very difficult to simulate in the ballistic range, since the model, shown in Fig. 6, is of solid metal construction.) The priority is given to having the correct dynamic similarity of the pitch oscillations (i.e., equal λ/Ds) rather than the correct dynamic similarity of the drag slow down, which would be obtained if the ρ_s/ρ values were matched between the flight vehicle and the model. (See discussion of velocity drops presented in Sec. 7.) For the flight trajectory under discussion here, and the range simulation of the same, the key parameters are given in Appendix A to enable the reader to follow through the analyses presented herein with numerical data and results.

We see from Fig. 7 that the flight trajectory point for Mach 3.96 is well within the facility capability zone and therefore, in principle, this flight trajectory can be simulated exactly in the HFFAF ballistic range. In Fig. 8, we show the flight trajectory again, along with the facility capability zones for Mach 2.37 and 3.96 for a 3.56 cm diameter maximum model size. We see that the flight trajectory point at Mach 2.37 is again well within the facility capability zone. In principle, all of the flight trajectory points can be simulated exactly in the HFFAF ballistic range.

This, however, is not feasible in practice because it would necessitate different model mean densities, diameters and sabot designs for each Mach number, resulting in an extremely expensive and time-consuming test entry. In the present example, since the critical event, parachute deployment, occurs at the lower end of the Mach number range, it was decided to try to provide a close range match to the flight condition at Mach 2.37. For this condition, the calculated λ/D for pitch oscillations is 331. Taking λ to be 11.43 m (giving two oscillation cycles in the range), D would be 3.45 cm. We chose a slightly larger value of D, 3.56 cm, which is 80% of the gun bore diameter. (The larger the model diameter, the less likely the model is to be disturbed or kicked by the enclosing sabot when the sabot is discarded.) With this model diameter, matching the Reynolds number gives a required pressure in the range of 170 Torr. Matching the density ratio gives a model density of 7.35 g/cm^3. Hence, steel, with a density of 7.80 g/cm^3, was chosen as the model material. This defines one point on the green curve in Fig. 8. The remaining points on the green curve were defined by choosing the range pressure for each Mach number to keep the same pitch oscillation wavelength – that is, to maintain 2 pitch oscillations in the length of the range. By moving from the red curve to the green curve (i.e., from an impractical test entry to a practical test entry) one gives up the possibility of obtaining (in principle) an exact match of ρ_s/ρ and Re between the model and the flight vehicle for each Mach number.

The above procedure provides very good simulation around Mach 2.37, with parameter mismatches of the order of 10%. At the higher Mach numbers, the mismatches can be as large as 20% for ρ_s/ρ and 35% for Re. We note that the actual ballistic range Mach numbers, 2.08 to 3.65, are slightly lower than the flight trajectory Mach numbers originally studied. Figure 9 shows an expanded version of Fig. 8, showing the variable (impracticable) model and final (single model) trajectories in more detail. Taking the green data point at Mach 3.0 as an example, it can be seen that by reducing the range pressure (moving along the purple curve), we can get much closer to the desired ρ_s/ρ and Re values. While this may appear to be desirable, it reduces the number of oscillation cycles in the range and, hence, was rejected as an option.

The analysis discussed above for the LDSD model with the inflatable deployed configuration was repeated for the LDSD model with the inflatable stowed configuration. The vehicle and the ballistic range model are shown in Figs. 10 and 11, respectively. The resulting trajectory point at Mach 3.45 and the facility capability zone for this case are shown in Fig. 12. It is seen that the flight data point is outside the capability zone of the facility. For this case, with λ/D for pitch

oscillations of 661 and two pitch oscillations in the length of the range, the model diameter would be 1.73 cm. The required model density is 23.8 g/cm^3, which is unattainable. Since a 20 mm gun was available, a model diameter of 85% of the gun caliber, or 1.698 cm, was selected. This is only slightly less than the value for the flight data point in Fig. 12. The model was designed to be fabricated primarily of a machinable tungsten alloy with a density of 17 g/cm^3 with a steel "anti-weight" in the nose to properly locate the center of gravity. This resulted in a mean model density of 14.24 g/cm^3. To have two cycles in the range, the required range pressure was calculated to be 195 Torr, which determines the range model Reynolds number and the range model density ratio, ρ_s/ρ. These values then determine the location of the upper green data point in Fig. 12. The lower green data point represents the range condition for some shots which were made at Mach 3.15 rather than at Mach 3.45. For the data point at Mach 3.45, the mismatches are ~20% for density ratio and 30% for Reynolds number.

6. Calculating range simulation capabilities: example 2 – the High-Energy Atmospheric Reentry Test (HEART)

The analysis of Sec. 5 was repeated for the proposed HEART vehicle. The HEART vehicle is shown in Fig. 13 and is a low density decelerator comprised of a centerbody surrounded by an inflatable cone made up of 12 tori. As will be seen, with the HEART vehicle and trajectory, there is more difficulty in obtaining dynamic similarity and Reynolds number matching than with the LDSD vehicle and trajectory. The normalized masses (mass divided by diameter cubed) of the HEART vehicle and the LDSD vehicle with the inflatable deployed are both in the range of 6 to 8 kg/m^3. Thus, the vehicles are rather similar to each other and the difference in the difficulty in obtaining dynamic similarity and Reynolds number matching is primarily due to the different trajectories for the two vehicles.

The HEART flight test will have as primary objectives testing the robustness of the fabric tori with respect to heating and aerodynamic forces. The static and dynamic stability of the vehicle are also of importance and can be assessed in the ballistic range prior to the flight test. The Mach numbers of interest for the HEART ballistic range stability tests are 0.8 to 2.0. Figure 14 shows the flight trajectory of the HEART vehicle and the simulation capabilities of the HFFAF range. Figure 14 is analogous to Fig. 7 for the LDSD vehicle with the inflatable deployed, except that facility capability data for the two extreme Mach numbers are shown in Fig. 14. We see that, unlike the case for the LDSD vehicle with the inflatable deployed, the trajectory of the HEART vehicle lies well outside the capability of the HFFAF range, especially if one is limited to using the 44 mm gun (the Ames powder gun with the most extensive user database). The HFFAF range, particularly with the 44 mm gun, falls well short of the flight Reynolds number requirements and far off the flight ρ_s/ρ values. With a decelerator flying at a low ρ_s/ρ, the oscillations in pitch are relatively much more rapid than with a decelerator flying at a high ρ_s/ρ, and the λ/D values are correspondingly much smaller, leading to the problem that there are far too few data stations per cycle to capture the pitch oscillations accurately. A measure of the capability of a range to capture the pitch oscillations is the station spacing divided by the largest model diameter (which we have been taking as 0.80 times the caliber of the largest gun). Characteristics of the Ames HFFAF range and three 1 atm open ranges are given in Table 1 below. (The Ames GDF range is located in the same complex as the Ames HFFAF range; the Eglin ARF range is located at Eglin Air Force Base, Florida and the DRDC range is located at DRDC, outside of Quebec City, Quebec, Canada. As of November, 2016, the Eglin range is no longer operational.)

Table 1. Characteristics of various ballistic ranges.

Range	Range length (m)	Station spacing, Δx (m)	Gun (mm)	Max model diameter, D (cm)	$\Delta x/D$
Ames HFFAF	22.9	1.52	44	3.56	42.9
Ames HFFAF	22.9	1.52	61	4.88	31.3
Ames GDF	4.88	0.098*	44	3.56	2.74
Ames GDF	4.88	0.098*	61	4.88	2.00
Eglin ARF	201	3.38†	76	6.10	55.5
DRDC	135	2.50	110	8.80	28.4
DRDC	135	2.50	155**	12.40	20.2

*Small station spacing achieved by having each of 8 cameras take 12 – 14 images
**155 mm gun is currently rifled, would have to be smooth bored to do aerodynamic range work
†Average station spacing for first 91 m of range length

In regard to capturing short wavelength pitch oscillations, the ARF range has less capability than the Ames HFFAF, while the DRDC range has some advantage over the HFFAF range, particularly if the 155 mm gun could be brought into service. In this respect, the Ames GDF range has a very great advantage over the Ames HFFAF range. The Ames GDF range does have limitations due to its short length, however. An important comparison will be to place the capabilities of the other three ranges on the graph of Fig. 14. However, before doing that, we discuss how the capabilities of a 1 atm range appear on the ρ_s/ρ – Re plane.

Figure 15 shows the capabilities of the Ames GDF range for the HEART vehicle at the Mach 0.8 flight data point, using the Ames 44 mm powder gun. These capabilities were calculated for a single material ballistic range model, assumed for model robustness. The limiting lines are established, in part, by limits on model diameters and pitch oscillation wavelengths. The maximum model diameter is taken to be 3.56 cm, which is 80% of the gun diameter. The minimum model diameter is taken to be 1.27 cm, based on having sufficient resolution in the photos of the model. (For the GDF ICCD camera system, this corresponds to having 10 pixels across the diameter of the model, which was judged to be the minimum to obtain acceptable position and angle data quality.) The maximum wavelength is taken to allow 2 cycles within length of the range. The minimum wavelength is taken to be that which allows data points at 6 stations per cycle.

The horizontal boundaries in Fig. 15 are established by the maximum and minimum model diameters, with the known model velocity, air density and viscosity. One criterion for the left side vertical boundary is established using the minimum wavelength and the maximum model diameter and then translating to ρ_s/ρ using Eq. (3). Another criterion is ρ_s/ρ based on the assumed lowest model density of 0.94 g/cm^3 (polyethylene). The larger of these two values is used to establish the left side vertical boundary. One criterion for the right side vertical boundary is established using the maximum wavelength and the minimum model diameter and then translating to ρ_s/ρ using Eq. (3). Another criterion is ρ_s/ρ based on the assumed highest model density of 13.0 g/cm^3 (machinable tungsten alloy with sufficient margin for an anti-weight to position the center of gravity in the correct location). Whichever of these two values is the smaller is used to establish the right side vertical boundary.

For the inclined boundaries, we take Eq. (7), cube both sides of the equation and then divide both sides of the equation by $(\rho_s/\rho)^2$. This yields

$$\frac{\rho_s}{\rho} = \left(\frac{1}{K} \frac{\lambda M \rho c}{\mathrm{Re}\,\mu} \right)^2 \qquad (10)$$

Note that ρ is a constant for a 1 atm range. Also, note that ρ_s/ρ now varies as $(1/Re)^2$, whereas in Eq. (7), ρ_s/ρ varies as $(1/Re)^{2/3}$. For the upper inclined boundary, Eq. (10) is evaluated at the maximum λ and at the lower inclined boundary, Eq. (10) is evaluated at the minimum λ.

Figure 16 shows the HEART flight trajectory (red) and the simulation capability of the Ames HFFAF range for the Mach 2 flight condition in blue. The simulation capabilities of the Ames GDF range are shown in green and those of the DRDC range in purple. Note that the simulation capability box of the DRDC range using its 155 mm gun does not show 6 boundary lines like the capability box shown in Fig. 14, since the relative positions of the limit lines causes some of the them to disappear. Also, for the DRDC range using its 110 mm gun, the lines squeeze together to such an extent that essentially only one capability point remains. Because of the high $\Delta x/D$ value for the Eglin ARF range (see Table 1), no simulation capability of that range appears in Fig. 16. A relaxation of one of our criteria (such as allowing less than 6 data points per pitch oscillation cycle) would be necessary for a simulation capability of the ARF range to appear in Fig. 16. Figure 17 shows the corresponding plot for the Mach 0.8 flight condition.

For the Mach 2 flight condition, we consider the best facility operating condition within the simulation capability of each range/gun combination. From Fig. 16, we then note a progressive improvement in the Reynolds number and density ratio simulation as one moves up in gun size from 44 mm to 61 mm to 110 mm to 155 mm. Within the HFFAF capabilities, the 61 mm gun does substantially better than the 44 mm gun. The DRDC range can come quite close to the flight conditions. The Ames GDF range can match the density ratio but would be a factor of ~4 short of the flight Reynolds number. More details relating to the preceding discussion are given in Table 2. In Tables 2 and 3 below, $R = \rho_s/\rho$, ρ_{sr} is the ballistic range model density and P_r is the range pressure. (R is used for clarity in Tables 2 and 3.)

Table 2. Key parameters for simulation of HEART flight condition at Mach 2.0 in various facilities with various guns.

Range	Gun (mm)	Re_f	R_f	Re_r	R_r
HFFAF	44	3.49×10^6	7270	0.674×10^6	26,000
HFFAF	61	3.49×10^6	7270	1.74×10^6	13,800
DRDC	110	3.49×10^6	7270	4.07×10^6	11,340
DRDC	155	3.49×10^6	7270	5.00×10^6	7270
GDF	44/20	3.49×10^6	7270	0.83×10^6	7270

Table 2 (continued). Key parameters for simulation of HEART flight condition at Mach 2.0 in various facilities with various guns.

Range	Gun (mm)	D_r (cm)	ρ_{sr} (g/cm^3)	P_r (Torr)	Mismatch of Re, Re_f/Re_r	Mismatch of R, R_r/R_f
HFFAF	44	3.56	13.0	319	5.18	3.57
HFFAF	61	4.88	13.0	600	2.00	1.90
DRDC	110	8.8	13.5*	760	0.858	1.56
DRDC	155	11.2	8.68	760	0.698	1.00
GDF	44/20	1.85†	8.68	760	4.20	1.00

†Could perhaps use 20 mm gun

*If ρ_s = 13 g/cm^3, only 5.88 points per oscillation cycle would be obtained

For the Mach 0.8 flight condition, as for the Mach 2 flight condition, a progressive improvement in Reynolds number and density ratio simulation as one moves through the increasing diameters of the Ames guns in the HFFAF range to the DRDC guns in the DRDC range is noted. However, in this case, even the best DRDC simulation is short of the flight Reynolds number by a factor of 2.2 and off density ratio by a factor of 3.3. The Ames GDF can match the flight density ratio, but is well short of the flight Reynolds number (by a factor of 7.6). More details relating to the preceding discussion are given in Table 3.

Table 3. Key parameters for simulation of HEART flight condition at Mach 0.8 in various facilities with various guns.

Range	Gun (mm)	Re_f	R_f	Re_r	R_r
HFFAF	44	5.04×10^6	2034	0.231×10^6	30,260
HFFAF	61	5.04×10^6	2034	0.596×10^6	16,090
DRDC	110	5.04×10^6	2034	1.63×10^6	13,230
DRDC	155	5.04×10^6	2034	2.29×10^6	6690
GDF	44†	5.04×10^6	2034	0.66×10^6	2034

Table 3 (continued). Key parameters for simulation of HEART flight condition at Mach 0.8 in various facilities with various guns.

Range	Gun (mm)	D_r (cm)	ρ_{sr} (g/cm^3)	P_r (Torr)	Mismatch of Re, Re_f/Re_r	Mismatch of R, R_r/R_f
HFFAF	44	3.56	13.0	273	21.8	14.9
HFFAF	61	4.88	13.0	514	8.45	7.91
DRDC	110	8.8	15.8*	760	3.10	6.50
DRDC	155	12.4	7.99	760	2.20	3.29
GDF	44†	3.56	2.43	760	7.64	1.00

*If ρ_s = 13 g/cm^3, only 5.44 points per oscillation cycle would be obtained; if ρ_s = 14.24 g/cm^3 could be obtained, as was done for the LDSD stowed model, then the number of points per cycle would increase to 5.70.

Tables 2 and 3 give the required size of the model (D_r) for each possible condition of choice. Also given are the required model densities. Models with densities of 13 g/cm^3 (and above) would likely be fabricated mainly out of machinable tungsten alloy, with a density of 17 g/cm^3. Several ballistic range models in the tables have required densities of 8 – 8.7 g/cm^3. These could be fabricated mainly of steel (7.8 g/cm^3) or brass (8.7 g/cm^3). In one case, the required model density is 2.43; this model could be fabricated mainly of aluminum (2.7 g/cm^3). Internal hollows in the model or magnesium (1.8 g/cm^3) inserts could bring the density down to that required value.

The choice of which range (and gun) to be used will depend upon many factors, two of which are:

Relative importance placed on Reynolds number and density ratio mismatch. (The density ratio mismatch translates to a mismatch in λ/D, the normalized pitch oscillation wavelength.)

The increasing expenses for the models, sabots and gun operation as the gun size increases.

The best choice of range and gun for HEART type vehicles depends upon the relative weighting given to the various factors and hence, we make no attempt to give a definitive answer here.

7. Determination of decrease in velocity and Mach number per cycle of pitch/yaw oscillations and during traverse of the range test section

If the model has the same r_g/D as the flight vehicle, and λ/D is matched, the fractional velocity drop per pitch oscillation cycle will be the same for the flight vehicle and the model. Thus, the deceleration of the flight vehicle and the model will be dynamically similar. For some vehicles, particularly those with inflatable or deployable aerobrakes, it may not be feasible, with a robust gun-launched model, to have r_g/D the same for the flight vehicle and the model. The fractional velocity drop per cycle can be calculated from the following equations, starting with Newton's law, force (F) = mass (m) x acceleration (a). The aerodynamic drag force is given by

$$F = C_D A \frac{1}{2} \rho u^2 \tag{11}$$

The mass times acceleration term is given by

$$ma = m\frac{du}{dt} = mu\frac{du}{dx} \tag{12}$$

where t is time and x is distance along the flight trajectory. From Eqs. (11) and (12), we get

$$\frac{du}{u} = \frac{C_D A \rho}{2m} dx = \frac{C_D A \rho}{2V \rho_s} dx \tag{13}$$

Evaluating du/u for dx = the wavelength, λ, using Eq. (2), we get

$$\left.\frac{du}{u}\right|_\lambda = \pi C_D \sqrt{\frac{AD}{V}\frac{\rho}{\rho_s}\frac{2}{C_{m_\alpha}}}\frac{r_g}{D} \tag{14}$$

Applying Eq. (2) once more, we get

$$\left.\frac{du}{u}\right|_\lambda = 4\pi^2 \frac{C_D}{C_{m_\alpha}}\left(\frac{r_g}{D}\right)^2 \frac{D}{\lambda} \tag{15}$$

For the LDSD vehicle with the inflatable deployed and the conditions discussed in Sec. 5 with Mach numbers from 2.37 to 3.96, the fractional velocity drop per cycle is ~0.04 for the flight vehicle and ~0.05 for the ballistic range model. These differences between these small velocity drops very likely has a negligible effect on the simulation of dynamic similarity between the model and the flight vehicle. For the HEART vehicle, with a large inflatable, the velocity drops per cycle are larger, being ~0.14 for the flight vehicle and ~0.20 for the model. These differences still may be acceptable for sufficiently accurate dynamic similarity.

The fractional velocity drop may be reduced by decreasing the model diameter D, while maintaining λ. However, this moves one away from λ/D pitch oscillation similarity and reduces

the Reynolds number, both of which are undesirable. For example, let D be reduced to 0.8 of its original value, while λ is maintained, which can be done by decreasing ρ to 0.64 of its original value. This would reduce the fractional velocity drop by 20%, but would also put λ/D off dynamic similarity by 20%. Further, the Reynolds number would be reduced to 0.51 of its original value, a 49% reduction.

If it is desired to move the model r_g/D closer to the flight vehicle r_g/D to achieve closer dynamic similarity of the velocity drop, this can, in principle, be done by building a two-material model, say of magnesium and steel. Such a model would be much more complex than a single-material model and may be difficult to make sufficiently robust to survive the gun launch process. There may be a strong tendency for such a model to come apart at the joint between the two materials.

Reference 3 gives other useful velocity drop criteria. One criterion of this reference is that the Mach number change (drop) on traversing the range test section should be less than 0.2. We take the fractional velocity drop per oscillation cycle from Eqn. (15) and transform to get

$$\left.\frac{dM}{\bar{M}}\right|_{range} = \left.\frac{du}{u}\right|_{\lambda} \frac{L}{\lambda} \tag{16}$$

where M is the Mach number and L is the length of the range. From Eq. (16), we get

$$dM_{range} = \bar{M}_{range} \left.\frac{du}{u}\right|_{\lambda} \frac{D}{\lambda}\frac{L}{D} \tag{17}$$

For the LDSD model with the inflatable deployed, for the conditions discussed in Sec. 5 with Mach numbers from 2.37 to 3.96, the Mach number drop on traversing the range from Eq. (17) ranges from 0.24 to 0.32. These drops somewhat exceed the suggested limit of 0.20 of Ref. 3. For the HEART model shown in Table 2 of Sec. 6, in the NASA Ames GDF facility over the Mach number range of interest (Mach 2.0 to Mach 0.8), the Mach number drops on traversing the range are much larger, ranging from 0.52 to 0.58. This model is a relatively light model and slows down very rapidly – hence, the large Mach number drops are unavoidable, unless one moves well away from dynamic (λ/D) similarity between the model and the flight vehicle.

A second criterion given in Ref. 3 is that the Δx due to deceleration in the range, i. e., the difference between the distance travelled by the actual model and the distance travelled by a model with zero deceleration, be greater than a certain value, which is given as 2.5 cm for the NASA Ames HFFAF facility. This limit is a lower limit for measurability. This limit corresponds to accuracy of 0.013 cm in measurements of the model position in the shadowgraphs and a time measurement accuracy of 0.02 microseconds. Δx can be calculated from Eq. (18):

$$\Delta x = \frac{1}{2}\left.\frac{dM}{\bar{M}}\right|_{range} L \tag{18}$$

For the LDSD model with the inflatable deployed and the HEART model discussed in the preceding paragraph, Δx is between 60 and 160 cm, much larger than the minimum Δx criterion (2.5 cm) given in Ref. 3. Hence, for these models, there will be no problem regarding this criterion.

For the LDSD vehicle with the inflatable deployed and the range simulation of same, the key parameters necessary for the calculation of $\left.\frac{du}{u}\right|_{\lambda}$, dM_{range} and Δx and the results themselves are given in Appendix B.

8. Determine swerve due to oscillating lift caused by pitch (or yaw) oscillations

Following the treatment of Ref. 4, we estimate the swerve due to the oscillating lift caused by pitch (or yaw) oscillations. This swerve will be compared to the estimated precision with which the model position can be measured to assess the accuracy with which the lift coefficient slope (C_{L_α}) can be determined. We consider the pitch angle of attack (α) to be oscillating sinusoidally:

$$\alpha = \alpha_{\max} \sin\left(\frac{2\pi x}{\lambda}\right) \tag{19}$$

where x is the distance along the range. The lift (L) at an angle of attack α is given by:

$$L = C_{L_\alpha} \alpha \frac{1}{2} \rho u^2 A \tag{20}$$

Combining Eqs. (19) and (20), we get:

$$L = C_{L_\alpha} \alpha_{\max} \sin\left(\frac{2\pi x}{\lambda}\right) \frac{1}{2} \rho u^2 A \tag{21}$$

Using Force = Mass x Acceleration, we get

$$\ddot{y} = L / m \tag{22}$$

where $\ddot{y}$ is the acceleration perpendicular to the flight path. Combining Eqs. (21) and (22) and using x = ut (assuming constant velocity), where t is time, we get

$$\ddot{y} = \frac{C_{L_\alpha} \alpha_{\max}}{m} \sin\left(\frac{2\pi u t}{\lambda}\right) \frac{1}{2} \rho u^2 A \tag{23}$$

Integrating twice and evaluating at the maximum of the sine function, we get

$$y_{\max} = \frac{C_{L_\alpha} \alpha_{\max}}{m} \frac{\lambda^2 \rho A}{8\pi^2} \tag{24}$$

where y_{max} is the maximum swerve due to the oscillating lift. Substituting for λ from Eq. (1), we get:

$$y_{\max} = \frac{C_{L_\alpha} \alpha_{\max}}{m} \frac{I}{D C_{m_\alpha}} \tag{25}$$

Using $I = m r_g^2$, we get

$$y_{\max} = \frac{C_{L_\alpha}}{C_{m_\alpha}} \alpha_{\max} D \left(\frac{r_g^2}{D^2} \right) \tag{26}$$

Using Eq. (26), we can evaluate y_{max} for the LDSD model with the inflatable deployed and the HEART model discussed in the previous section. As was mentioned previously, the accuracy of the position measurements in the NASA Ames HFFAF facility is given in Ref. 4 as 0.013 cm. For an example given in Ref. 4, with an α_{max} of 10 degrees, a y_{max} of 0.5 cm is calculated. With the measurement accuracy of 0.013 cm, the maximum swerve displacement was about 40 times the measurement accuracy. For the LDSD model in the NASA Ames HFFAF facility, y_{max} was estimated as 0.19 to 0.25 cm, being 15 to 19 times the measurement accuracy. For the HEART model in the NASA Ames GDF facility, y_{max} was estimated to be 0.13 to 0.18 cm. If the measurement accuracy of the Ames GDF facility is taken to be equal to that for the Ames HFFAF facility (0.013 cm), the estimated y_{max} values are 10 to 14 times the measurement accuracy. These y_{max} values are not as favorable as those in the example given in Ref. 4 and point to the difficulty in getting good lift curve data. The problem becomes more severe at smaller α_{max} values, such as 5 degrees or 2 degrees. Unfortunately, the parameters C_{L_α}, C_{m_α} and r_g/D in Eq. (26) are characteristic of the model and cannot really be changed significantly. D is usually constrained by the size of the launchers and by the need to have an adequate number of oscillation cycles in the range.

For the LDSD vehicle with the inflatable deployed and the range simulation of same, the key parameters necessary for the calculation of y_{max} and the y_{max} values themselves are given in Appendix C.

It is concluded that for testing the LDSD model with the inflatable deployed in the HFFAF and the HEART model in the GDF, errors of the order of 5 to 10% in the lift coefficient slope may occur due to measurements inaccuracies when α_{max} is ~10 degrees. Errors would be greater at smaller α_{max} values and less at larger α_{max} values. In such cases, one needs to make every effort to get accurate swerve measurements.

9. How to determine swerve due to lift for lifting models

If the model lifts, one can determine the (vertical) swerve due to lift down the length of the range. The equations to determine the swerve follow. Again starting with Newton's law F = ma, the aerodynamic lift force is

$$F = C_L A \frac{1}{2} \rho u^2 \tag{27}$$

The lateral acceleration a is, then

$$a = \frac{C_L A \frac{1}{2} \rho u^2}{m} \tag{28}$$

The swerve, y, over a time of flight t over a range length L is, assuming constant u,

$$y = \frac{1}{2} a t^2 = \frac{1}{2} a \frac{L^2}{u^2} \tag{29}$$

Combining Eqs. (28) and (29) and using m = $\rho_s V$, we get

$$y = \frac{1}{4} C_L \frac{L^2}{D} \frac{AD}{V} \frac{\rho}{\rho_s} \tag{30}$$

Using Eq. (2) with Eq. (30), we obtain

$$\frac{y}{L^2} = 2\pi^2 \frac{C_L}{C_{m_\alpha}} \frac{r_g^2}{D^2} \frac{D^2}{\lambda^2} \frac{1}{D} \tag{31}$$

and

$$y = 2\pi^2 \frac{C_L}{C_{m_\alpha}} \frac{r_g^2}{D^2} \frac{D^2}{\lambda^2} \frac{L}{D} L \tag{32}$$

Note that the length, L, in equations (29) to (32), must be the length from the gun muzzle to the last data station rather than the distance from the first to the last data station. For the Ames HFFAF, L is 32.92 m. For the Ames HFFAF, the maximum lift swerve allowable before the model lifts out of the field of view of the last shadowgraph station is 17 cm. By tilting the gun downwards (at angles up to ~1 degree) so that the model first dives down, then levels out and then starts to rise upwards along the length of the range, the maximum allowable lift swerve can be increased by almost a factor of three to 47 cm. In three test campaigns[6-8], by tilting the gun, models with lift coefficients of 0.3 - 0.6, ~0.35 and ~0.4 were successfully tested in the Ames HFFAF. The corresponding lift/drag ratios ranged from 0.25 to 0.51. It should be pointed out that the tests of Refs. 6 and 8 were performed in the Ames HFFAF, while the tests of Ref. 7 were performed in the Ames GDF facility (see Sec 6). At the present time, it is only possible to tilt the powder guns and not the two-stage light gas guns.

Models with higher L/Ds may be tested by decreasing the model diameter D, decreasing ρ or increasing ρ_s (or a combination of these steps), but this moves one away from λ/D pitch oscillation similarity and reduces the Reynolds number. Due to the small size of the ballistic range models, the Reynolds numbers are often already somewhat below the flight values. Hence, a further reduction in Reynolds number is usually undesirable. Table 4 shows the normalized variables for several techniques which could be used to reduce swerve (s = normalized swerve). Cases 1 to 4 show techniques for reducing the swerve by 20%. For case 1,

Table 4. Normalized variables (baseline variables = 1) for several techniques to reduce swerve.

Notes	ρ_s/ρ	ρ	ρ_s	D	λ	λ/D	Cycles	Re	s
Baseline	1	1	1	1	1	1	1	1	1
Case 1	1	1	1	0.8	0.8	1	1.25	0.8	0.8
Case 2	1.56	0.64	1	1	1.25	1.25	0.8	0.64	0.8
Case 3	1.56	1	1.56	1	1.25	1.25	0.8	1	0.8
Case 4	1.25	0.8	1	0.894	1	1.12	1	0.72	0.8
Case 5	2.0	0.5	1	0.707	1	1.414	1	0.35	0.5

the diameter is reduced by 20%, which leaves the dynamic similarity unchanged, reduces Re by 20% and increases the number of cycles by 25%, which may or may not be acceptable. For

case 2, the same reduction in the swerve is achieved by decreasing the gas density. Here the penalties are more severe, λ/D is increased by 25%, Re is decreased by 36% and the number of cycles is reduced by 20%. The reduction in the number of cycles may result in less than 4 extrema of the pitch oscillation angles within the length of the range and a consequent reduction in the accuracy of the determination of the growth or decay rate of the pitch angle oscillations. If it is possible to increase ρ_s by 56%, one may arrive at Case 3. Here, Re is unchanged, but λ/D increases by 25%, which decreases the number of cycles by 20%. For case 4, both ρ and D are decreased, which permits one to maintain λ and the number of cycles. The penalties are a 28% reduction in Re and a 12% increase in λ/D. Since the cycles can be maintained for the technique of case 4, that case was extended to achieve a more substantial reduction in s (by a factor of 2) in case 5. Here, the Reynolds number penalty is severe, by almost a factor of 3. Also, λ/D is increased above its baseline value by 41%.

Models with much higher L/D values can be tested in the Ames GDF facility, but this range is a short (4.88 m) open (1 atm) ballistic range, which limits model size and the ability to achieve dynamic and Reynolds number similarity.

One method of making a model lift is to insert a weight (and/or "antiweight" – a weight with a density less than that of the bulk model material) which is located off the centerline of the model. This causes the model to trim at an angle of attack, producing lift. In some cases, when the weight was placed above the centerline of the model, the model was found to roll and, hence, to lift sideways out of the field of view. This problem was solved by reversing the model so that the weight was below the model centerline. This change, of course, reversed the direction of lift of the model.

For the LDSD vehicle with the inflatable deployed and the range simulation of same, the key parameters necessary for the calculation of y and the y values themselves are given in Appendix D. To illustrate this procedure, in the Appendix, we have assumed that C_L = 0.23. The actual C_L for this vehicle is zero and hence y for the actual, non-lifting vehicle (and model) would be zero. The vehicle (and model) would have to be weighted off-center to produce a non-zero C_L.

10. Model design – materials, weights

Table 5 shows materials frequently used to fabricate ballistic range models. Most of these materials have been successfully used by the present author. In most cases, a material can be

Table 5. Materials for ballistic range models

Material	Compound, alloy, remarks	Density, g/cm^3
TPX	Polymethyl pentene	0.835
UHMW Polyethylene	(UHMW = ultra high molecular weight)	0.94
ABS, high impact	Acrylonitrile-Butadiene-Styrene	1.04
ST-801 Nylon	Poly-amide, DuPont	1.08
Delrin, toughened	Acetal	1.34
Magnesium	ZK60A-T5	1.83
Aluminum	7075-T6	2.80
Titanium	Ti-6Al-4V	4.43
Steel	4140	7.83
Steel	17-4 PH stainless	7.81
Brass	70 Cu/30 Zn	8.53
Tungsten	Machinable alloy, Kulite K1700 or equivalent	17.00

chosen which has a density close to the desired density calculated in sections 5 and 6. In some cases, two-material models, screwed or press fit together may be required to achieve the desired average model density.

In many cases, a two- (or three-) material model is required to properly place the center of gravity (CG) of the model in the correct axial location. To do so, a nose weight or "anti-weight" is often required. The nose weight may be press-fit into the main model body or the model can be made in several pieces and screwed together. Figure 18 (see Ref. 5) shows a model with a press-fit nose "anti-weight". Similarly, to offset the CG from the axial centerline so as to generate lift, weight/"anti-weights" can be press-fit sideways into the main body of the model. Figure 19 (see Ref. 6) shows a model with such a press-fit weight and an "anti-weight" to laterally offset the CG. The same type of CG offset can be obtained by a sideways offset weight trapped by a threaded retainer as shown in Fig. 20 (see Ref. 7). We note that by proper selection of the axial positions of the weights and "anti-weights" shown in Figs. 19 and 20, the presence of these weight/"anti-weights" can also be used to adjust the axial location of the CG as required. Figure 21 (see Ref. 8) shows a three piece tabbed model. Several methods of adjusting the CG location in this model are possible. Small changes in the axial position of the CG can be made by adjusting the sizes of the cavities A and B. A large change in the axial position of the CG was made by changing from a brass forebody to an aluminum forebody while also changing from a ABS plastic afterbody to an aluminum afterbody. The CG is obviously offset laterally by the presence of the tab. However, considerable additional lateral CG offsets can be made by adjusting the sizes of the cutouts C and D.

11. Sabot design – materials

Table 6 shows materials used for sabots for ballistic range models. The first three materials have frequently been used and have been successfully used by the present author. The ST-801

Table 6. Materials for ballistic range sabots

Material	Compound, alloy, remarks	Density, g/cm^3
ABS, high impact	Acrylonitrile-Butadiene-Styrene	1.04
ST-801 Nylon	Poly-amide, DuPont	1.08
Lexan, Zelux	Polycarbonate	1.20
Radel R5500	Polyphenylsulfone	1.29

"super tough" Nylon has, in general, given us good service. However, unexpected failure has occasionally occurred with this material. The impact strength of plastics are frequently measured by the notched Izod impact test (ASTM D256). The Izod value for ST-801 Nylon is quoted by DuPont as 17 – 20 ft-lbf/in. Izod tests that were made for doubtful batches of Nylon have given values as low as 5 – 6 ft-lbf/in. Thus, for severe launch conditions, it may be desirable to have Izod tests performed before fabricating components from ST-801 Nylon so as to ensure their performance. As a standard practice in the HFFAF, at least 5 Izod specimens are made and tested. Ideally, some specimens should be cut in all three possible orientations. However, it is realized that for round stock or flat stock with a maximum dimension of less than 2.5", only two orientations of the Izod specimens are possible.

For moderate launch conditions, ABS has given us good service. One must be sure to obtain "high impact" ABS with Izod values of 5 – 7 ft-lbf/in, rather than "medium impact" ABS with Izod values of 2 – 4 ft-lbf/in. The tensile strength of ABS is given as about 6 ksi, nearly the same as that of ST-801 at 2.3% water content. (This water content occurs when the Nylon is in equilibrium at 50% relative humidity air.) The density of ABS is slightly less than that of ST-801.

Our current policy is to use ABS (and sometimes ST-801) for moderate launches and ST-801 for more severe launches. If the ST-801 is tested and proven to have the claimed Izod values, it has roughly 3 times the impact strength of ABS and thus, is the sabot material of choice for severe launch conditions. The Radel has successfully been used at the NASA Marshall center, but not by the present author. It has a tensile yield strength of 10 ksi and an Izod strength of 13 ft-lbf/in, but a somewhat higher density than the other plastics in Table 6.

Many designs for sabots made of polycarbonate (Lexan, Zelux) are given in Ref. 9. Reference 10 states that "Polycarbonate plastic (Lexan) is widely used because it has a higher impact strength and a high(er) modulus of elasticity than most other plastics." Our experience with polycarbonate is that it can easily craze crack if it is not carefully double annealed. Polycarbonate is also subject to degradation due to age, ultraviolet light and some lathe cutting fluids. We are not currently using polycarbonate for sabots, although its nominal strength is greater than that of ABS or ST-801 Nylon. If one chooses to use polycarbonate for sabots (or models) it would be prudent to use new material that has been double annealed.

The mass of the sabot is sometimes called "parasite mass" because the goal is to launch the model, but, in most cases, a sabot is necessary. The sabot can make a substantial contribution to the total launch package mass. To enable higher velocities to be obtained or to reduce the stress on the gun and the launch package, a lighter sabot would be preferred. Because ABS and ST-801 Nylon have the lowest densities in Table 6, the sabot parasite mass will be less when the two former plastics are used, instead of polycarbonate or polyphenylsulfone.

12. Sabot separation

A typical launch package consists of a model encased within four (or two) interlocking sabot "fingers". Figure 22 shows a model inside a four-fingered sabot with one of the fingers off to one side. When the launch package exits the gun muzzle, the sabot fingers must be separated (move apart sideways) from the model, allowing it to fly freely. Ideally, the model then passes through a center aperture in a steel cone (the "sabot stripper"), while the sabot fingers impact the outer surface of the cone and are stopped. Figure 23 shows the arrangement of the gun, dump tank, sabot stripper and shadowgraph test section for the NASA Ames HFFAF facility. (The use of the "slap" paper will be discussed in Sec. 14.) The sabot fingers can be driven apart sideways by several techniques. One technique consists of shaping the front of the sabot fingers to form a conical (typically at a half angle of ~45 degrees) ramp-like surfaces. The aerodynamic ram pressure then will open up the sabot fingers from the front. This is called aerodynamic sabot separation and can be seen in the sabot design shown in Fig. 22. As a rough rule for the Ames HFFAF ballistic range, a minimum pressure of 30 – 50 Torr of air is required for adequate aerodynamic sabot separation. If a cylindrical hole is cut in the rear part of the sabot fingers, the muzzle blast of the gun can be used to open the sabot fingers from the rear. This is called muzzle blast sabot separation. At times, both separation techniques can be used together. Figure 24 shows a launch package using both types of sabot separation techniques. Figure 25 shows several progressive frames from a sabot separation video for the launch package shown in Fig. 24. Figure 26 shows frames from a sabot separation video for a launch package identical to that shown in Fig. 24 except without the muzzle blast cavity. It is evident that with the muzzle blast cavity, the sabot finger separation angles (from the rear) are much larger than those without the cavity.

When launching into very low (e.g., < 30 - 50 Torr) test section pressures, as is typically done for calibration spheres, the aerodynamic separation technique is not effective. Hence, muzzle blast separation is the technique of choice. (In some cases, while the initial launch is into a vacuum, farther down range the model passes through a diaphragm into the pressurized region of the range, where the aerodynamic studies take place.) Figure 27 shows a launch package designed for launching a very light model into a vacuum using muzzle blast sabot separation. Although the forward ends of the sabot fingers are cut into a 45 degree cone shape, there are

no aerodynamic separation forces since the launch is into vacuum. In addition, aerodynamic separation could not be used in this case, because the aerodynamic forces would tend to drive the very light model back into contact with the sabot fingers, resulting in unacceptable wild motions of the model.

In some cases, it is advantageous to place an obturator (gas seal) cup behind the sabot fingers to block the passage of drive gas up through the joints between the serrated sabot fingers. This prevents the drive gas from heating the model for aerothermal tests. However, this prevents the use of muzzle blast sabot separation. The obturator cup generally follows the model down the range, but drops behind sufficiently so as not to affect the flight of the model. Figure 28 shows a launch package with an obturator cup (beneath the sabot fingers) designed for aerodynamic separation of the sabot fingers. Discussion of obturator cup design and tests is presented in Ref. 11.

In some ranges, (e.g., the Ames Vertical Gun Range - AVGR), the sabot fingers are separated by centrifugal forces, using a rifled gun barrel. This will not work for the Ames HFFAF and GDF ranges, since the guns used in these ranges are not rifled and since rapidly spinning models are not suitable for vehicle aerodynamic studies, wherein the flight vehicles are not spinning.

Reference 12 has a good discussion of sabot separation techniques and mechanical sabot separation techniques in particular. One mechanical sabot separation technique is to have a reduced (less than the barrel diameter) diameter hole plate at the muzzle to intercept the outer edge of the sabot and slow it down or stop it. In one version, the hole plate successively stepped down to 82% of the barrel diameter and stopped the plastic sabot. This was used up to launch velocities of ~200 m/sec. (Note that this technique does not appear in Ref. 12.) A second version, which does appear in Ref. 12 (with details in Ref. 13) has a hole plate of 90% of the barrel diameter which intercepts the outer part of a foam sabot enough to slow it down to drop behind the model. This was used with launches at velocities up to 800 m/sec. Reference 12 also discusses contracting vented barrels and deflecting barrels and ramps.

13. Stress calculations

13.1. Launch stresses

As a first step, one needs to calculate the muzzle velocity of the gun. From the maximum desired mid-range model velocity, using the CFD-estimated drag coefficient, one can back calculate to the maximum muzzle velocity required for a given model in a given test campaign. Then, given the length of the gun barrel, the average acceleration needed to achieve this muzzle velocity is calculated. The maximum acceleration in the gun is typically about 2.5 times the average acceleration for powder gun launches, but can be as much as 3 to 6 times the average acceleration for two-stage light gas gun launches. In some cases, for powder gun launches at NASA Ames, powder chamber pressure histories for a substantial number of different shot conditions are available. These data, with some scaling, can be used to estimate the maximum model base pressure and hence, the maximum acceleration for the shot in question. For two-stage light gas gun launches, it may be possible to run a CFD simulation of the shot in question to get a value for the maximum launch package acceleration in the barrel. With the maximum launch package acceleration in hand, one can proceed to the calculation of the model and sabot stresses.

We first consider a conventional (compact) model in a sabot. Figure 29 shows the NASA Ames Mars Science Laboratory (MSL) model in the sabot[8]. The arrows in Fig. 30 show the high bearing stresses under the model, the lower (near hydrostatic) pressures in the sabot away from the model base and the drive gas pressures on the base of the sabot. These combined stresses will lead to shear stresses (see Fig. 31) tending to allow the model to “fall” through the sabot due to the very large launch accelerations. The difference between the bearing stresses

beneath the model and the near hydrostatic pressures outside the model base should be compared with the compressive strengths of the model and sabot materials. The shear stresses shown in Fig. 31 should be compared with the shear strength of the sabot material, which can be estimated as about 60% of the tensile strength if actual shear strength data is not available. The stress analyses can be performed in the older manner as described above, or a finite element model can be constructed (e.g., in SolidWorks) and the von Mises stresses found. The maximum von Mises stresses can then be compared with the uniaxial yield stresses of the relevant model and sabot materials.

Figure 32 shows a ballistic range model of a vehicle with a compact centerbody and a relatively thin aerobrake (a solid, fixed structure designed to simulate an inflatable or deployable) in its launch sabot. This model simulates a flight vehicle similar to the HEART vehicle discussed in Sec. 6 and shown in Fig. 13. With this type of model, attention must be paid to additional failure modes that are unimportant with the typical compact model. Considering the centerbody as an isolated unit, the bearing stress under the centerbody and the sabot shear stress needed to prevent the centerbody from falling through the bottom of the sabot need to be examined. If it is concluded that the isolated centerbody cannot be supported by the sabot base, then the centerbody plus aerobrake considered as a single unit should be considered. The bearing stress for the unit as a whole can then be examined; this stress will be much lower and hence, more favorable than the bearing stress for the isolated centerbody. The sabot plastic shear stresses necessary to prevent the centerbody/aerobrake from falling through the sabot plastic should then be examined. Since, in this case, the aerobrake and the centerbody must act as a unit, the shear stress at the joint between to two components will be fairly high – it must be examined and determined to be within the capabilities of the material under consideration. If the model is comprised of, say, a magnesium aerobrake and a steel centerbody, the steel will tend to fall out of the magnesium and the shear stresses on the threads between the two materials must be examined and determined to be at an acceptable level for the weaker of the two materials. A finite element analysis of the model-sabot combination can be performed as described in the preceding discussion and the following stresses should be examined.

Bearing stresses under the centerbody and the aerobrake.
Shear stresses in the sabot material under the outer edge of the centerbody.
Shear stresses at the joint between the centerbody and the aerobrake, particularly thread shear stresses if the two parts are made of different materials and threaded together.

We note that the model-sabot combination of Fig. 32 is a concept and has not actually been launched to date. However, an ADEPT model with a compact centerbody and a relatively thin aerobrake has been successfully launched using the model-sabot combination shown in Fig. 33.

The previous calculations are made as if the model were in a steady-state environment maintained at the maximum launch package acceleration. However, these extreme conditions are short-lived and there is considerable evidence that shows, at higher muzzle velocities (i.e., 4 km/sec and above), at least for compact models (e.g., spheres), the launch packages can tolerate stresses that are nominally well above the static material yield stresses for the short duration of the launches. Sufficient time may not elapse during the launches for the models to fall through the sabots. For the launches described in Figs. 3.36, 3.39, 3.41, 3.42 and 3.43 of Ref. 14, and in particular for the relatively large sphere launches of Figs. 3.42 and 3.43, bearing and shear stresses calculated as described in the earlier paragraph regarding compact models are 2 to 5 times the nominal static yield stresses and yet, satisfactory launches were presumably obtained. The model-sabot configurations for these launch packages are shown in Figs. 34 – 36. Note that there is some uncertainty regarding the sphere diameter shown in Fig. 3.43 of Ref. 14. No reference is given in Ref. 14 for this launch package and the stresses calculated for the larger sphere [Fig. 36 (b)] are extremely large. It might be better to key future

designs off the launch package with the smaller sphere [Fig. 36 (a)], where the stresses are more comparable to stresses for other successful designs. These launches were at velocities of 7.3 – 9.4 km/sec. The calculated stresses for the higher velocity launches (up to 5.7 km/sec) of the model shown in Figs. 29 – 31 also greatly exceed the nominal static yield stresses. Such a favorable situation may well not be the case for lower velocity launches which last for considerably longer periods of time (as scaled by the launch tube diameter). Failed launches, where the model has fallen through the sabot rear, have been seen in X-ray photographs (e.g. see Fig. 37). For compact models at high velocities, it would seem desirable to key off earlier, successful sabot designs, even though the calculated stresses are above the static yield stresses of the materials. The best philosophy may be to design the sabots so that the calculated stresses are no greater (relative to the material yield stresses) than those calculated for successful sabot designs, even though both sets of stresses exceed the material static yield stresses.

If stresses, calculated as described above, are found to be pushing or exceeding the limits (either the static yield stress limits for lower velocities or the limits of successful designs for higher velocities) and cannot be avoided by sabot and model design changes, then the launch package should be regarded as experimental. As such, a definite failure risk must be acknowledged, and it would be desirable to have muzzle view and separation videos and/or muzzle X-ray pictures to verify the quality of the launch. (It should be noted that for ANY new model/sabot design, it is desirable to have muzzle and sabot separation videos.) It must be realized that a complete failure of the sabot (i.e., model fall-through) within the launch tube could result in the model scraping along the gun barrel and ruining it, requiring a time-consuming and expensive barrel replacement.

13.2. Aerodynamic stresses

For models with a centerbody and a relatively thin aerobrake (see Fig. 38) in free flight, the aerodynamic forces will produce substantial bending and shear stresses near the joint between the centerbody and the aerobrake. These stresses must be calculated at the most severe muzzle velocity/range gas density condition for the model in question. If the model is made of two pieces and threaded together [(Fig. 38(b)] the joint will be able to withstand much lower stresses than for the case of a single piece model. If the stresses are too high, stronger materials or a greater aerobrake thickness near the aerobrake-centerbody joint may be necessary. If heavy gas jets are used to “slap” the model to induce pitch oscillations (discussed in Sec. 14), the aerodynamic forces must be evaluated for the heavy gas condition.

13.3. Slap stresses

In some cases, varying amplitude pitch oscillations are produced by “slapping” the model by having it impact a sheet of paper or cardstock which covers one-half of the frontal area of the model. (This procedure is discussed further in Sec. 14 and Ref. 5.) For bodies with thin aerobrakes or a thin front shell (e.g., see Fig. 39), one must also evaluate the stresses produced by the “slap” process. From conservation of momentum, assuming an inelastic collision and that the mass loading (g/cm^2) of the slap media is much less than that of the aerobrake, the velocity of the thin aerobrake or front shell relative to the rest of the model after the slap impact, u_a, will be given by

$$u_a = \frac{um_p}{\rho_a t_a} \qquad \text{Eq. (33)}$$

where

u = velocity of model, cm/s
m_p = mass loading of slap paper, g/cm^2
ρ_a = density of thin shell, g/cm^3
t_a = thickness of thin shell, cm

The kinetic energy per unit mass of the moving thin shell relative to the main mass of the model, K_a, is

$$K_a = \frac{1}{2}u_a^2 \tag{34}$$

To calculate the exact shape that the thin shell will assume at maximum deflection after the impact is a very complex problem. We can get a rough estimate of the amount of bending energy in the shell by evaluating this energy for a deflection curve based on uniform pressure loading. We assume that this analysis gives us a curve of $M_b = M_b(r)$, where M_b is the bending moment per unit length and r is the radius out from the central axis. For the model shown in Fig. 39(a) one might use a clamped boundary condition at the edge of the thin shell. For the model shown in Fig. 39(b), the boundary condition might approach simply supported to some degree since the thickening ring around the edge of the thin shell could tilt and pull away from the material of the afterbody. The shear energy per unit mass is much less than the bending energy per unit mass if the thickness of the shell is much less than the radial extent of the shell, varying as [(thickness)/(radius)]^2. The maximum tensile or compressive stress at the shell surface, σ_b, is

$$\sigma_b = \frac{M_b y}{I_b} \tag{35}$$

where y is the distance of the shell surface from the shell neutral axis, equal to $t_a/2$ and I_b is the moment of inertia per unit length of the shell cross section, equal to $t_a^3/12$. Hence,

$$\sigma_b = \frac{6M_b}{t_a^2} \tag{36}$$

The strain energy per unit volume at the shell surface, E_s, is given by

$$E_s = \frac{1}{2}\sigma_b\varepsilon_b = \frac{\sigma_b^2}{2E} \tag{37}$$

where ε_b is the strain and E is Young's modulus of elasticity. The average strain energy over the shell is one third the peak value at the shell surface. Hence,

$$\bar{E}_s = \frac{\sigma_b^2}{6E} \tag{38}$$

Substituting for σ_b, we get

$$\bar{E}_s = \frac{6M_b^2}{t_a^4 E} \tag{39}$$

Dividing by the shell density, ρ_a, gives the energy per unit mass

$$\bar{\bar{E}}_{sm} = \frac{6M_b^2}{t_a^4 E \rho_a} \tag{40}$$

We then average over the thin shell to get

$$\bar{\bar{E}}_{sm} = \frac{6\left[M_b^2\right]_{av}}{t_a^4 E \rho_a} \tag{41}$$

We then evaluate $\bar{\bar{E}}_{sm}$ at $Max(\sigma_b) = Max(M_b)\frac{6}{t_a^2} = \sigma_{yield}$, call this value $\bar{\bar{E}}_{sm,\max}$ and compare it with K_a. If $K_a \geq \bar{\bar{E}}_{sm,\max}$, yielding is possible or likely. If K_a << $\bar{\bar{E}}_{sm,\max}$, one should be safe. From $K_a = \bar{\bar{E}}_{sm,\max}$, a safety factor of perhaps 3 may apply, but this is a matter of professional judgment.

For a given slap impulse density, um_p, the relation of K_a with $\bar{\bar{E}}_{sm,\max}$ improves linearly with decreasing E and increasing ρ_a and improves quadratically with increasing t_a and σ_{yield}. If, after adjusting these parameters, K_a is still too high compared with $\bar{\bar{E}}_{sm,\max}$, other options are available to "slap" the model. One may use a succession of thinner slap papers or jets of heavy or light gases to "slap" the model. For a compact model with a thin shell, one could cut a hole in the slap paper so that the paper impacts the model only outside the thin shell area. For compact models, one can avoid the thin front shell by using different model materials. Metals of choice are tungsten alloy, brass, steel, titanium, aluminum and magnesium. Densities of these metals are given in Table 5 of Section 10. Such a model design is shown in Fig. 40. For compact models without a thin front shell, the aerodynamic and paper slap stresses are unimportant and do not need to be analyzed for model design.

14. Tilted launches and "slapping" of model to produce pitch/yaw oscillations

To characterize the aerodynamics of a model fully, a number of shots must be made, with the model having a wide range of amplitudes of pitch oscillations. Typically, the peak amplitudes (i.e., one-half of the peak-to-peak value) required range from 2 to 40 degrees. These can be achieved by launching the models in different sabots with different in-sabot tilts. (See, for example, Fig. 41.) This requires a number (3 or 4) of different sabot designs. At the larger sabot tilts, poor launches can be obtained, because, with the asymmetric sabot structure and asymmetric sabot separation, the sabot fingers can re-contact the model after separation, causing large, unwanted variations in the pitch and yaw oscillation amplitudes.

A second way to achieve a range of pitch (or yaw) oscillation amplitudes is to use a single sabot design (that orients the model at zero pitch and yaw angles) and "slap" the model with a piece of paper or cardstock after the model passes through the sabot stripper. In the NASA Ames HFFAF ballistic range, the location of the paper or cardstock is shown in Fig. 23. The paper/cardstock is arranged to impact one-half of the model to provide the maximum kick for a given paper mass loading (g/cm^2). (We use "slap" to describe the action of the paper or cardstock impacting the model and "kick" to describe the amount of angular velocity imparted to the model by the "slap".) Figure 42 shows 4 frames from a high speed video showing a LDSD model penetrating the slap paper.

The paper mass loading (m) to produce a required rms pitch oscillation amplitude can be calculated as follows. The linear impulse, I_L, to the model on impacting the paper is given by

$$I_L = \frac{\pi}{8} D^2 mu \tag{42}$$

We assume that the impact is a flat, normal impact – no attempt is made to refine the analysis by allowing for the paper sliding off the inclined front surface of the model, while maintaining a fraction of its initial forward velocity (relative to the model). Since the distance of the center of gravity of the semicircle from the axis is $2D/(3\pi)$, the angular impulse, I_A, to the model on impact is

$$I_A = \frac{1}{12} D^3 mu \tag{43}$$

The initial angular velocity of the model after impact, $\dot{\theta}_{\max}$, is given by

$$\dot{\theta}_{\max} = \frac{1}{12} \frac{D^3 mu}{I} \tag{44}$$

The angular motion of the model subsequent to impact is given by

$$\theta = \theta_{\max} \sin\left(\frac{2\pi t}{P}\right) \tag{45}$$

where

θ = instantaneous pitch angle
θ_{max} = maximum pitch angle
t = time
P = period of pitch oscillations

Differentiating Eq. (45), we get

$$\dot{\theta} = \theta_{\max} \frac{2\pi}{P} \cos\left(\frac{2\pi t}{P}\right) \tag{46}$$

Evaluating Eq. (46) at t = 0, we get

$$\dot{\theta}_{\max} = \theta_{\max} \left(\frac{2\pi}{P}\right) \tag{47}$$

Figure 43 shows the rms pitch oscillation angles versus slap paper (or cardstock) mass loading for LDSD models with the inflatable stowed (Fig. 11) and deployed (Fig. 6). Two sets of data points are shown for the LDSD model with the inflatable deployed, red dots for shots with a single slap sheet and blue dots for multiple slap sheets. The purple dots are the data points for the LSDS model with the inflatable stowed. It is seen that the theoretical lines agree roughly

with the trend liens of the experimental data. For the data with the inflatable deployed, the agreement is quite good. For the data with the inflatable stowed, the theoretical line lies up to 30% above the trend line for the experimental data for the largest angles, but the agreement is much better at the smaller angles.

It has been observed at NASA Ames that stacking sheets of paper or cardstock one immediately behind the next can lead to wide variations in the oscillation amplitudes obtained, while very consistent results are obtained if single sheets of paper or cardstock of varying thicknesses are used. It is believed that these variations are caused by the ejecta from the first sheets blowing away part of the succeeding sheets before they can produce their full impact momentum. This effect is believed to be very sensitive to the exact arrangement and spacing of the sheets. The effect can be seen in Fig. 43, where four of the blue data points, with multiple slap sheets, are significantly below the trend line, while the red data points, with single slap sheets, group much more tightly around the trend line. All of the purple data points, with single slap sheets, group about as well as the red data points. At Ames, the paper/cardstock sheets are stacked together without separation. On the other hand, at the Eglin ARF range, multiple sheets of paper or film with spacings of several centimeters have been successfully used.

Figure 44 shows data corresponding to the data of Fig. 43 for a proprietary model launched in the NASA Ames HFFAF facility. Figure 44 shows the difference in the performance of the slap paper for the supersonic (M = 1.3 – 1.7) and subsonic (M = 0.6) cases. This is likely due, at least in part, to the difference in C_{m_α} between the supersonic and subsonic cases. It also shows that, for the supersonic cases, when the cutout in the slap paper is used, about 2.2 times the paper mass loading is required to achieve the same rms pitch oscillation amplitudes. The semi-circular cutout was 1” in diameter and the model diameter was 1.5”. The cutout was used because the center of the front of the model was a very thin shell and there was concern that the slap paper impact could permanently deform the shell.

For models with relatively thin, fragile aerobrakes surrounding a compact aeroshell, estimates of the stresses produced by the impact of typical slap paper often greatly exceed the strengths of the aerobrake materials. One possibility to avoid this problem is to “slap” the model by passing it through, say, 30 very light (~0.0006 cm thick) Mylar diaphragms spaced, say, 1 cm apart to avoid the ejecta issue discussed above. A second possibility, which provides an even smoother “slap” would be to pass the model through a gas jet which is heavier or lighter than the surrounding air. The heavier jets (e.g. Ar, CO_2) would increase the aerodynamic stress on the aerobrake, but a lighter (e.g., He) jet would not increase the aerodynamic stresses, but would provide a “negative” slap since the aerodynamic forces are unbalanced in the opposite direction. Air on the side of the model opposite the helium would be doing the “slapping”. It is clear that for both these options, the slapping medium, Mylar sheets or a gas jet, must be arranged to cover one half of the model as it flies through the medium.

Appendix A

In this appendix, we present the key parameters for the flight trajectory and the ballistic range simulation of the LDSD model with the inflatable deployed discussed in Sec. 5 of the main text. The list below gives key parameters for the flight vehicle and the normalized radius of gyration and the density for the preliminary range model.

D, flight vehicle diameter = 6 m
m, flight vehicle mass = 1369.9 kg
I_{min}, flight vehicle minimum moment of inertia = 1513.8 kg-m^2
I_{max}, flight vehicle maximum moment of inertia = 2077.4 kg-m^2
I in the analyses herein is taken to be I_{max}
V, flight vehicle volume = 23.017 m^3
ρ_s, flight vehicle mean density = m/V = 59.52 kg/m^3

A, flight vehicle frontal area = $\frac{\pi}{4}D^2$ = 28.27 m^2

x_{cg}/D, normalized axial location of center of gravity, distance aft of vehicle nose = 0.1583

r_g, flight vehicle radius of gyration = $\sqrt{\frac{I}{m}}$ = 1.231 m

$\frac{r_g^2}{D^2}$ for flight vehicle = 0.04212

$\frac{r_g^2}{D^2}$ for preliminary range model = 0.05993

ρ_s for preliminary range model = 7800 kg/m^3

Table A1 below gives the trajectory data, the CFD aerodynamics data for the flight vehicle, the density ratios ρ/ρ_s for the flight vehicle and the preliminary model design, the normalized pitch oscillation wavelength (λ/D) and the K parameter [see Eq. (4) of Sec. 5] for the flight vehicle and the preliminary model design.

Table A1. Trajectory, aerodynamic and other key data for the LDSD vehicle with the inflatable deployed and the corresponding range model.

Variable	Units	Trajectory point 1	Trajectory point 2	Trajectory point 3	Trajectory point 4	Trajectory point 5
M		3.957	3.50	3.00	2.479	2.365
u	m/s	1295	1144	982	811	774
ρ	kg/m^3	1.107 x 10^{-3}	1.058 x 10^{-3}	1.088 x 10^{-3}	1.379 x 10^{-3}	1.524 x 10^{-3}
T	K	266.68	266.04	266.45	266.56	266.29
μ	kg/m/s	1.678 x 10^{-5}	1.675 x 10^{-5}	1.677 x 10^{-5}	1.678 x 10^{-5}	1.676 x 10^{-5}
c	m/s	327.3	326.9	327.2	327.3	327.1
Re		5.126 x 10^5	4.337 x 10^5	3.821 x 10^5	4.001 x 10^5	4.220 x 10^5
C_{m_α}		0.1935	0.185	0.175	0.164	0.161
C_D		1.454	1.468	1.492	1.530	1.544
C_{L_α}		1.127	1.155	1.192	1.249	1.268
ρ_s/ρ (flight)		53,760	56,250	54,700	43,160	39,050
λ/D		353.8	370.1	375.3	344.3	330.8
n*		1.814	1.735	1.710	1.865	1.941
K (flight)		1.525	1.560	1.604	1.657	1.673
ρ_s/ρ (pre. model)		37,730	39,480	38,390	30,290	27,410
K (pre. model)		1.820	1.862	1.914	1.977	1.997

*n is the number of pitch oscillation cycles in the range with a model diameter of 3.56 cm and a range length of 22.86 m

"pre. model" denotes preliminary model

We note that the number of cycles in the range shown in Table A1 is somewhat less than the goal of 2.0 cycles. To alleviate this problem, the pressure in the range was raised somewhat above that implied by the ρ_s/ρ (preliminary model) values. This brings the number of cycles back towards the goal of 2.0, while accepting some mismatch (up to 20 - 30%) of the Re and λ/D values. In the actual test, the number of cycles in the range varied from 1.84 to 2.4. Only 7 of 37 shots had less than two cycles in the range and only 1 shot had less than 1.9 cycles in the range.

Appendix B

In this appendix, for the LDSD vehicle with the inflatable deployed and the range simulation of same, we give the key parameters necessary for the calculation of the velocity and Mach number drops $\left.\frac{du}{u}\right|_{\lambda}$ and dM_{range} and the velocity Δx (see Sec. 7). The list below gives some pertinent parameters for the flight vehicle and the preliminary range model.

$\frac{r_g^2}{D^2}$ for flight vehicle = 0.04212

$\frac{r_g^2}{D^2}$ for preliminary range model = 0.05993

L, range length = 22.86 m

D for preliminary range model = 3.56 cm

Table B1 below gives the data for the calculations for the five data points along the trajectory of the LDSD vehicle with the inflatable deployed and simulation of same.

Table B1. Data for calculation of velocity and Mach number drops and slow down Δx_{range} for LDSD vehicle with the inflatable deployed and simulation in the range.

Variable	Units	Trajectory point 1	Trajectory point 2	Trajectory point 3	Trajectory point 4	Trajectory point 5
M (average)		3.957	3.50	3.00	2.479	2.365
C_{m_α}		0.1935	0.185	0.175	0.164	0.161
C_D		1.454	1.468	1.492	1.530	1.544
λ/D		353.8	370.1	375.3	344.3	330.8
$\left.\frac{du}{u}\right\|_{\lambda,flight}$		0.0353	0.0357	0.0378	0.0451	0.0482
$\left.\frac{du}{u}\right\|_{\lambda,range}$		0.0444	0.0448	0.0475	0.0566	0.0606
dM_{range}		0.319	0.272	0.244	0.262	0.278
Δx_{range}	cm	92.1	88.9	92.9	120.8	134.5

Appendix C

In this appendix, for the LDSD vehicle with the inflatable deployed and the range simulation of same, we give the key parameters necessary for the calculation of the maximum swerve in the range due to the oscillating lift due to pitch oscillations, y_{max} [see eq. (26) of Sec. 8]. The list below gives some pertinent parameters.

$\frac{r_g^2}{D^2}$ for preliminary range model = 0.05993

D for preliminary range model = 3.56 cm
α_{max}, maximum pitch angle = 10 degrees

Table C1 below gives the data for the calculations for the five data points along the trajectory of the LDSD vehicle with the inflatable deployed and simulation of same.

Table C1. Data for calculation of maximum swerve due to oscillating lift vector for LDSD range model with the inflatable deployed.

Variable	Units	Trajectory point 1	Trajectory point 2	Trajectory point 3	Trajectory point 4	Trajectory point 5
M		3.957	3.50	3.00	2.479	2.365
C_{m_α}		0.1935	0.185	0.175	0.164	0.161
C_{L_α}		1.127	1.155	1.192	1.249	1.268
y_{max}	cm	0.253	0.245	0.219	0.201	0.187

Appendix D

In this appendix, for the LDSD vehicle with the inflatable deployed and the range simulation of same, we give the key parameters necessary for the calculation of the maximum swerve in the range due to steady-state lift, y [see Eq. (32) of Sec. 9]. Note that the actual model has zero mean lift and hence the actual y values are all zero. A lift coefficient of 0.23 was assumed in this appendix to illustrate the calculation technique. The list below gives some pertinent parameters.

$\frac{r_g^2}{D^2}$ for preliminary range model = 0.05993
D for preliminary range model = 3.56 cm
L, full length of range from gun muzzle to last shadowgraph station = 32.92 m.

Table D1 below gives the data for the calculations for the five data points along the trajectory of the LDSD vehicle with the inflatable deployed and simulation of same.

Table D1. Data for calculation of swerve due to (assumed) steady-state lift vector for LDSD range model with the inflatable deployed.

Variable	Units	Trajectory point 1	Trajectory point 2	Trajectory point 3	Trajectory point 4	Trajectory point 5
M		3.957	3.50	3.00	2.479	2.365
C_{m_α}		0.1935	0.185	0.175	0.164	0.161
C_L		0.23	0.23	0.23	0.23	0.23
y	cm	34.2	32.7	33.6	42.6	47.0

Since the estimated maximum lift height while still within the viewing area of the shadowgraph stations is 47 cm (see Sec. 9, main text), at the lowest Mach number point, we would be just about at the limit with C_L = 0.23. For the higher Mach number points, somewhat higher C_L values, up to ~0.31 would be acceptable.

References

1. Canning, T. M., Seiff, A. and James, C. S., “Ballistic Range Technology,” AGARDograph No. 138, NATO Advisory Group for Aerospace Research and Development, August, 1970, p. 295.
2. Brock, J. M., Stern, E. C. and Wilder, M. C., “CFD Simulations of the Supersonic Inflatable Aerodynamic Decelerator (SIAD) Ballistic Range Tests,” AIAA paper 2017-1437, 55th AIAA Aerospace Sciences Meeting, 9 – 17 January, 2017.
3. Canning, T. M., Seiff, A. and James, C. S., op. cit., pp. 102 – 103.
4. ibid., pp. 103 – 104.
5. Bogdanoff, D. W., Brown, J. D., Dyakonov, A. A. and Wilder, M. C., “New Developments in Diagnostic, Launch and Model Control Techniques in the NASA Ames Ballistic Ranges,” presented at the 63rd Meeting of the Aeroballistic Range Association, Brussels, Belgium, September-October, 2012.
6. Brown, J., Bogdanoff, D., Yates, L. and Chapman, G., “Transonic Aerodynamics of a Lifting Orion Crew Capsule from Ballistic Range Data,” *Journal of Spacecraft and Rockets*, Vol. 47, No. 1, January – February, 2010.
7. Bogdanoff, D. W., Brown, J. D., Wilder, M. C. and Yates, L. A., “Developments of Techniques for Capsule Tests in the Ames Gun Development Facility,” presented at the 59th Meeting of the Aeroballistic Range Association, Cape Town, South Africa, October 12 – 17, 2008.
8. Brown, J., Yates, L., Bogdanoff, D., and Chapman, G., “Free-Flight Testing in Support of the Mars Science Laboratory,” *Journal of Spacecraft and Rockets*, Vol. 43, No. 2, March-April, 2006.
9. Canning, T. M., Seiff, A. and James, C. S., “Ballistic Range Technology,” AGARDograph No. 138, NATO Advisory Group for Aerospace Research and Development, August, 1970, pp. 99 – 153.
10. ibid, p. 109.
11. Bogdanoff, D. W. and Wilder, M. C., “Sabot, Obturator and Gas-in-Launch Tube Techniques for Heat Flux Models in Ballistic Ranges,” presented at the 64th Meeting of the Aeroballistic Range Association, Destin, Florida, October 6 - 11, 2013.
12. Canning, T. M., Seiff, A. and James, C. S., op. cit., pp. 101, 102 and 115 (discussion) and pp. 125 and 153 (figures).
13. DeRose, C. E., “Ballistic Range Tests of a Drag-Ring Configuration at Mach Numbers Around 2,” NASA TN D-4291, December, 1967.
14. Canning, T. M., Seiff, A. and James, C. S., “Ballistic Range Technology,” op. cit., pp. 145 – 149.

This page intentionally left blank.

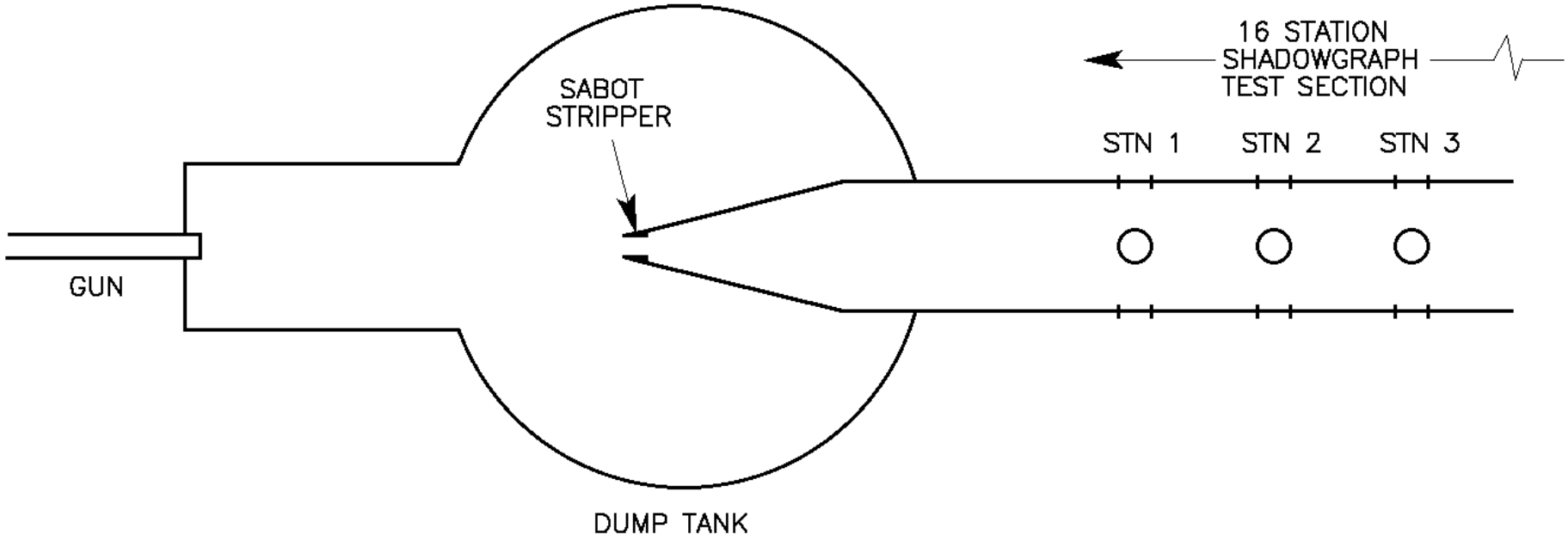

Fig . 1. Arrangement of gun, dump tank, sabot stripper and shadowgraph range for the NASA Ames HFFAF facility.

Fig. 2. Model inside 3 of 4 serrated sabot fingers. Fourth sabot finger is off to the right.

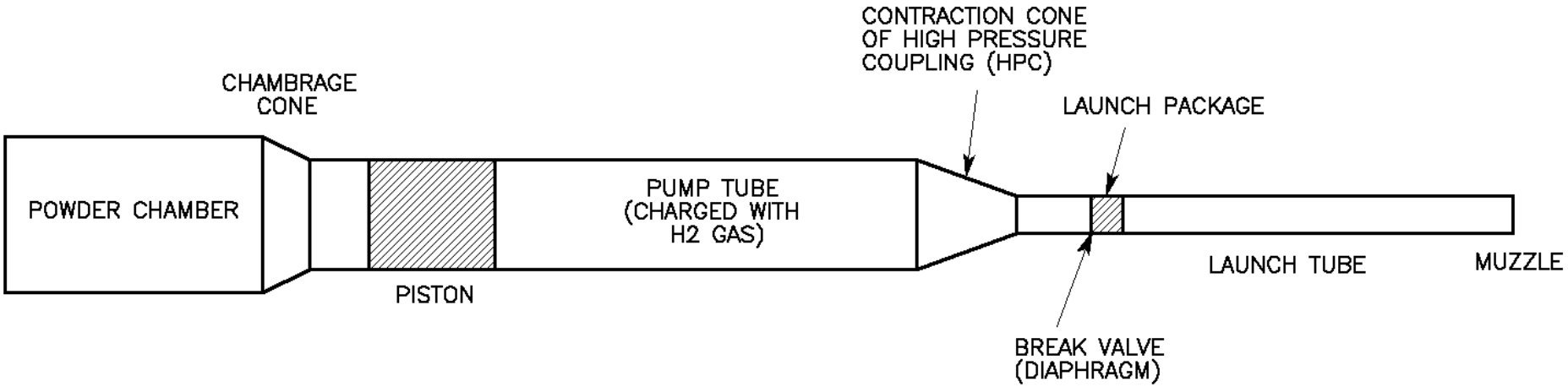

Fig. 3. Sketch (not to scale) of representative two-stage light gas gun.

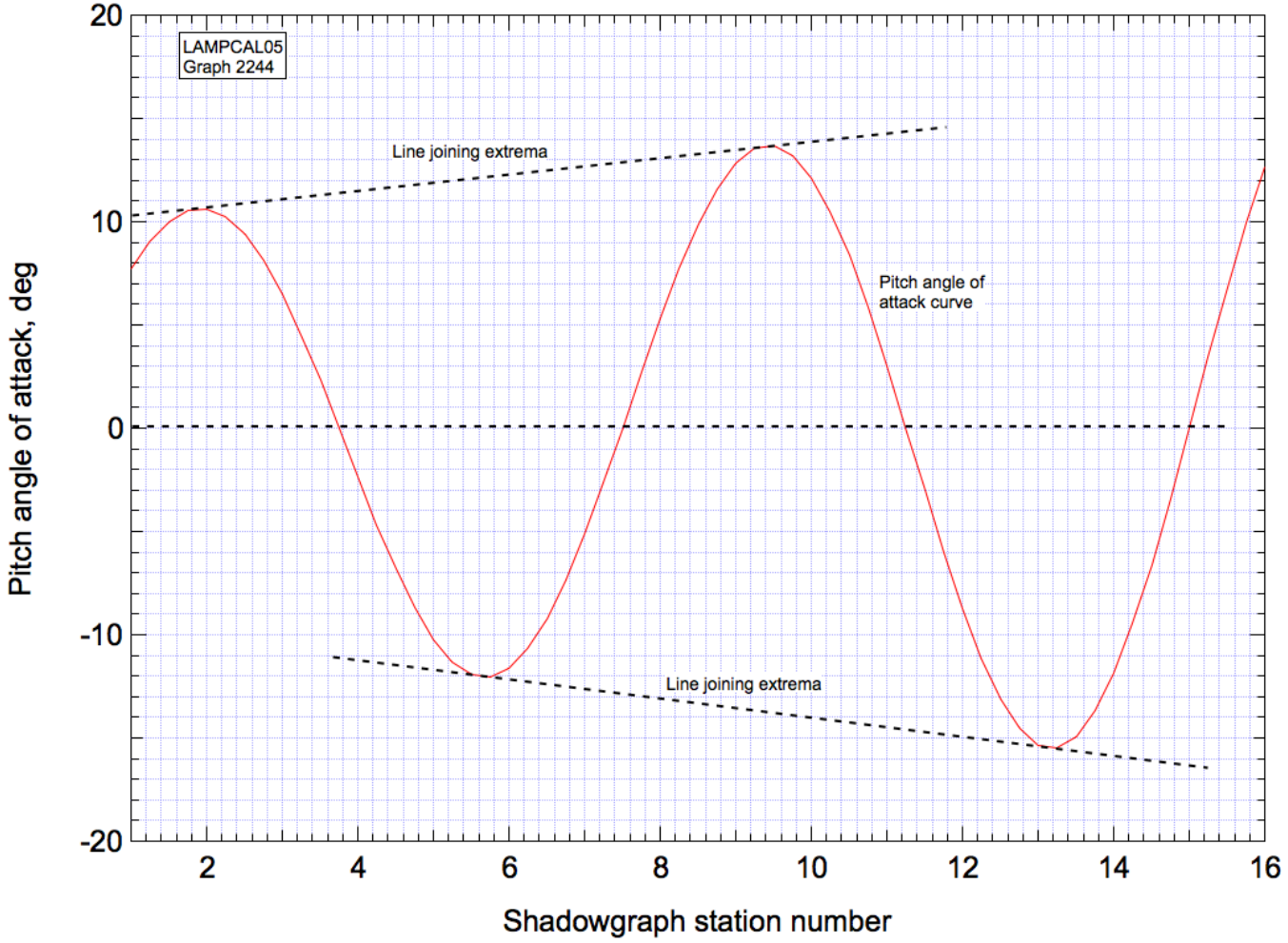

Fig. 4. Representative plot of pitch angle of attack versus shadowgraph station number. Note lines joining extrema.

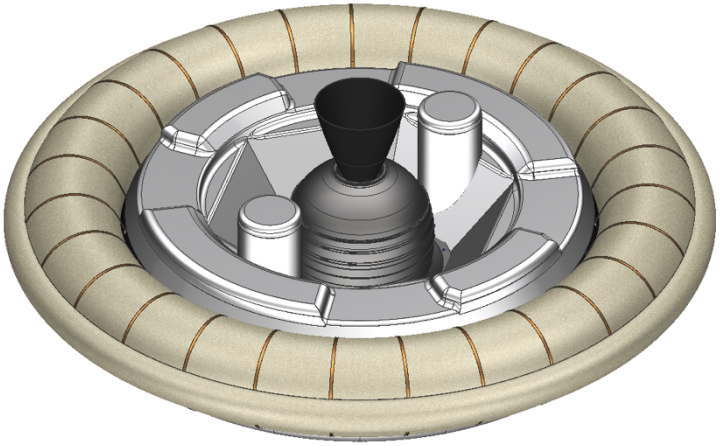

Fig. 5. LDSD vehicle with inflatable deployed.

Fig. 6. Ballistic range model of LDSD vehicle with inflatable deployed.

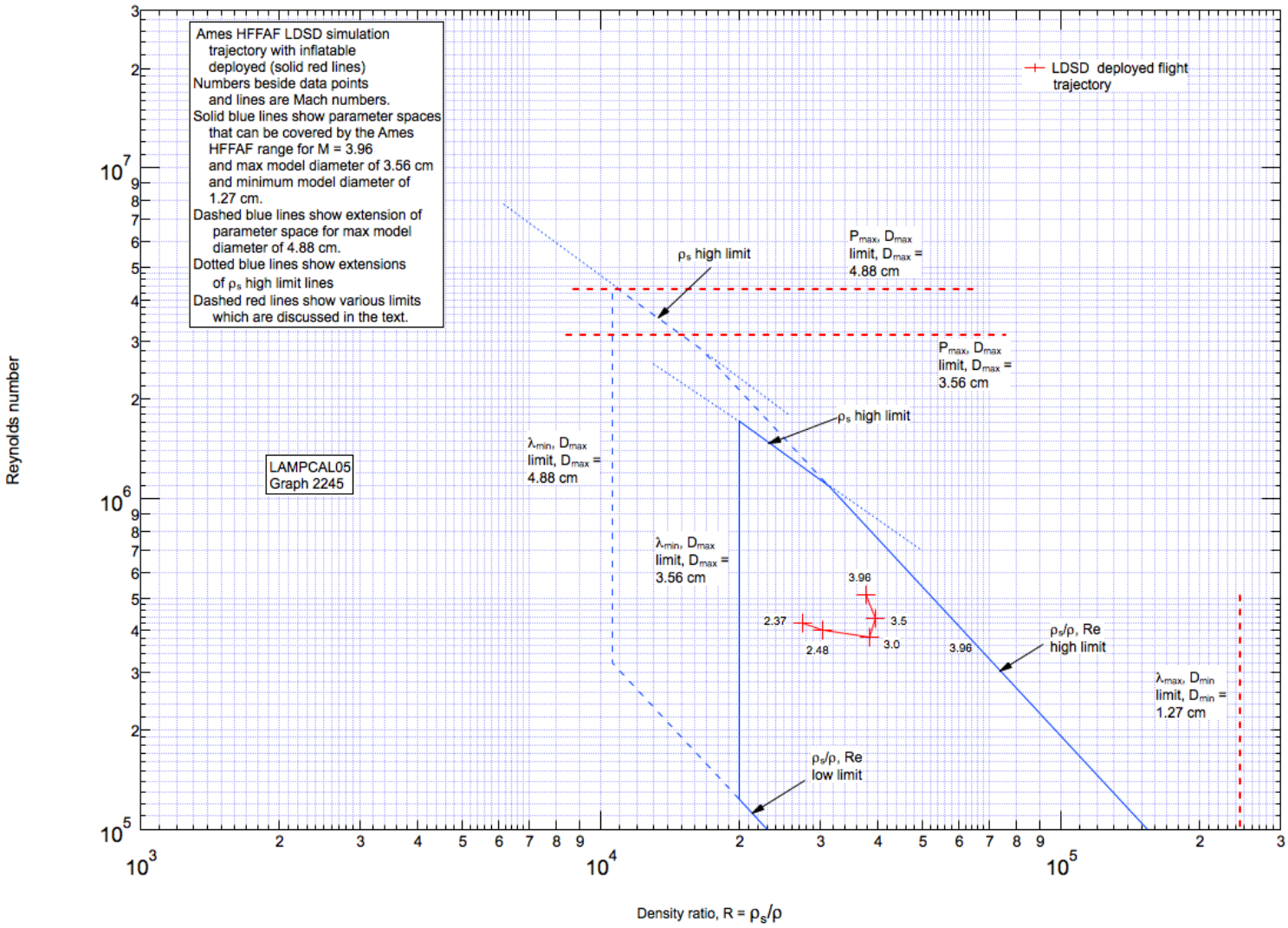

Fig. 7. Ames HFFAF LDSD simulation trajectory with inflatable deployed. Solid blue lines show facility simulation capability for Mach 3.96 and a maximum model diameter of 3.56 cm. Dashed blue lines show facility simulation capability for a maximum model diameter of 4.88 cm.

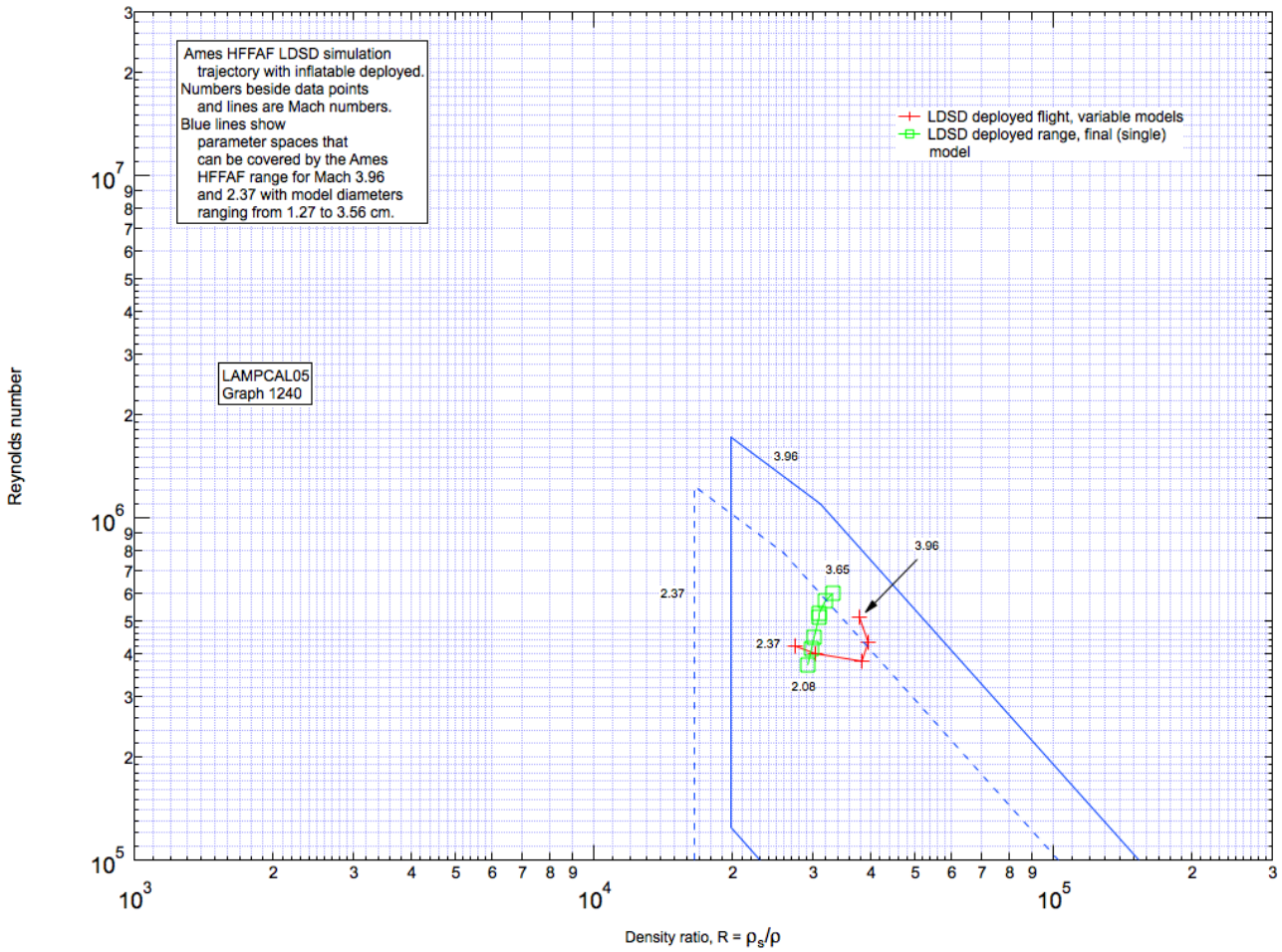

Fig. 8. Ames HFFAF LDSD simulation trajectory with inflatable deployed. Red data points show trajectory with variable models. Green data points show trajectory with a single model. Solid and dashed blue lines show facility simulation capability for Mach 3.96 and Mach 2.37 and a maximum model diameter of 3.56 cm.

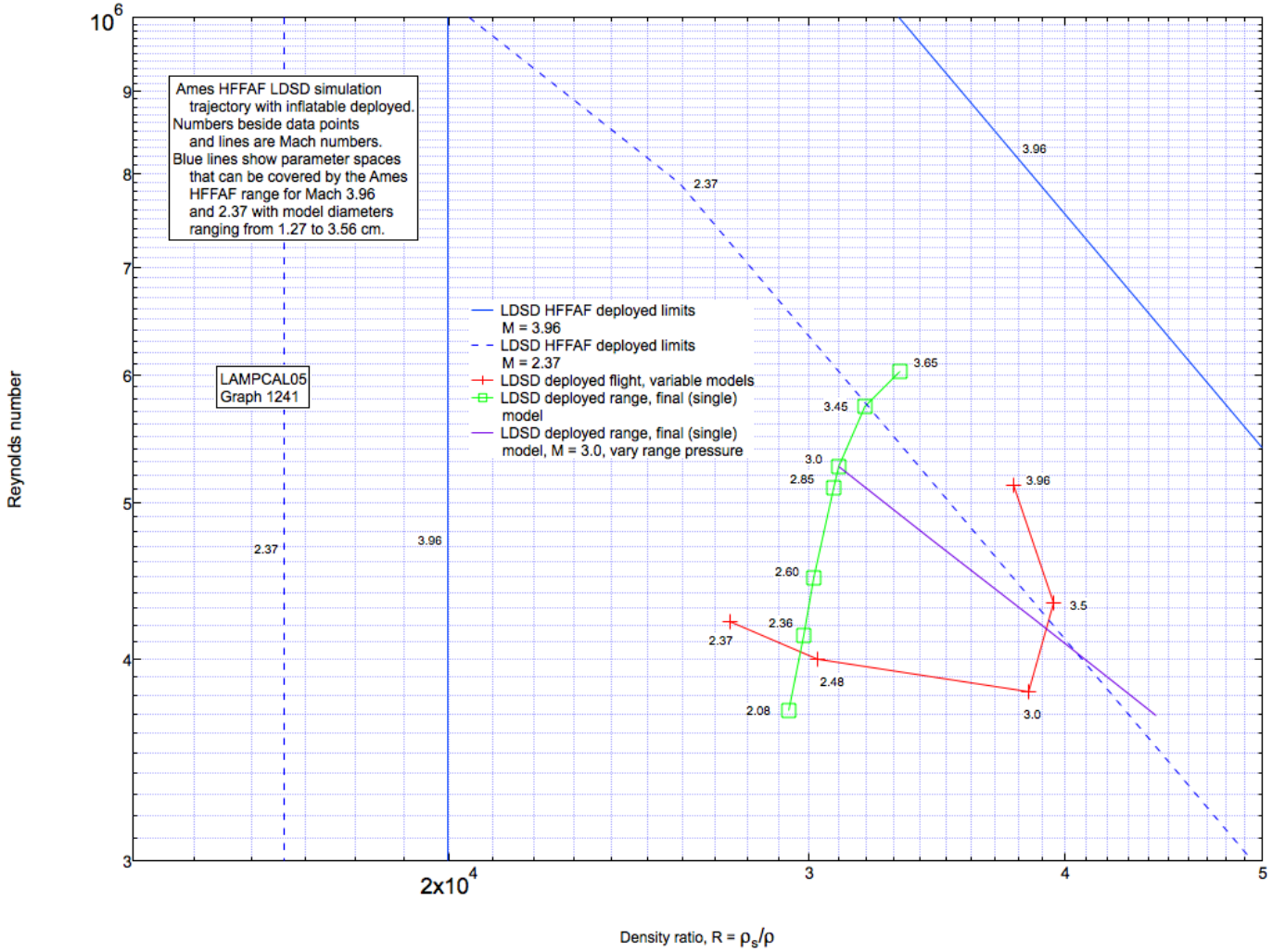

Fig. 9. Ames HFFAF LDSD simulation trajectory with inflatable deployed. Red data points show trajectory with variable models. Green data points show trajectory with a single model. Blue lines show facility simulation capability for Mach 3.96 and Mach 2.37 and a maximum model diameter of 3.56 cm. Purple line shows points at Mach 3.0 for a single model obtained by varying the range pressure.

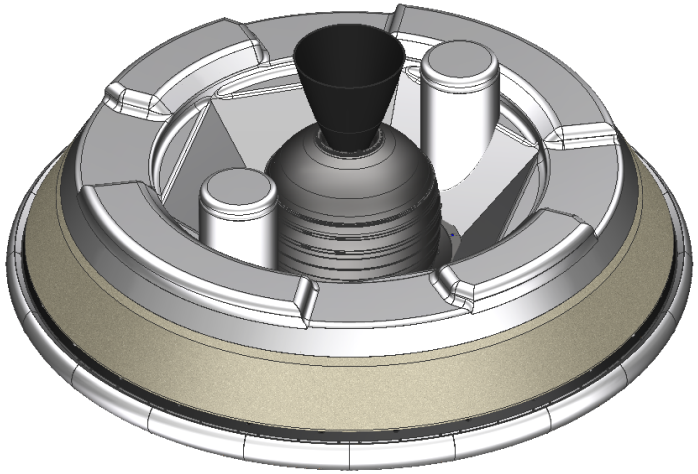

Fig. 10. LDSD vehicle with inflatable stowed.

Fig. 11. Ballistic range model of LDSD vehicle with inflatable stowed.

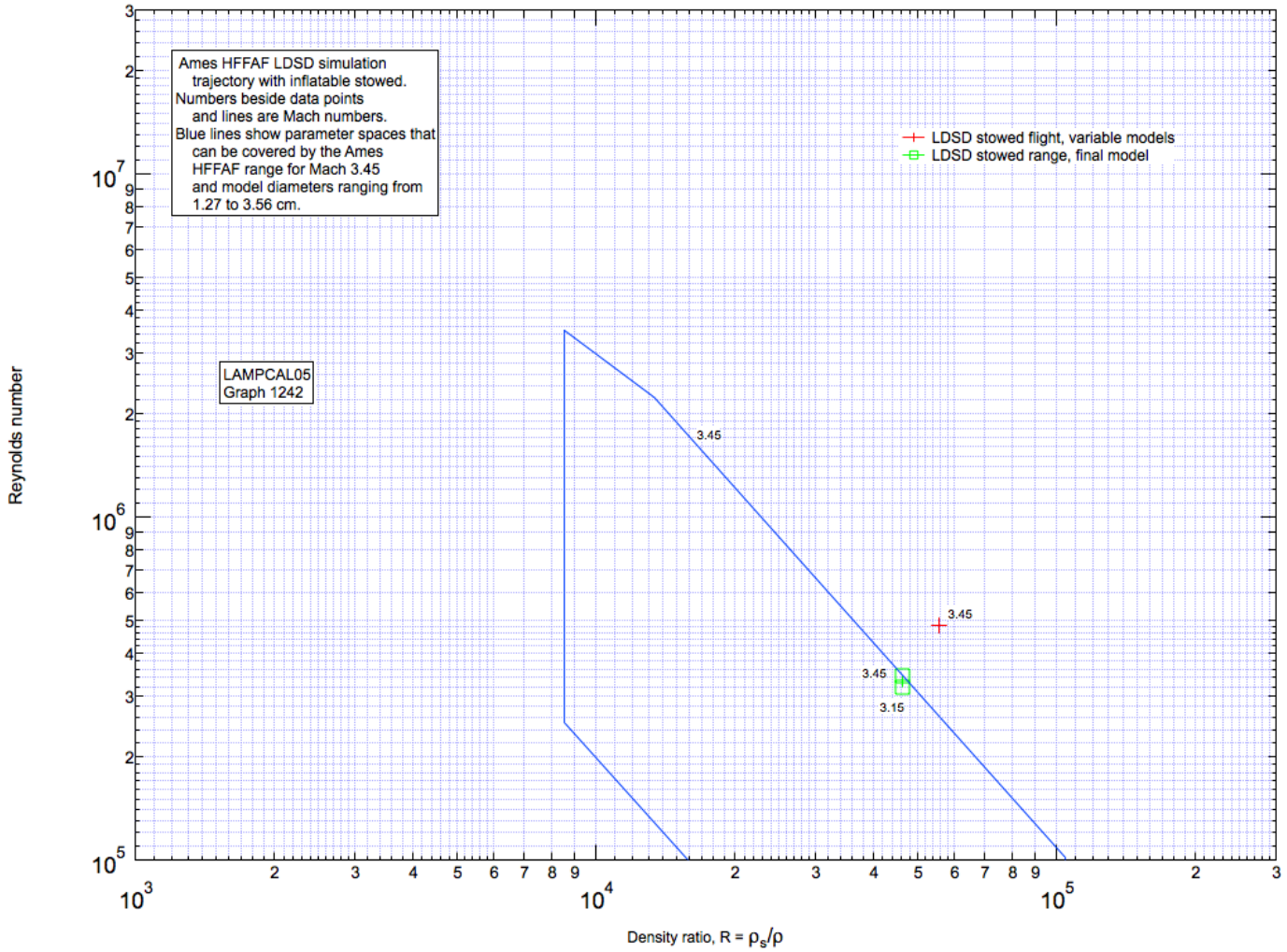

Fig. 12. Ames HFFAF LDSD simulation trajectory with inflatable stowed. Red data point is un-attainable (in range) condition. Upper green data point is closest attainable range condition. Solid blue lines show facility simulation capability for Mach 3.45 and a maximum model diameter of 3.56 cm. Lower green data point is alternate range operating condition at Mach 3.15.

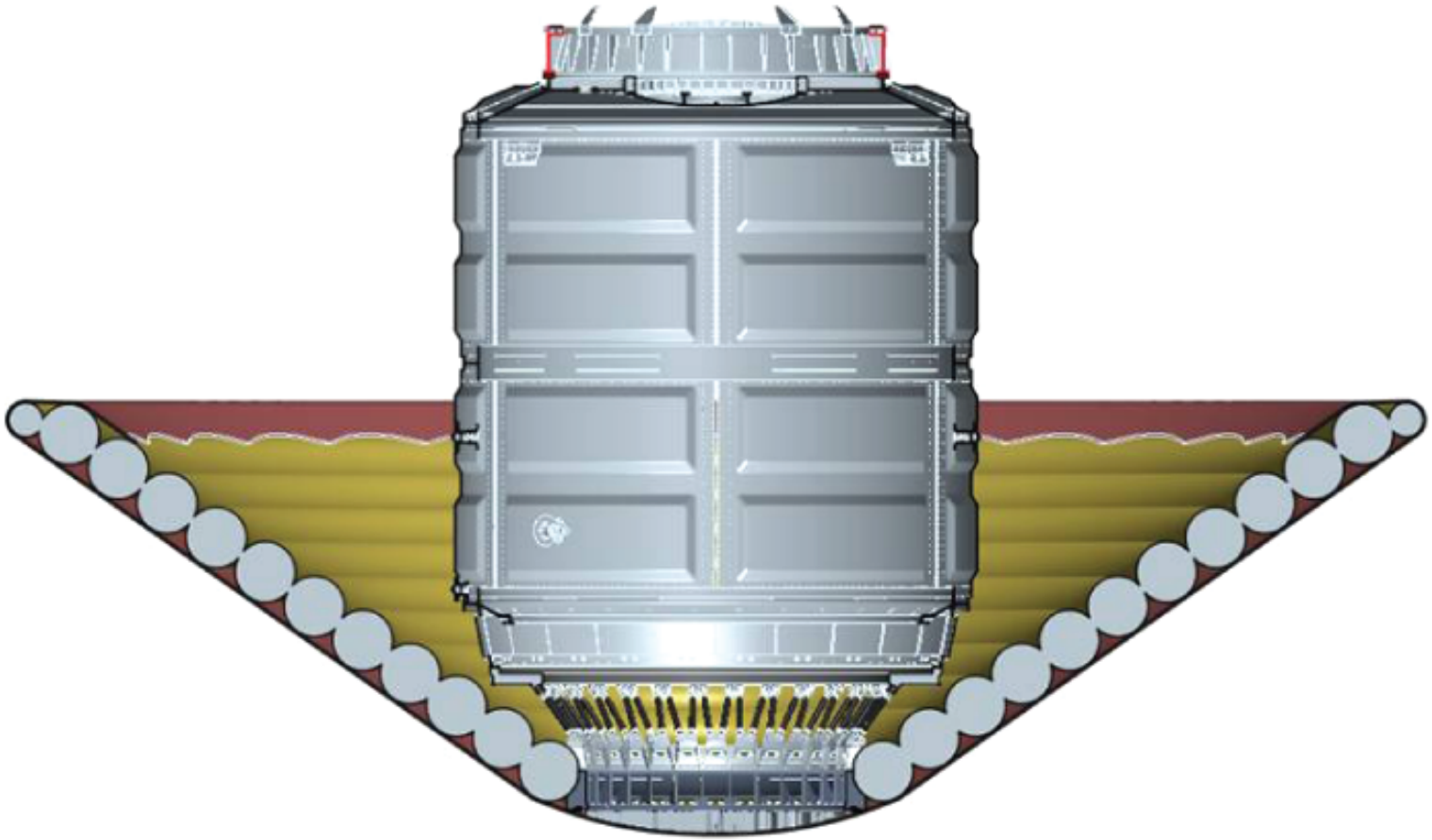

Fig. 13. HEART vehicle.

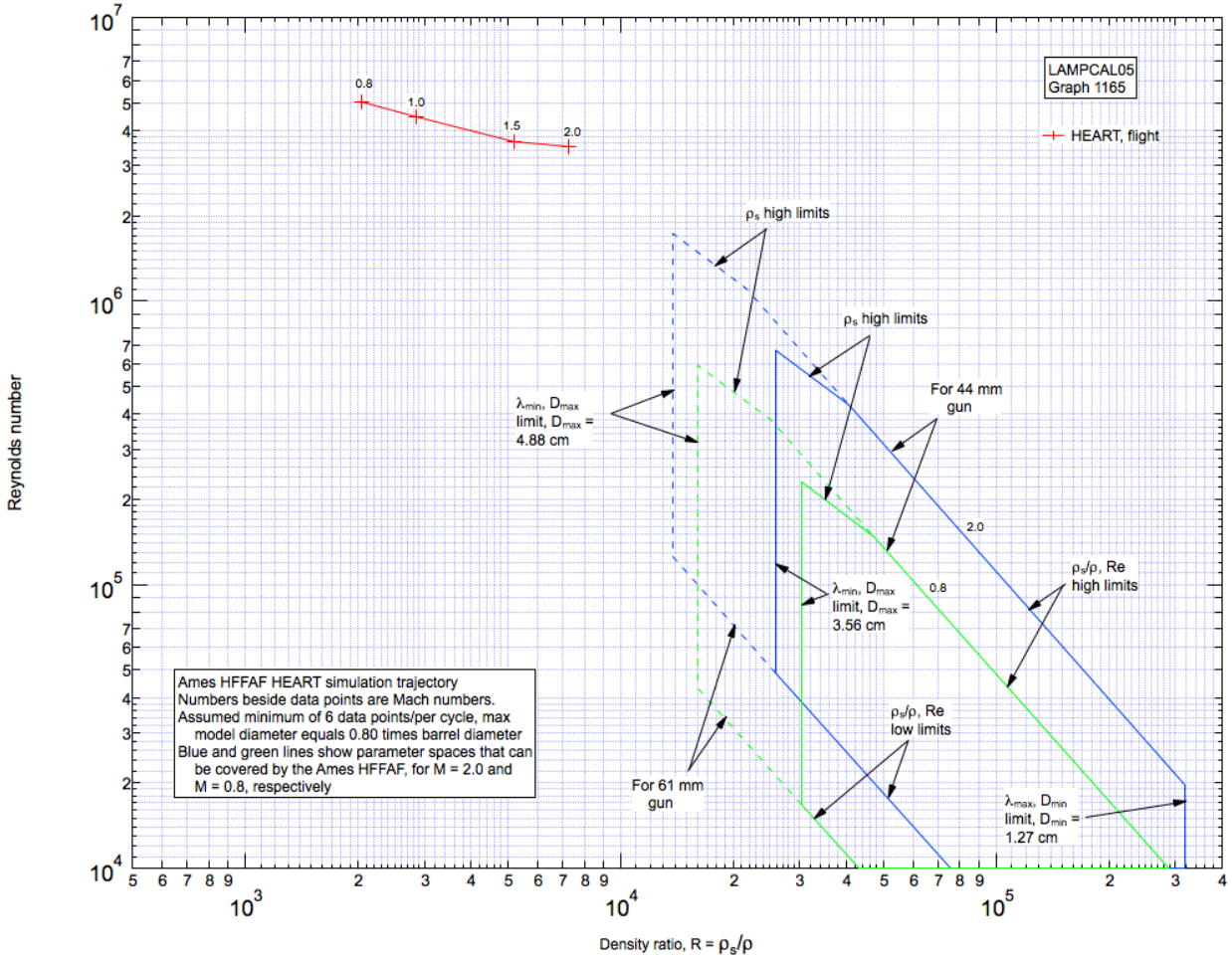

Fig. 14. Ames HFFAF HEART simulation trajectory. Blue lines show facility simulation capability for Mach 2.0 and maximum model diameters of 4.88 and 3.56 cm. (61 mm and 44 mm guns). Green lines show corresponding capabilities for Mach 0.8.

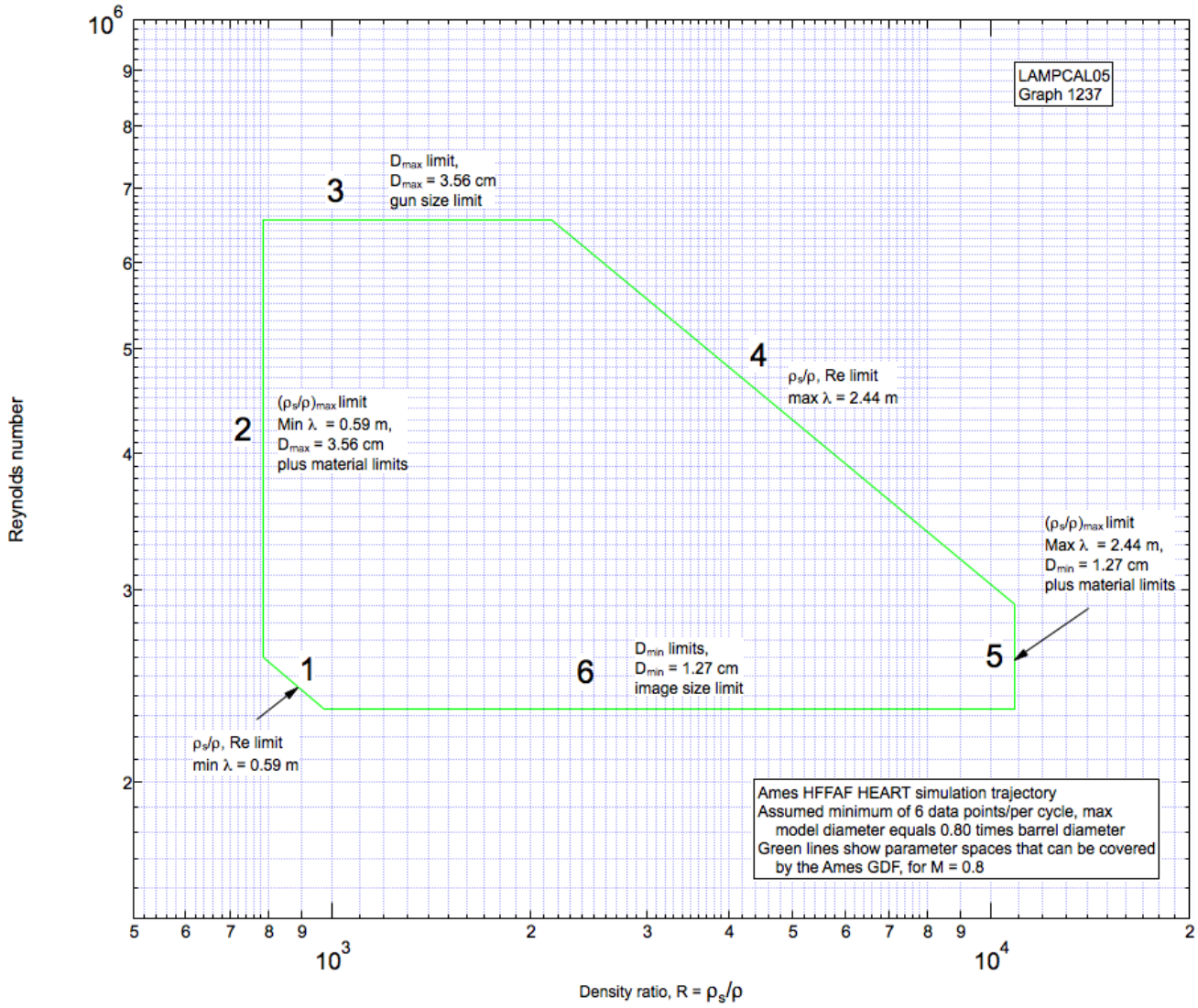

Fig. 15. Capabilities of the Ames GDF range for the HEART vehicle at the Mach 0.8 flight data point, using the Ames 44 mm powder gun.

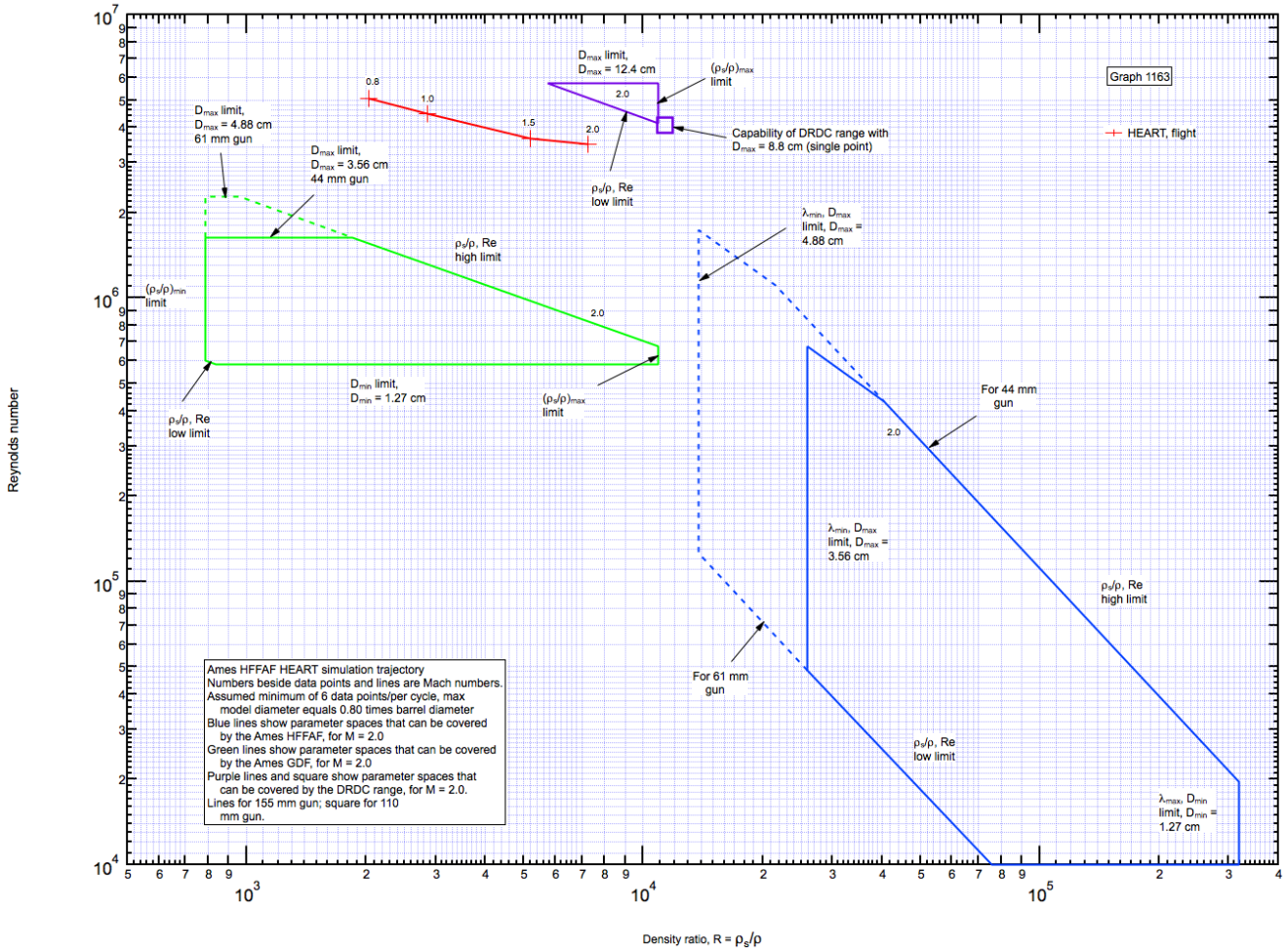

Fig. 16. HEART simulation trajectory. Blue lines show facility simulation capability for Ames HFFAF facility for Mach 2.0 and maximum model diameters of 4.88 and 3.56 cm. (61 mm and 44 mm guns). Green lines show the corresponding simulation capability for the Ames GDF facility. Purple lines show the corresponding simulation capability for the DRDC facility with maximum model diameters of 8.80 and 12.4 cm (110 mm and 155 mm guns).

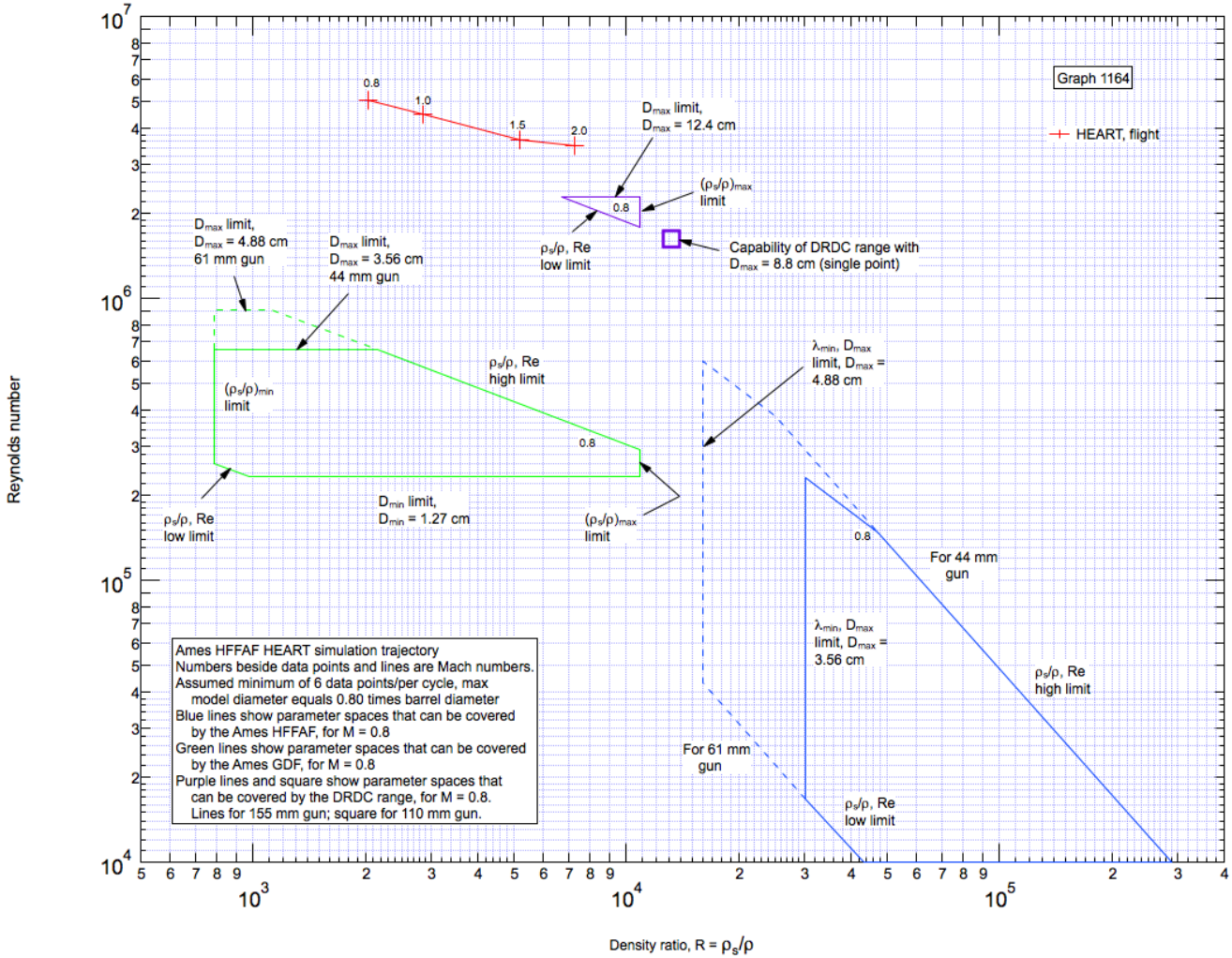

Fig. 17. HEART simulation trajectory. Blue lines show facility simulation capability for Ames HFFAF facility for Mach 0.8 and maximum model diameters of 4.88 and 3.56 cm. (61 mm and 44 mm guns). Green lines show the corresponding simulation capability for the Ames GDF facility. Purple lines show the corresponding simulation capability for the DRDC facility with maximum model diameters of 8.80 and 12.4 cm (110 mm and 155 mm guns).

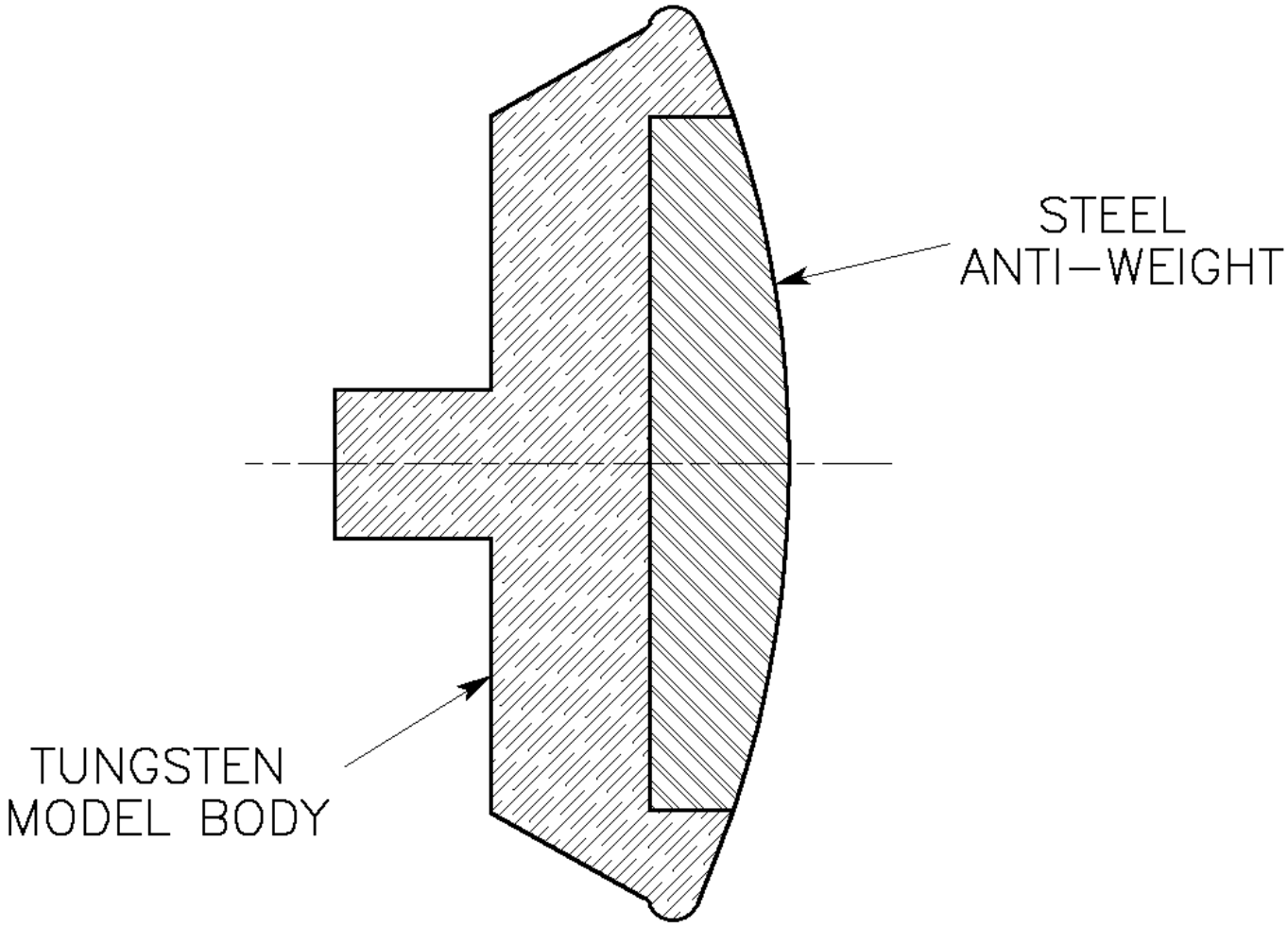

Fig. 18. Ballistic range model with press-fit nose “anti-weight”.

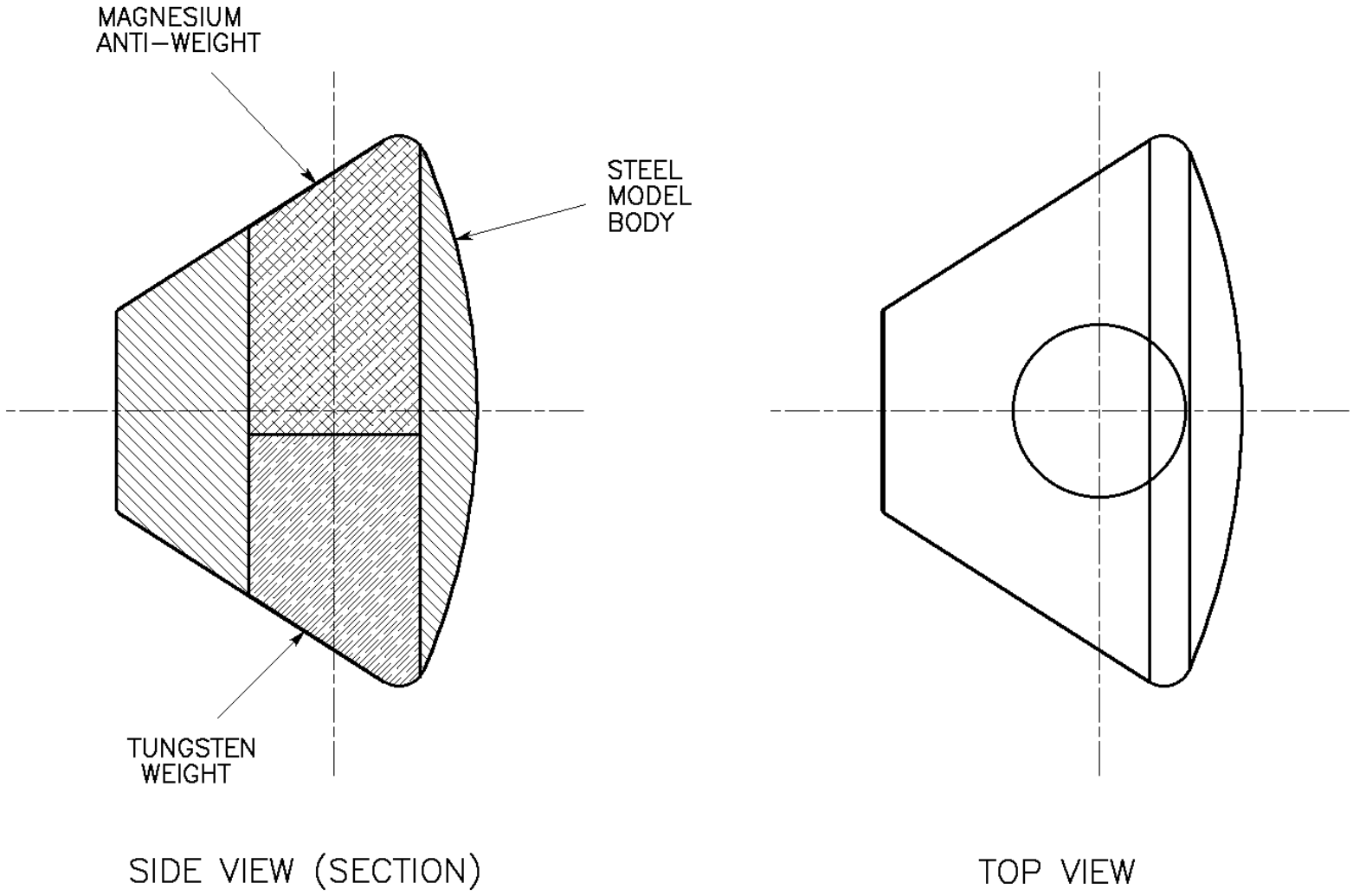

Fig. 19. Ballistic range model with sideways press-fit weight and "anti-weight" to adjust lateral position of CG.

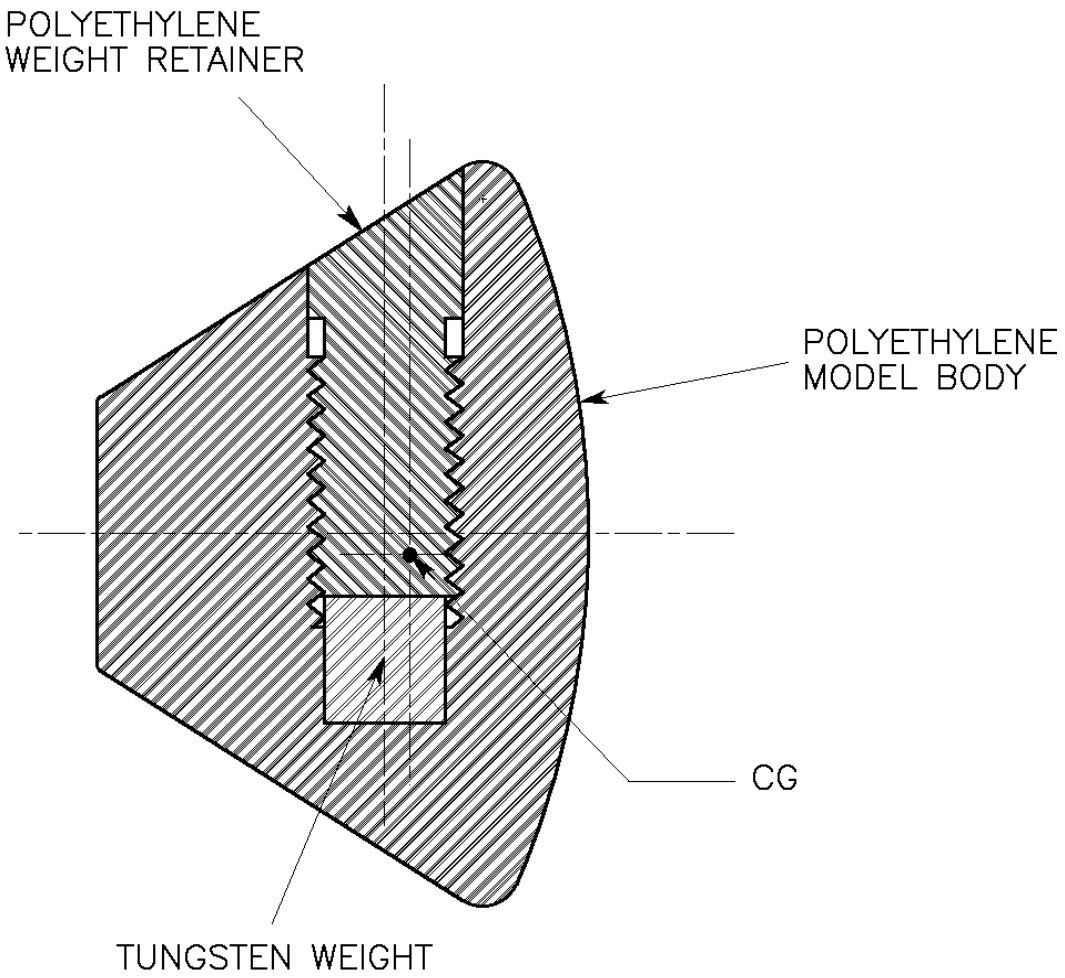

Fig. 20. Ballistic range model with sideways offset weight trapped by threaded retainer to adjust lateral position of CG.

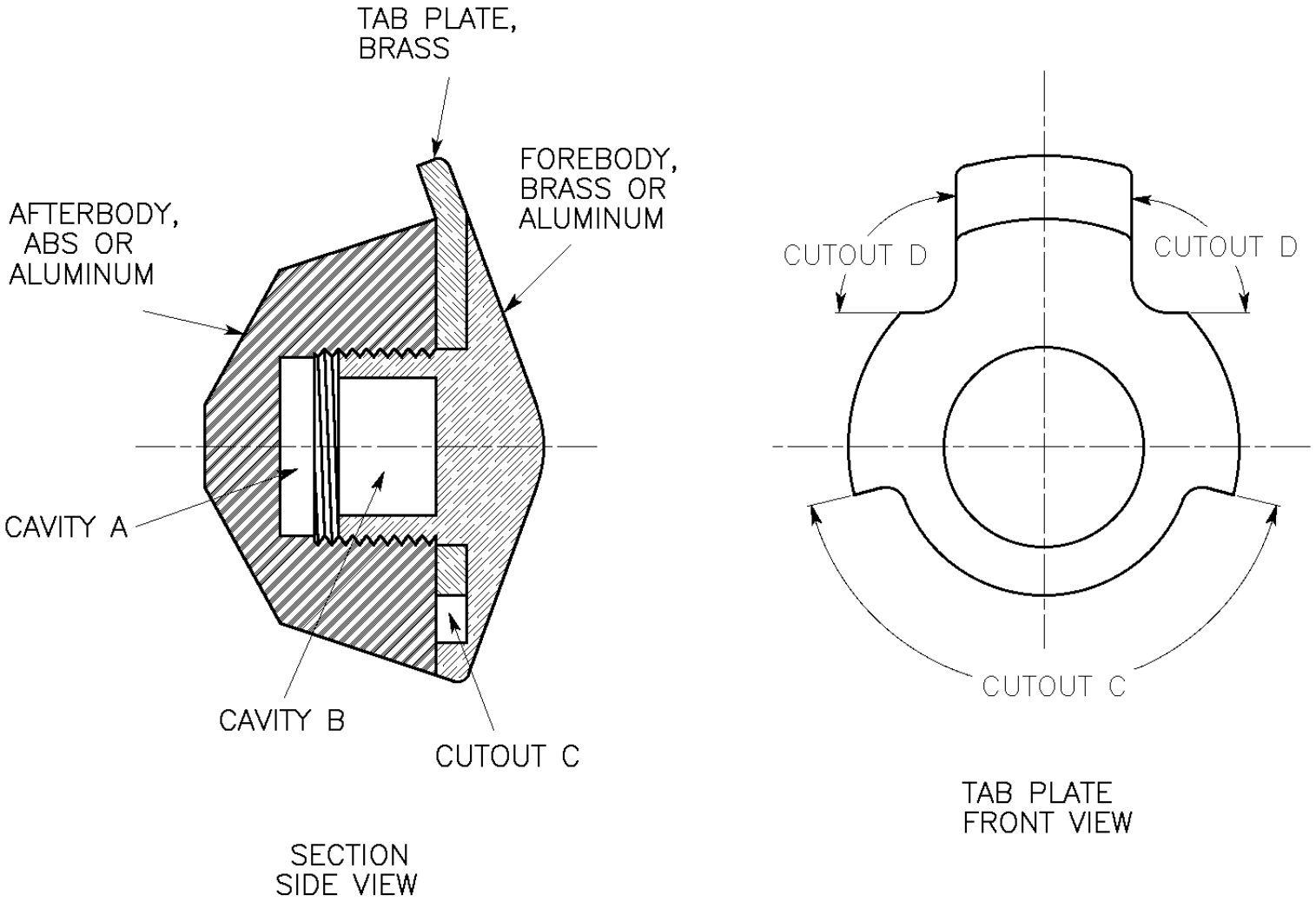

Fig. 21. Three piece tabbed model. Several methods of adjusting the axial and lateral position of the CG of this model are discussed in the text.

Fig. 22. Model inside 3 of 4 serrated sabot fingers. Fourth sabot finger is off to the right.

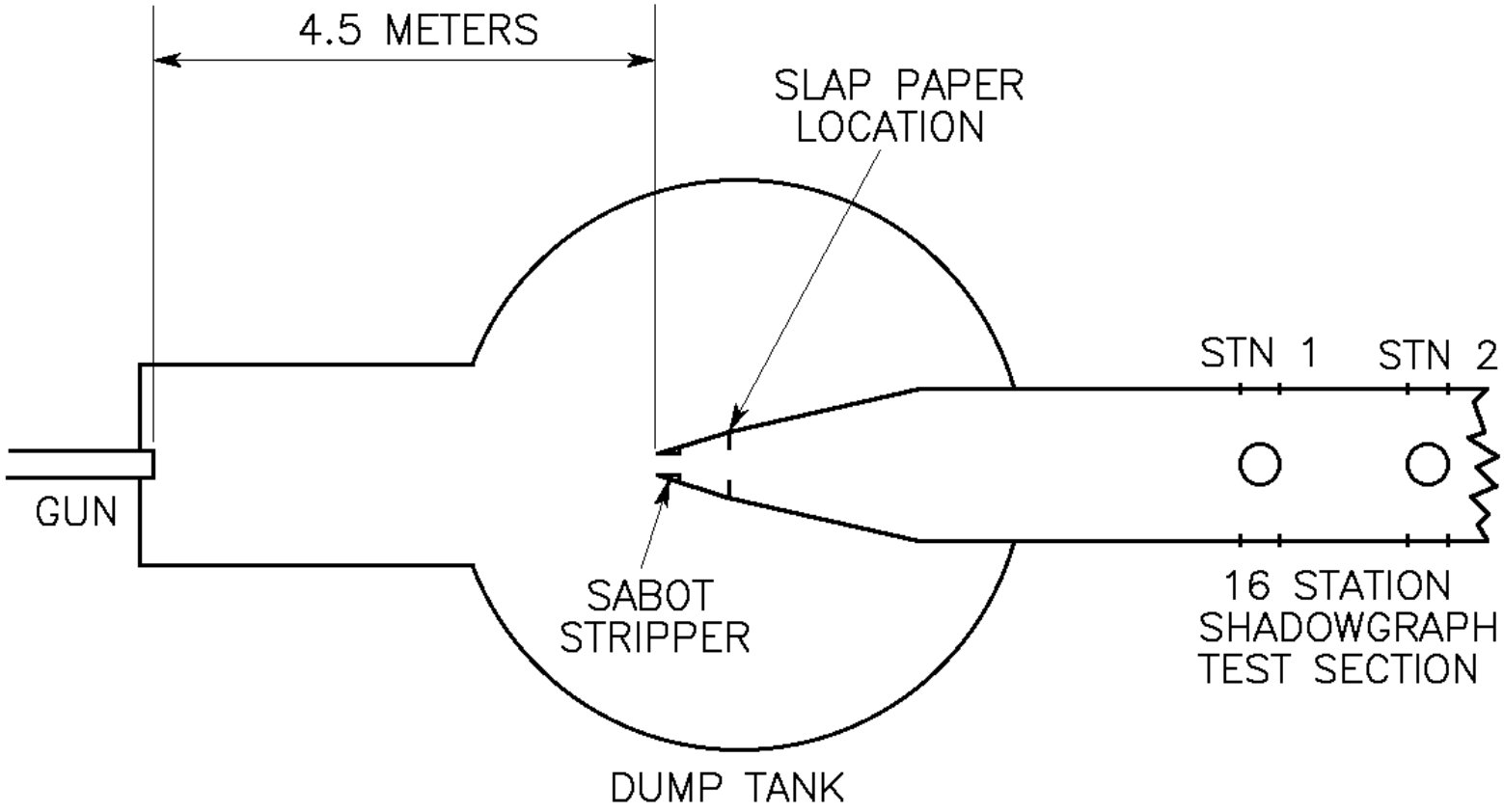

Fig. 23. Arrangement of gun, dump tank, sabot stripper and shadowgraph range for the NASA Ames HFFAF facility.

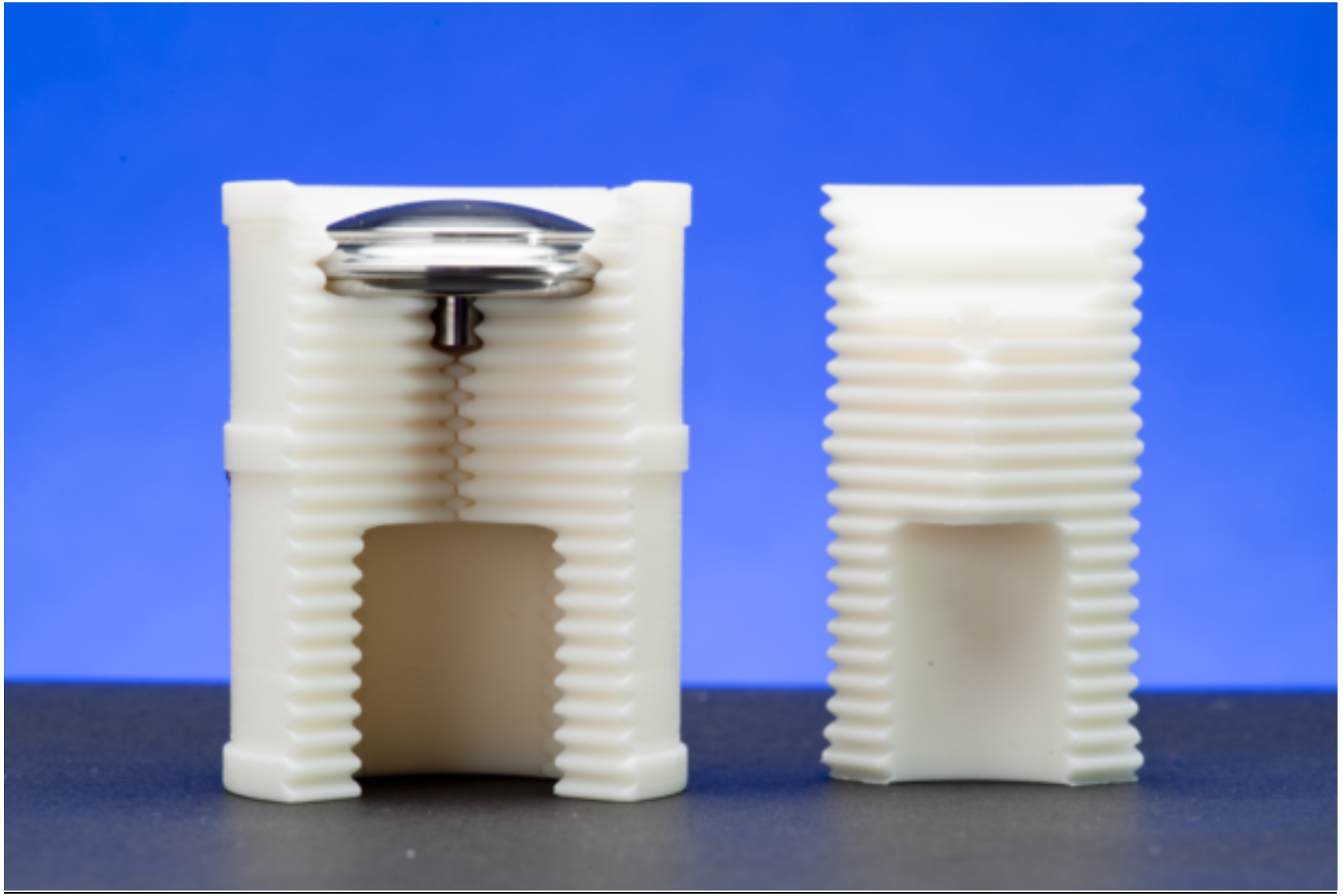

Fig. 24. Launch package designed to use both aerodynamic (ram air) and muzzle blast sabot separation forces.

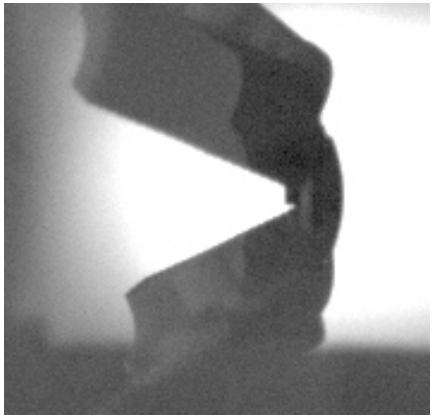

(a) x = 1.086 m

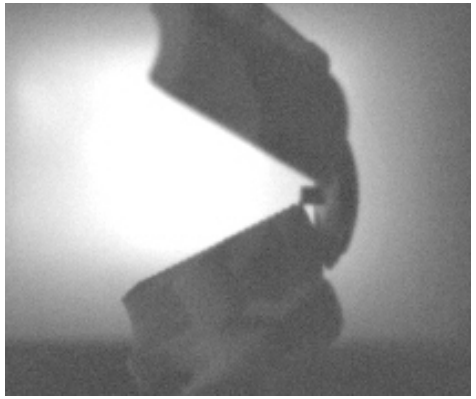

(b) x = 1.239 m

(c) x = 1.990 m

(d) x = 2.167 m

Fig. 25. Frames from sabot separation videos for the launch package shown in Fig. 21. Distances are from the muzzle of the gun.

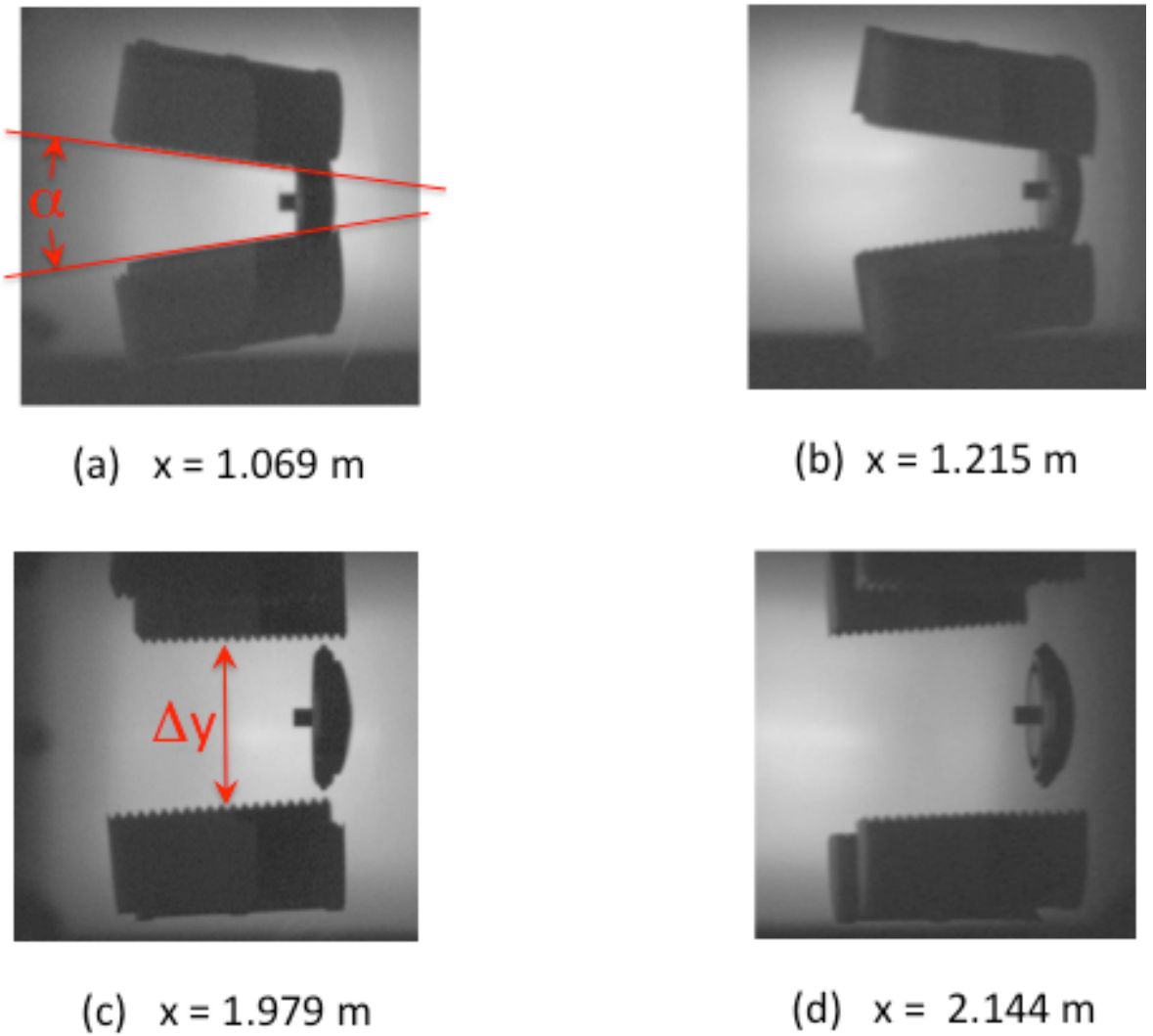

Fig. 26. Frames from sabot separation videos for a launch package identical to that shown in Fig. 21 except without the muzzle blast cavity. Distances are from the muzzle of the gun.

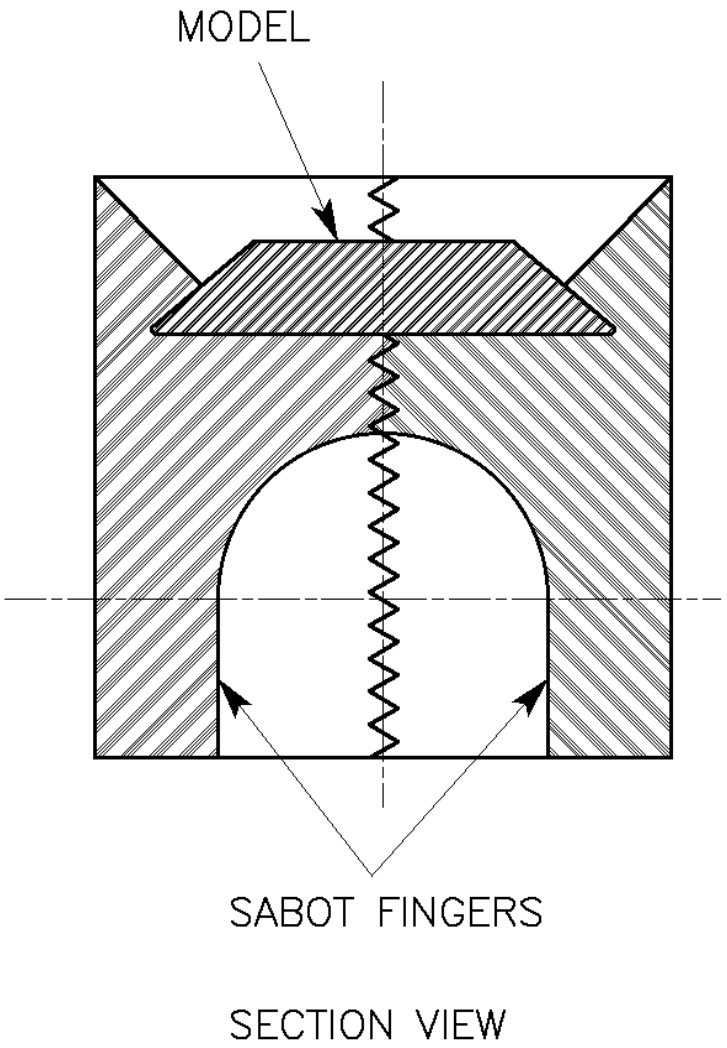

Fig. 27. Launch package for launch of very light model into vacuum using muzzle blast sabot separation.

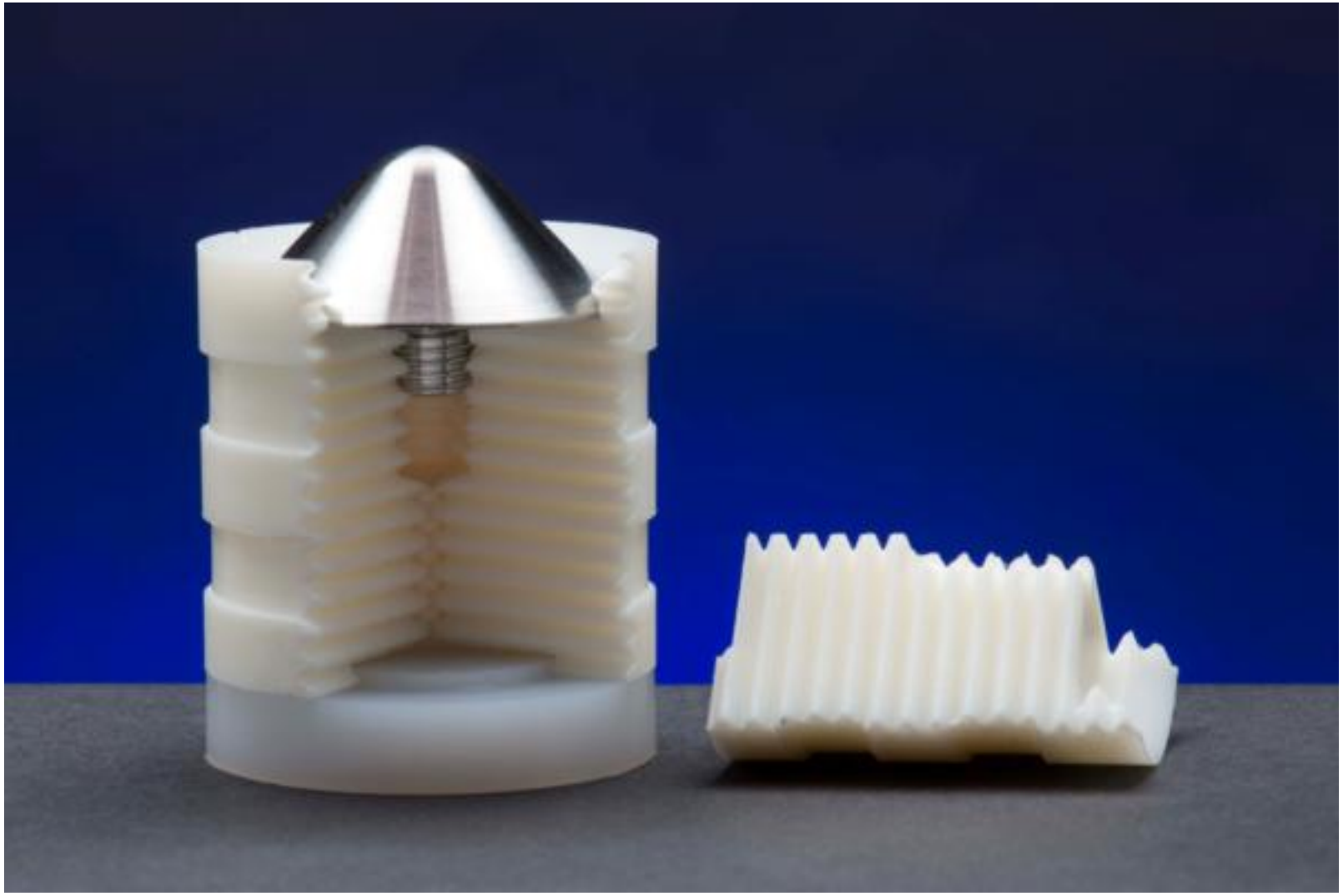

Fig. 28. Launch package with obturator cup (beneath sabot fingers) designed for aerodynamic sabot finger separation.

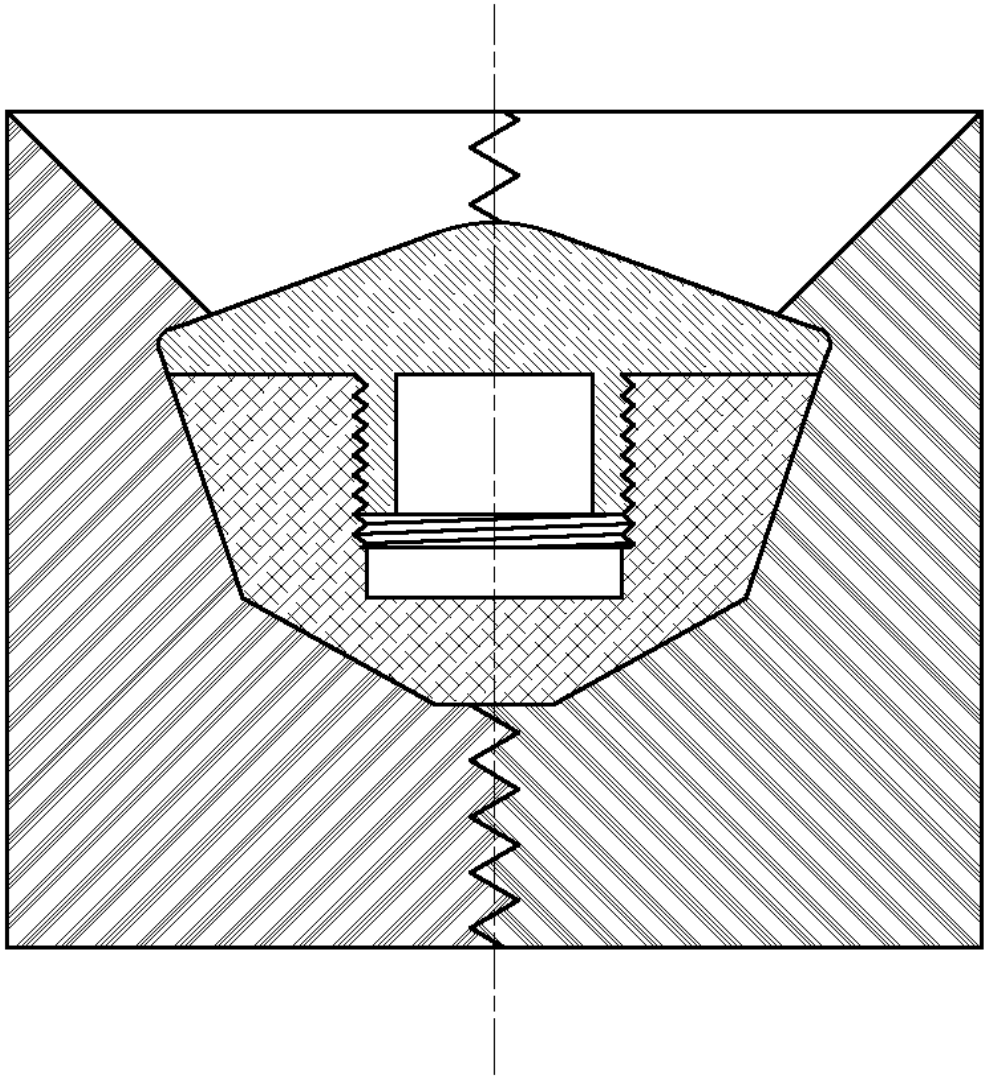

Fig. 29. Section view of NASA Ames Mars Science Laboratory (MSL) model in sabot. Sabot comprises four serrated sabot fingers as seen in Fig. 28.

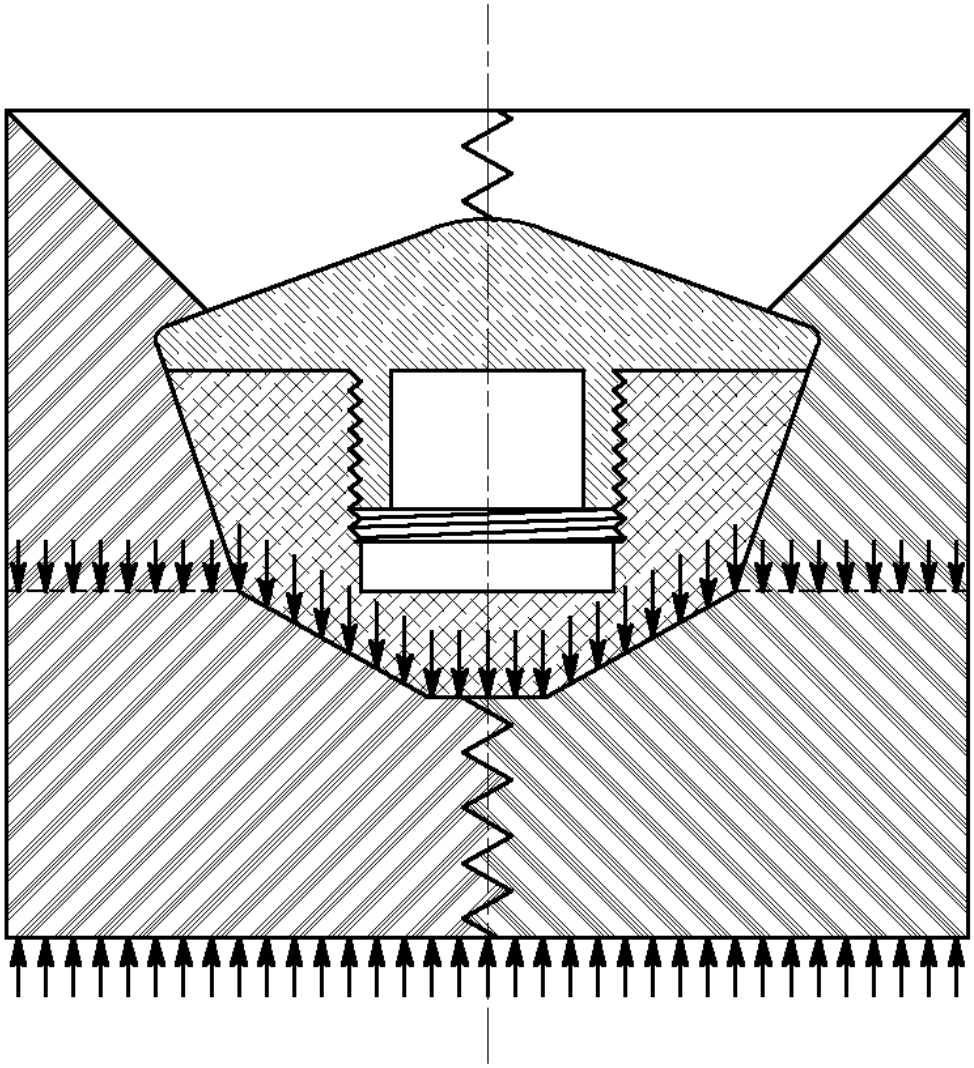

Fig. 30. Section view of MSL model in sabot. The arrows show the high bearing stresses below model, the lower (nearly hydrostatic) stresses away from the model base and the drive gas pressures below the sabot.

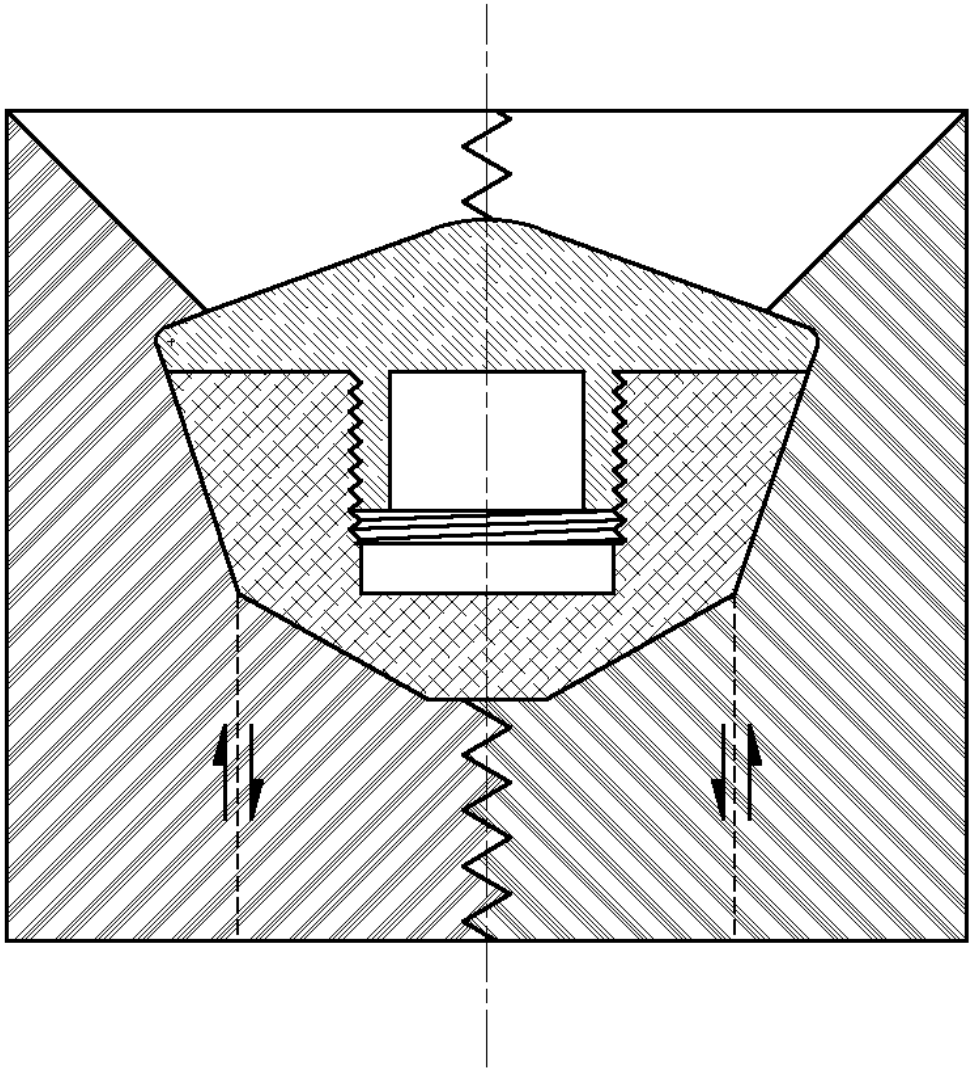

Fig. 31. Section view of MSL model in sabot. Shear stresses tending to allow model to "fall" through sabot are shown.

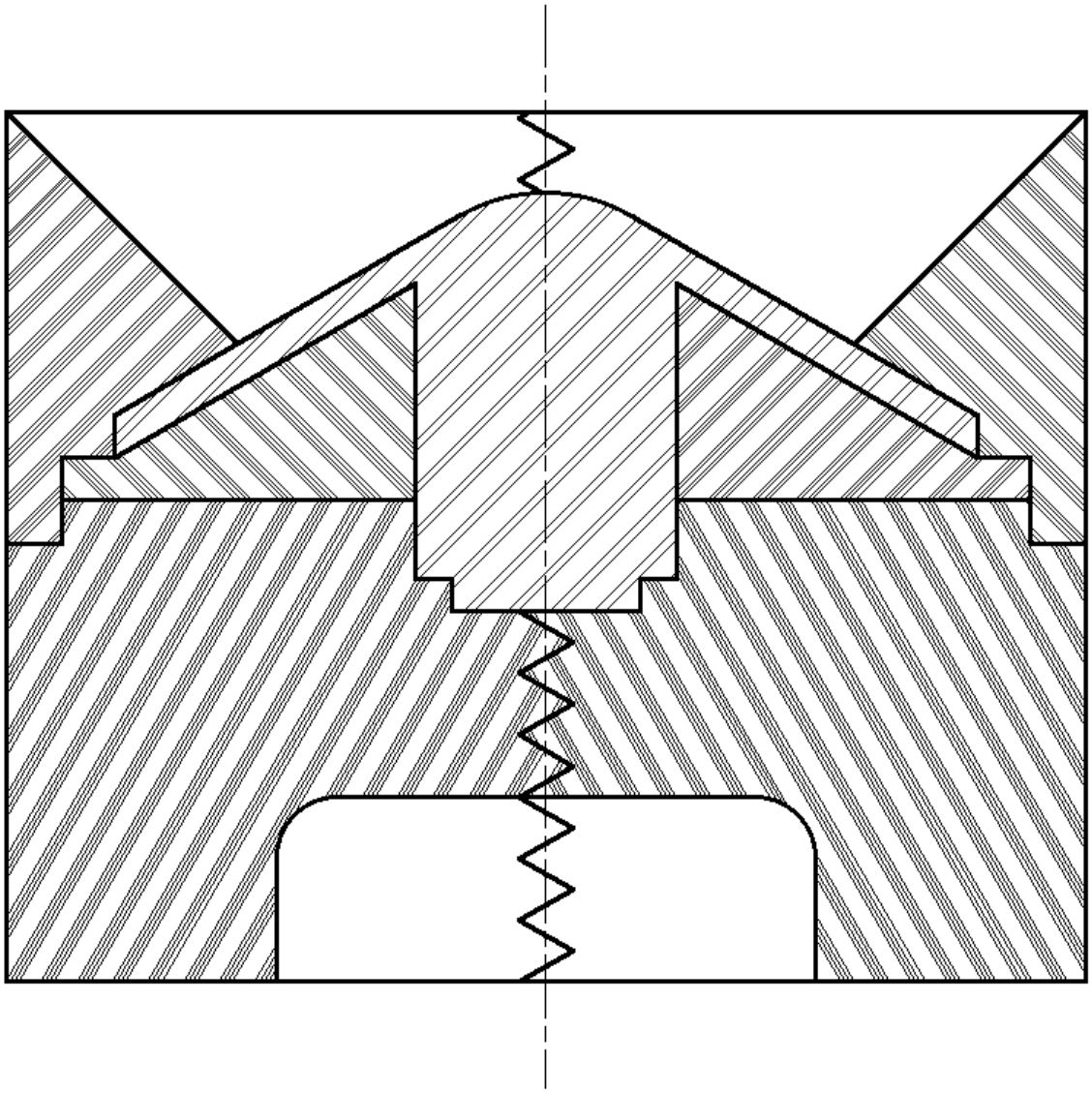

Fig. 32. Section view of range model of HEART vehicle in launch sabot. Model has a compact centerbody and a relatively thin aerobrake.

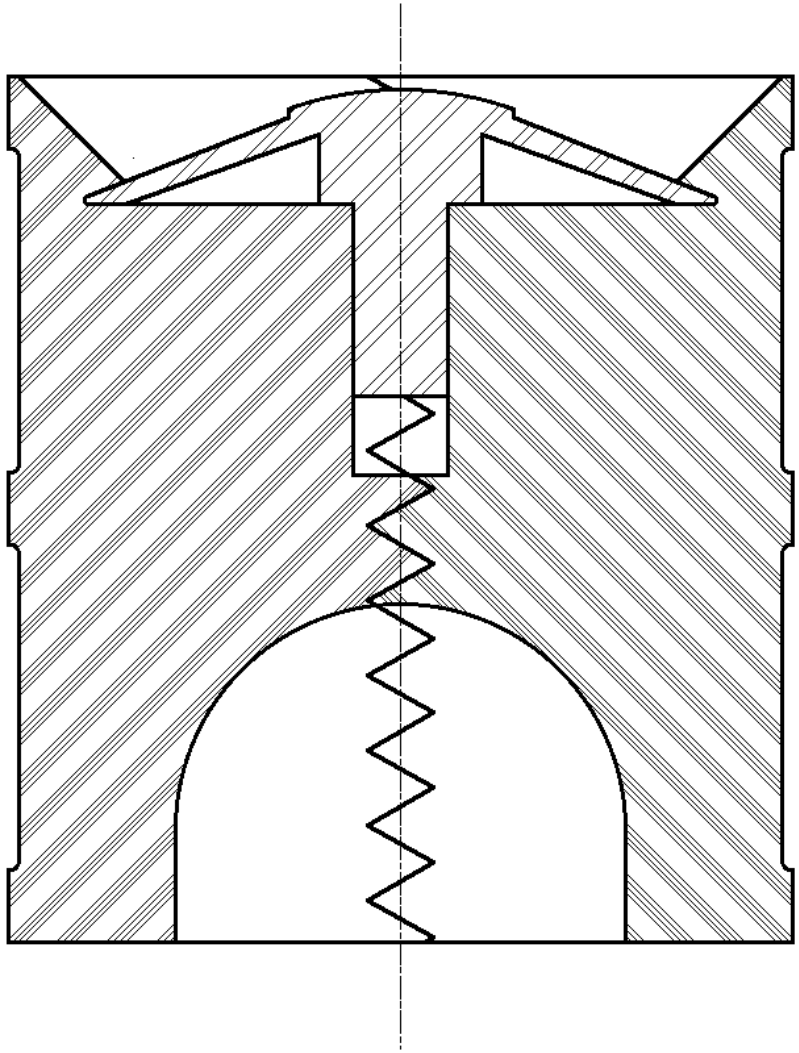

Fig. 33. Section view of range model of ADEPT vehicle in launch sabot. Model has a compact centerbody and a relatively thin aerobrake.

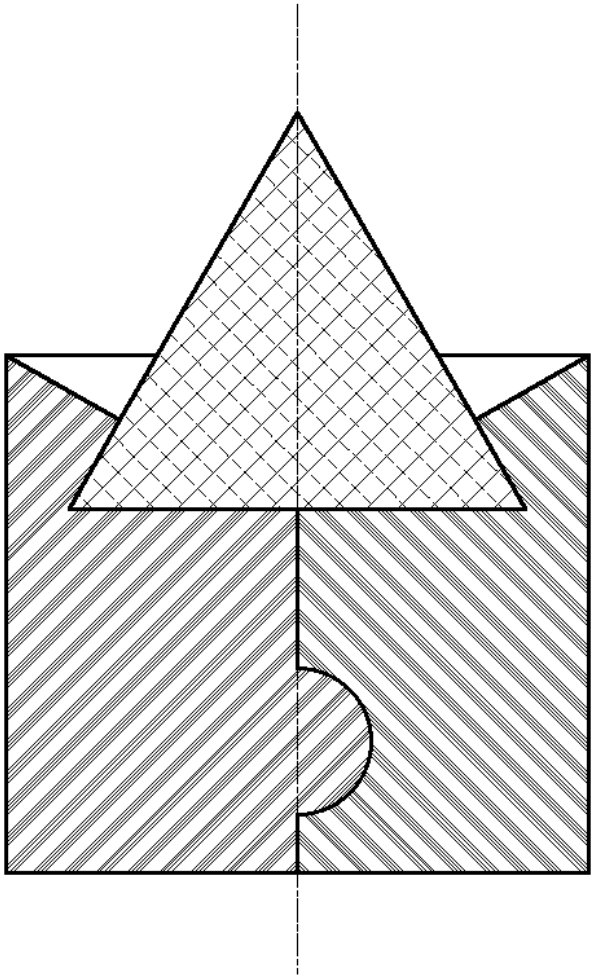

Fig. 34(a). From Fig. 3.36 in Ref. 13. Model is aluminum and polyethylene. Sabot is polycarbonate, launch at 7.3 km/sec. Two finger sabot.

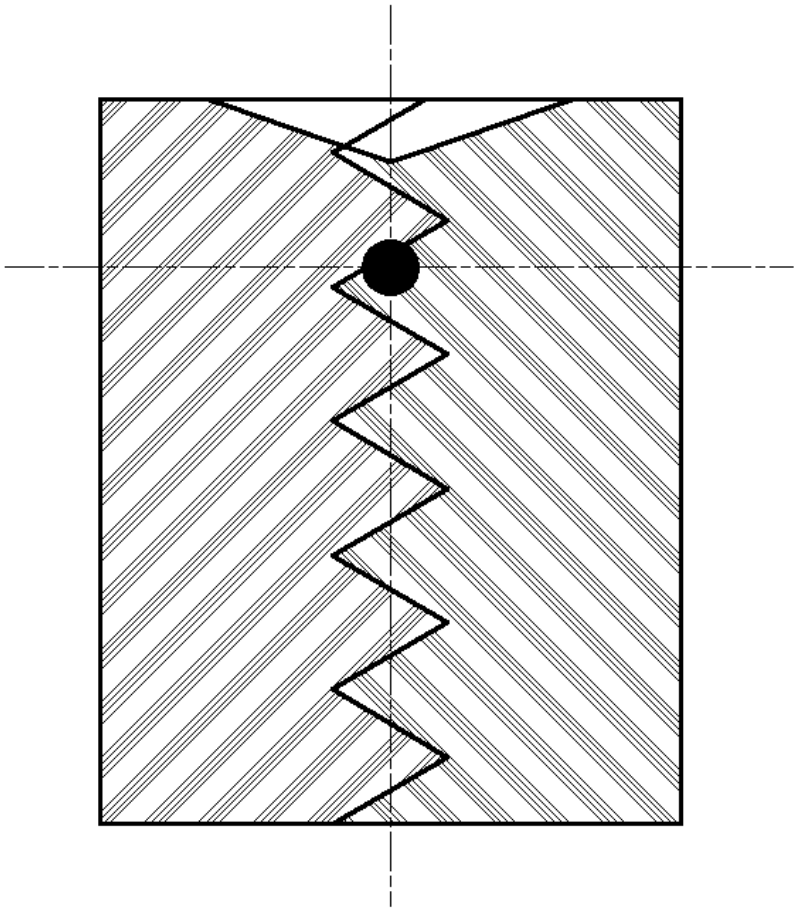

Fig. 34(b). From Fig. 3.39 in Ref. 13. Model is Al_2O_3. Sabot is unspecified plastic, launch at 8.0 km/sec. Four finger sabot.

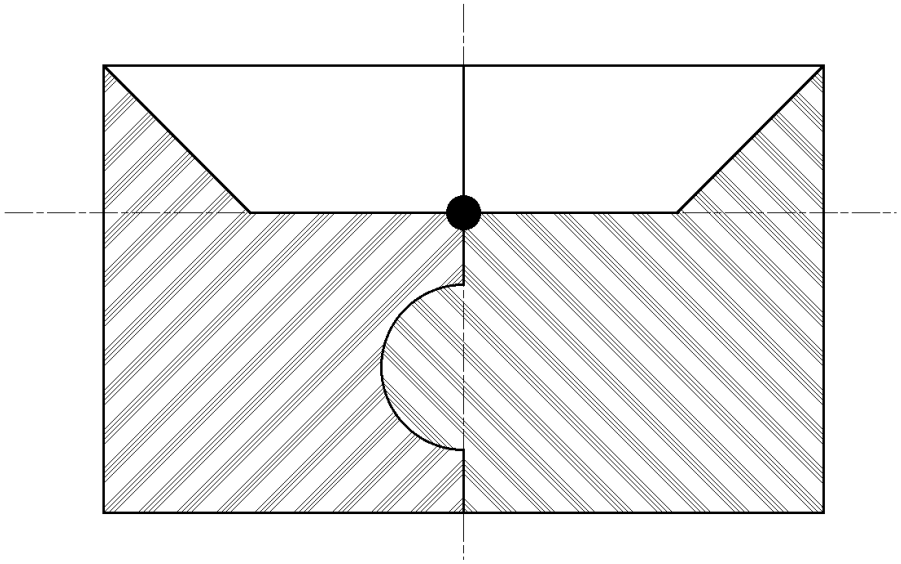

Fig. 35(a). From Fig. 3.41 in Ref. 13. Model is steel. Sabot is polycarbonate, launch at 8.3 km/sec. Two finger sabot.

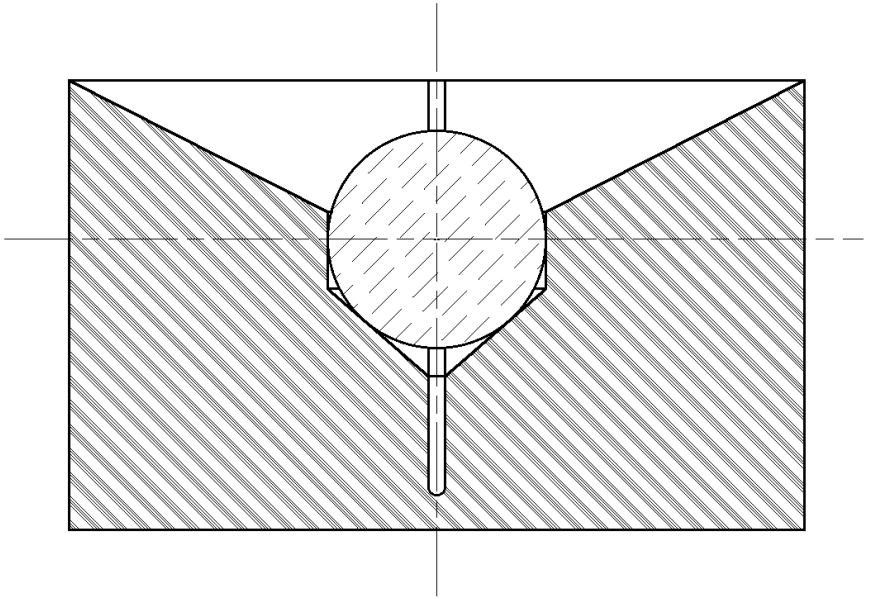

Fig. 35(b). From Fig. 3.42 in Ref. 13. Model is aluminum. Sabot is Nylon, launch at 9.4 km/sec. Sabot has two knife cuts at right angles almost through sabot.

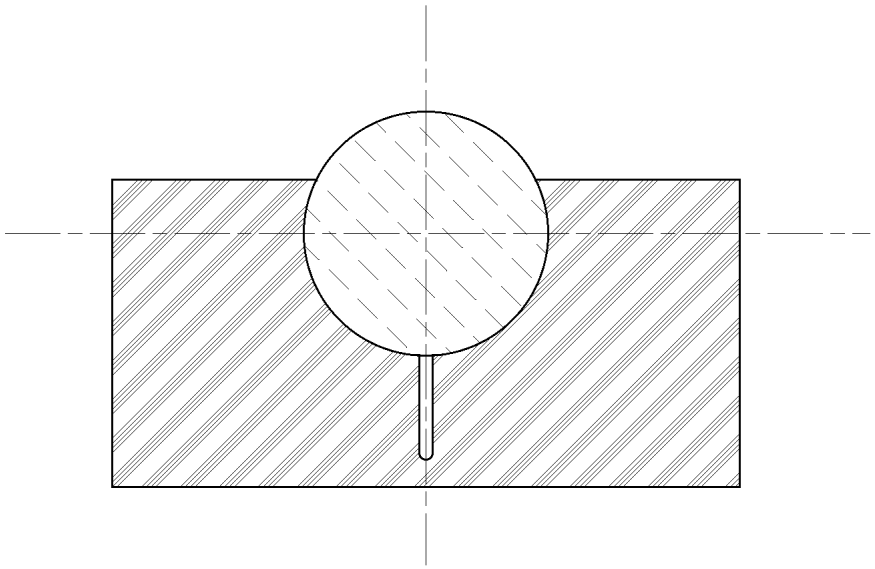

Fig. 36(a). From Fig. 3.43 in Ref. 13. Model is Pyrex. Sabot is polycarbonate, launch at 8.8 km/sec. Sabot has two knife cuts at right angles almost through sabot. Sphere diameter as scaled from drawing.

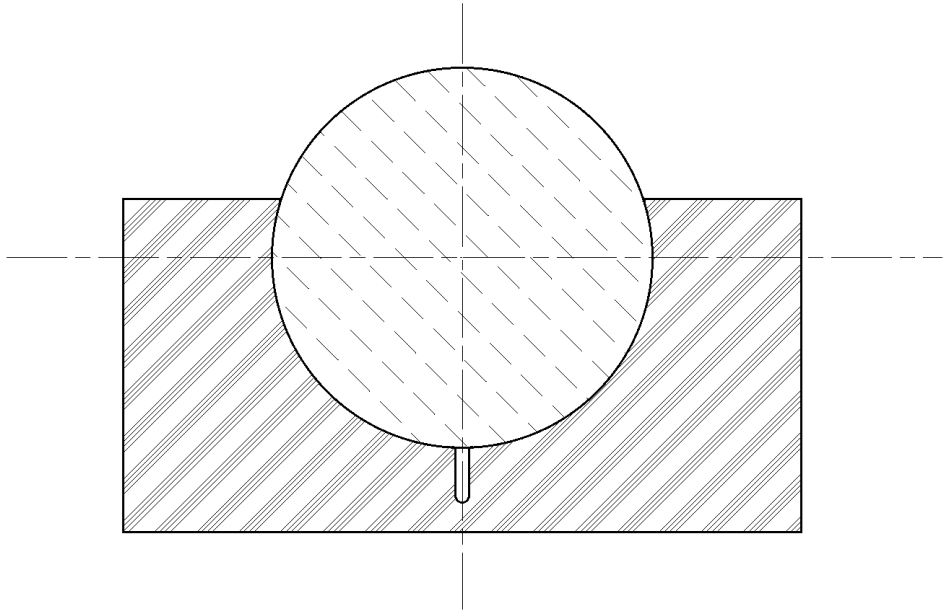

Fig. 36(b). From Fig. 3.43 in Ref. 13. Model is Pyrex. Sabot is polycarbonate, launch at 8.8 km/sec. Sabot has two knife cuts at right angles almost through sabot. Sphere size as stated in text of Ref. 13.

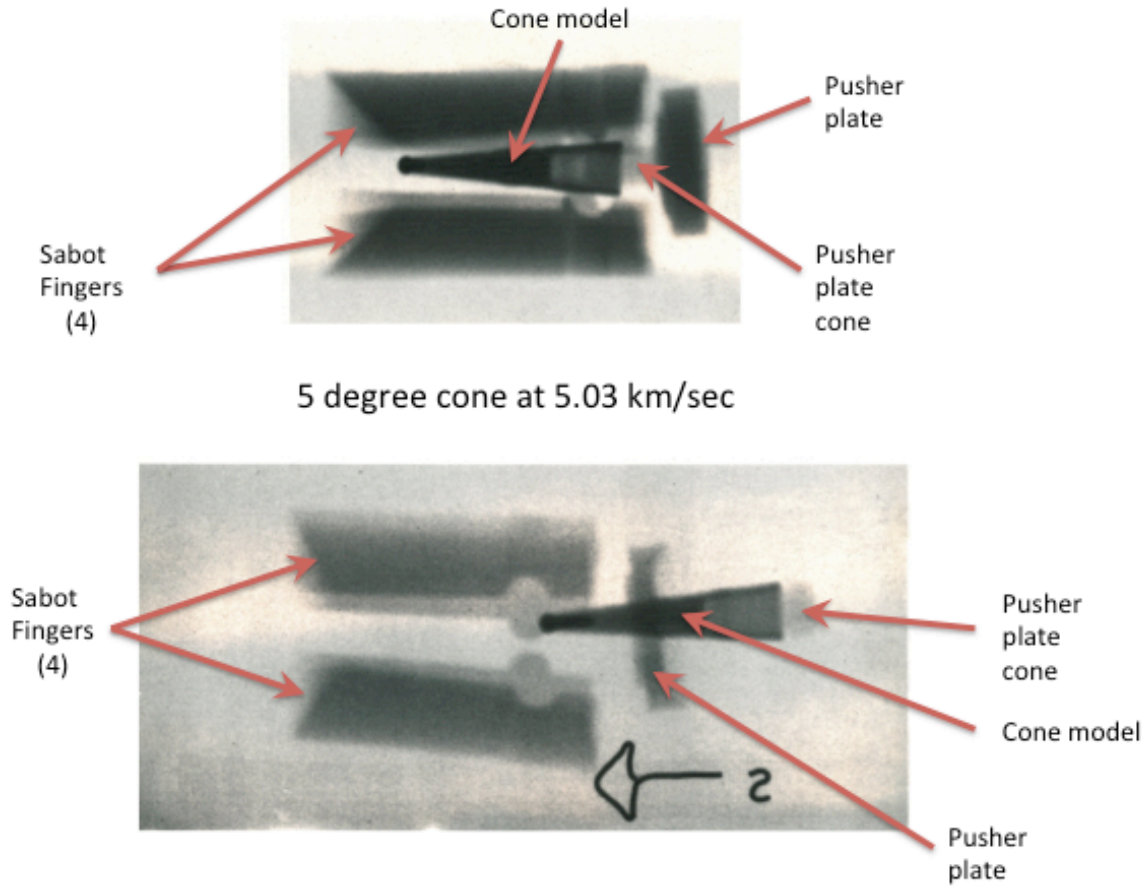

Fig, 37. X-ray pictures showing successful launch (upper picture) and failed launch (lower picture) of 5 degree cones. Failed launch is at a higher velocity and with a thinner pusher plate. In the failed launch, the model "fell" through the pusher plate and "cookie cut" out the pusher plate cone.

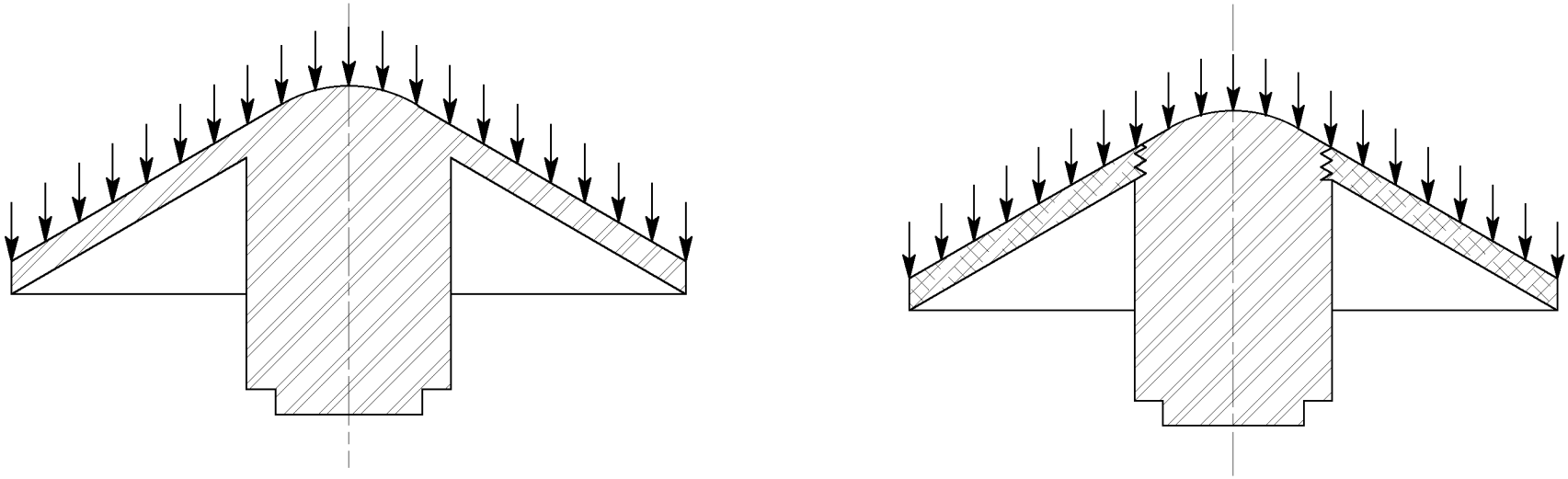

(a) *(b)*

Fig. 38. Aerodynamic forces on free flying model with compact centerbody surrounded by relatively thin aerobrake. (a) is one piece model and (b) is two piece model

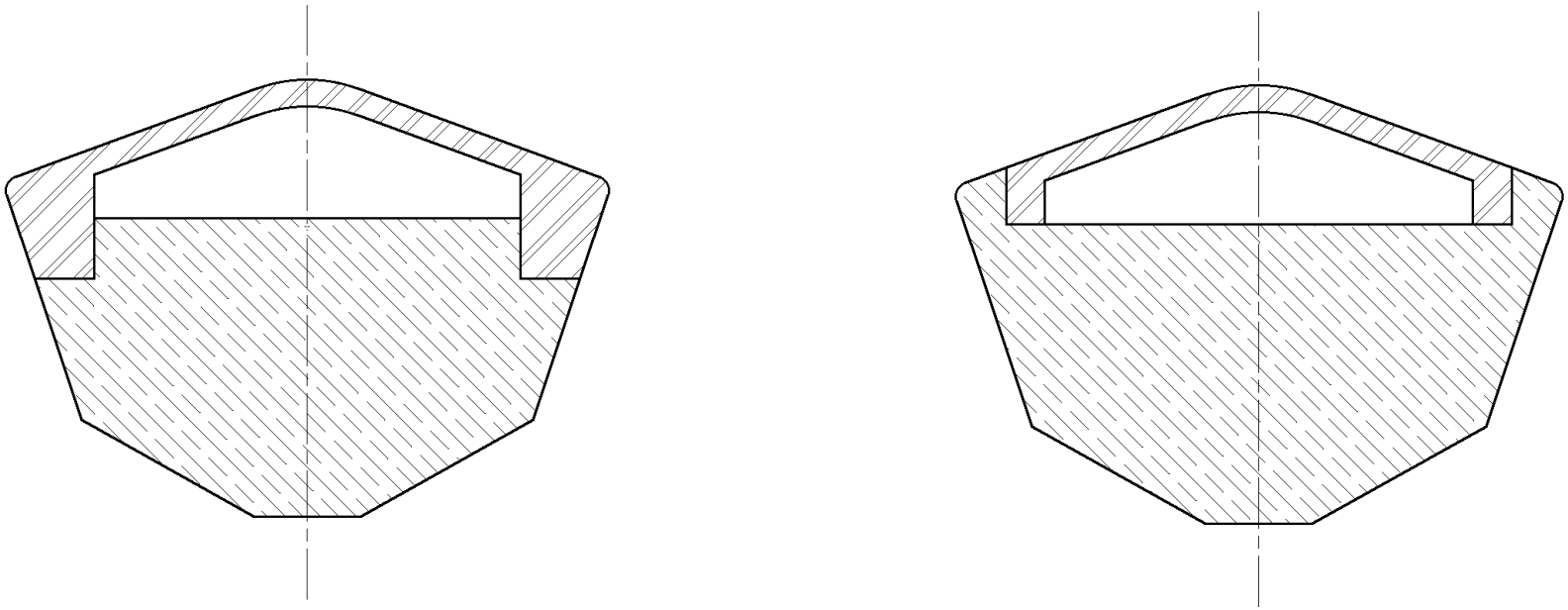

(a) *(b)*

Fig. 39. Compact models with thin front shells.

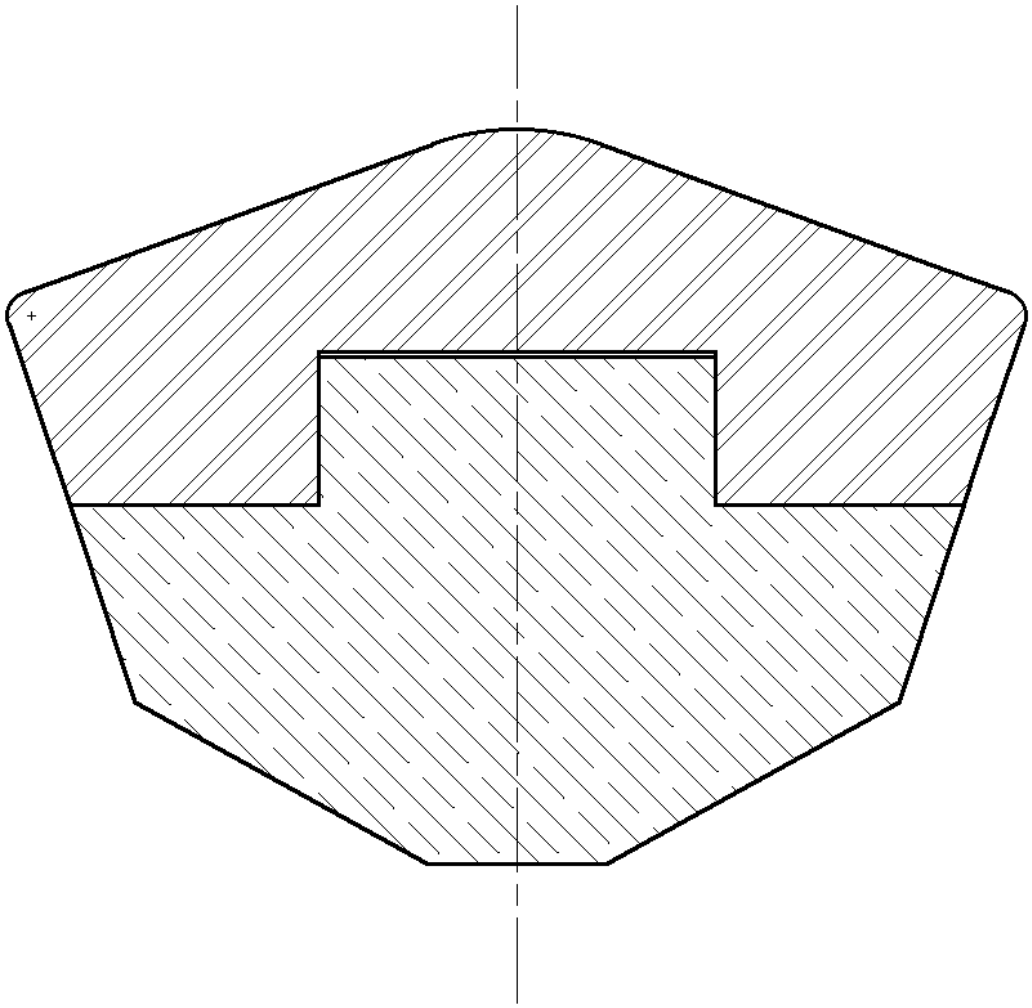

Fig. 40. Variation of compact models shown in Fig. 39 without thin front shell.

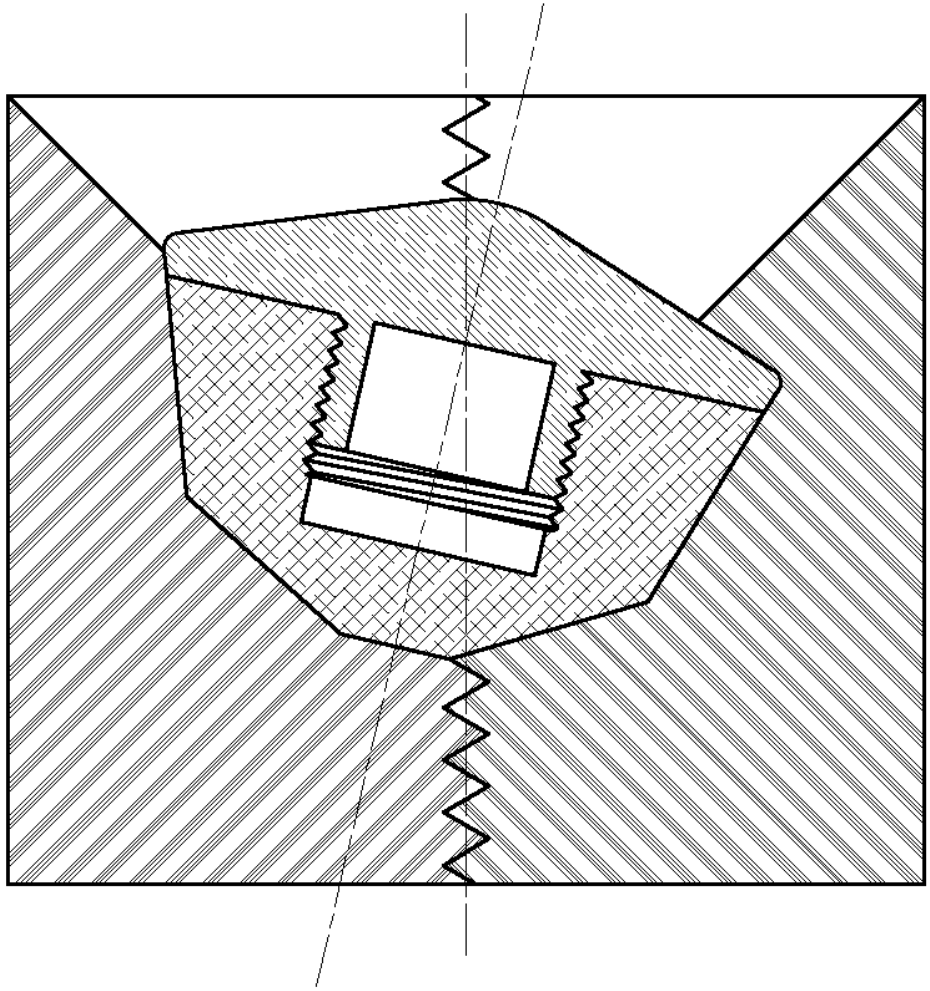

Fig. 41. Model of Fig. 29 in 13 degree tilted sabot.

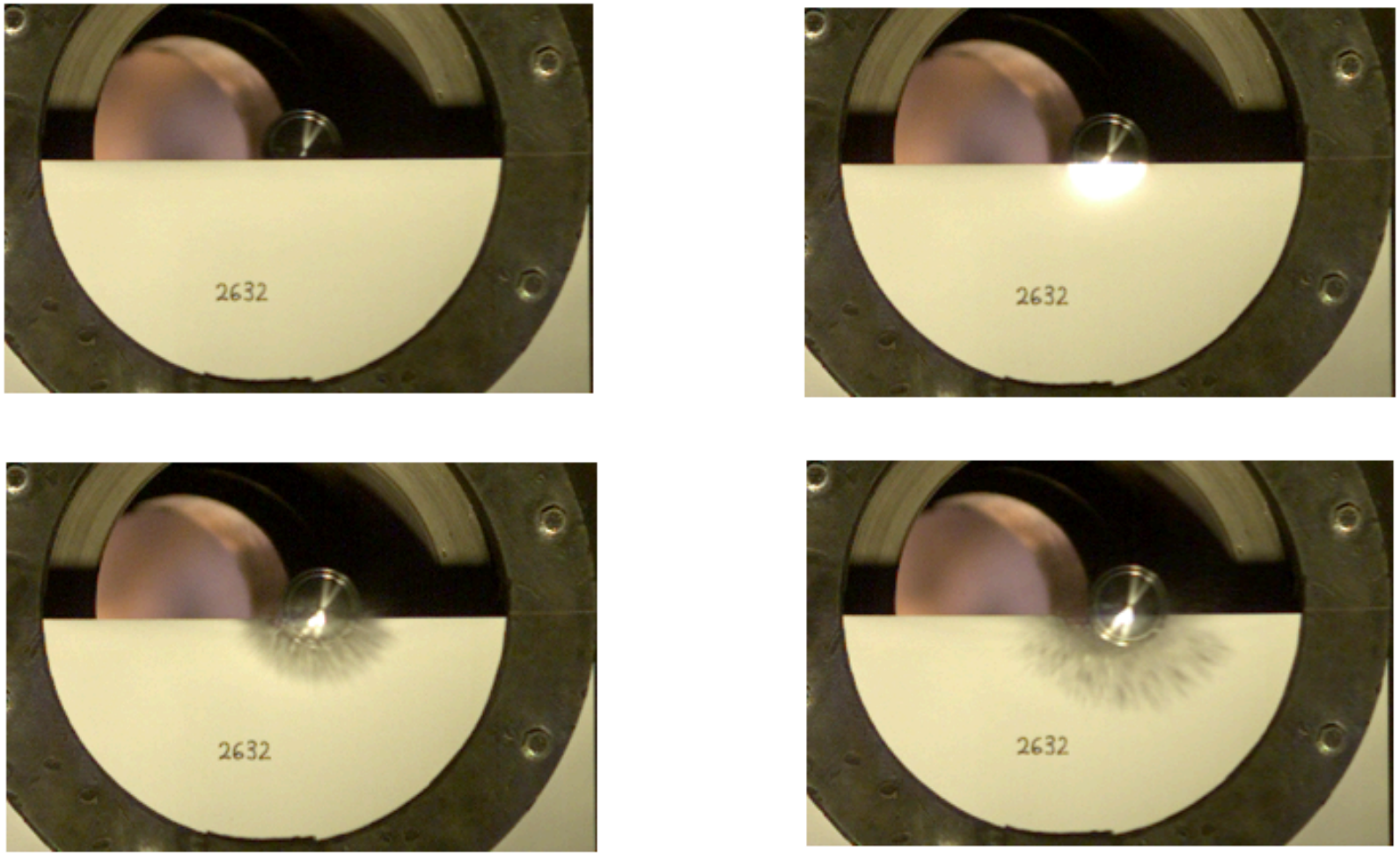

Fig, 42. Four frames from a high speed video showing a LDSD model penetrating the slap paper.

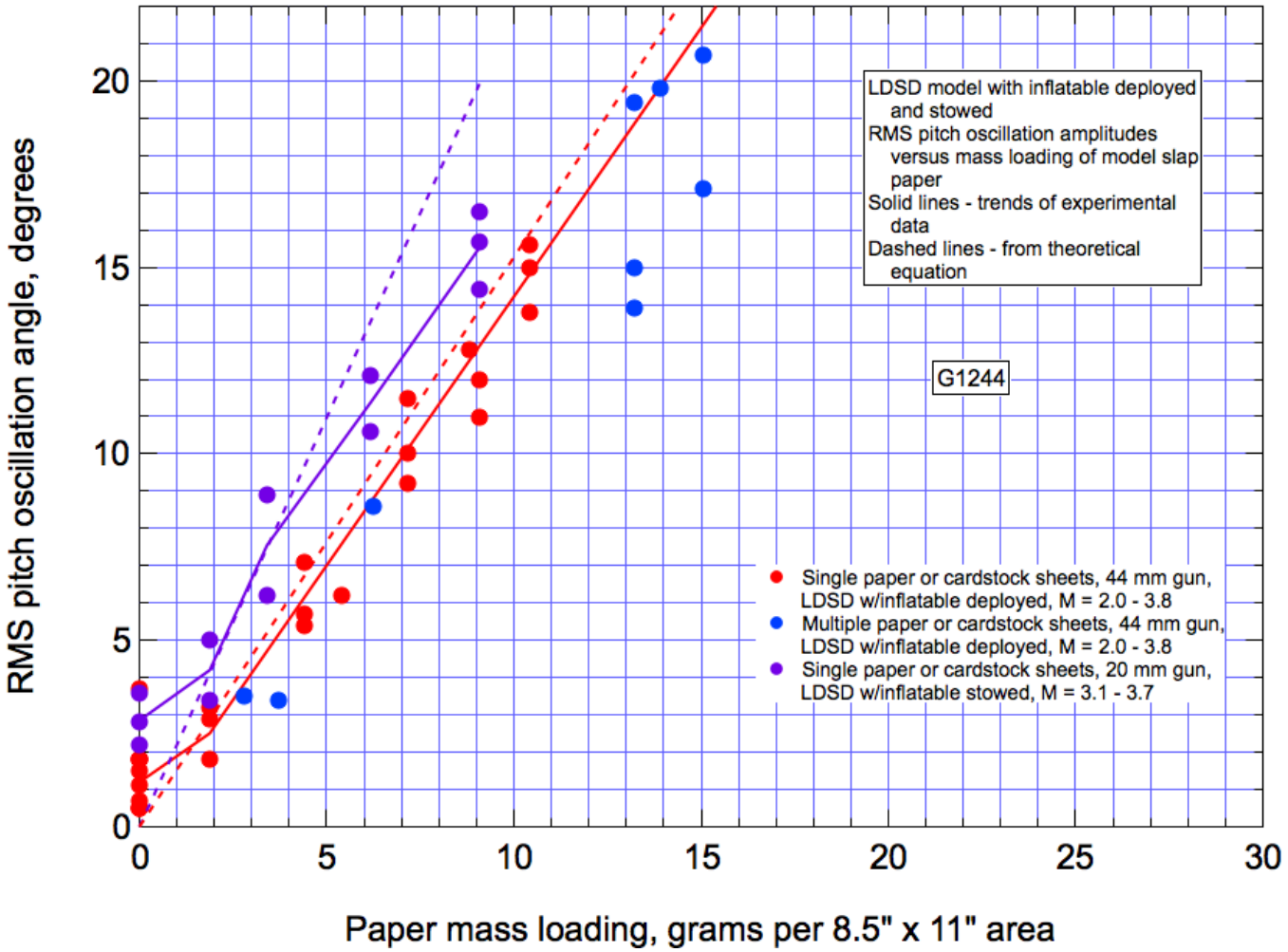

Fig. 43. RMS pitch oscillation amplitudes versus slap paper mass loading for two LDSD models launched in the NASA Ames HFFAF facility.

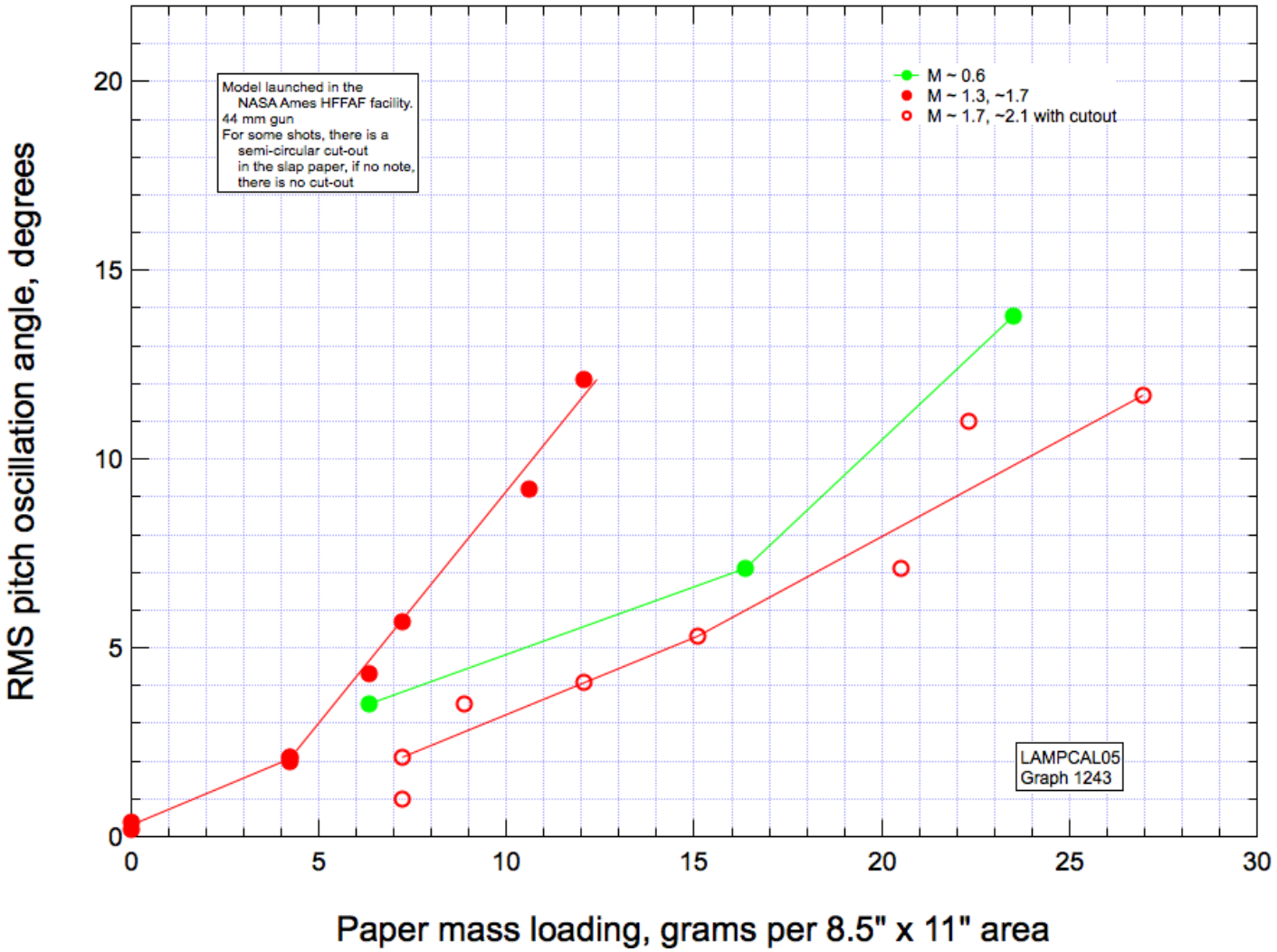

Fig. 44. RMS pitch oscillation amplitudes versus slap paper mass loading for a model launched in the NASA Ames HFFAF facility.